Integrated Optoelectronic Devices and System Limitations for WDM Passive Optical Networks

by

Sareh Taebi Harandi

A thesis
presented to the University of Waterloo
in fulfillment of the
thesis requirement for the degree of
Doctor of Philosophy
in
Electrical and Computer Engineering

Waterloo, Ontario, Canada, 2012

I hereby declare that I am the sole author of this thesis. This is a true copy of the thesis, including any required final revisions, as accepted by my examiners.

I understand that my thesis may be made electronically available to the public.

Abstract

This thesis puts focus on the technological challenges for Wavelength Division Multiplexed Passive Optical Network (WDM-PON) implementation, and presents novel semiconductor optical devices for deployment at the optical network unit (ONU). The first-ever reported L-band Reflective semiconductor optical amplifier (RSOA) is presented based on InP-base material. A theoretical model is developed to estimate the optical gain and the saturation power of this device compared to a conventional SOA. Experiments on this device design show long-range telecom wavelength operation, with polarization-independent gain of greater than 20 dB, and low saturation output power of 0 dBm suitable for PON applications.

Next, the effect of the amplified spontaneous emission noise of RSOA devices on WDM-PON system is investigated. It is shown through theoretical modeling and simulations that the RSOA noise combined with receiver noise statistics increase probability of error, and induce considerable power penalties to the WDM-PON system. By improving the coupling efficiencies, and by distributing more current flow to the input of these devices, steps can be taken to improve device noise characteristics.

Further, in spectrally-spliced WDM-PONs deploying RSOAs, the effect of AWG filter shape on system performance is investigated. Simulation modeling and experiments show that deployment of Flat-band AWGs is critical for reducing the probability of error caused by AWG spectral shape filtering. Flat-band athermal AWGs in comparison to Gaussin-shape counterparts satisfy the maximum acceptable error probability requirements, and reduce the power penalty associated with filtering effect. In addition, detuning between two AWG center wavelengths impose further power penalties to the WDM-PON system.

In the last section of this thesis, motivated by RSOA device system limitations, a novel injection-locked Fabry-Perot (IL-FP) device is presented which consists of a gain section monolithically integrated with a phase section. The gain section provides locking of one FP mode to a seed source wavelength, while the phase modulator allows for adjusting the wavelength of the internal modes by tuning bias current to maintain mode-locking. This device counters any mode drifts caused by temperature variations, and allows for cooler-less operation over a wide range of currents.

The devices and the performance metrics subsequently allow for a hybrid integration platform on a silicon substrate and integrate many functionalities like reflective modulator with thin film dielectric filter and receiver on a single chip for deployment at the user-end of future-proof low cost WDM-PONs.

Acknowledgements

Words cannot describe my heartfelt gratitude to my wonderful family, for their unconditional love and support. My father, Dr. Amir Taebi Harandi, is a source of inspiration to me. His guidance is the bright light to my path in life, and his passion for family, life and nature bring about the best in me. It was him who taught me to dream far, work hard for my dreams, and to always have faith. My mother, Farzaneh Shafiei, is a dedicated teacher of love, nurture and care, whose zest for life and never-ending sacrifices made my life a heaven. I lovingly thank them both for everything they have done for my success and happiness. Thanks to my beloved grandmother, Maman Beti, as her prayers are always with me. Thanks to my two younger brothers, Saleh and Mahdi, for their ever-present support, joy and amusement.

Last but not least, I express my profound thanks to my best friend, my husband, Mehrdad Nojoumian for his love, support and encouragement throughout graduate school years. We shared this incredible journey together, from grad-lounge lunch hours to burning night lamps before deadlines, and his keen determination always motivated me. There were many rewarding moments and some tough patches, and he made sure to stand by me, always.

... To Mehrdad
For always being there

Table of Contents

List of Tables

List of Figures

xiii

xiv

xv

List of Abbreviations

ASE	Amplified Spontaneous Emission
AR	Anti-Reflective
HR	Highly-Reflective
AWG	Array Waveguide Grating
BER	Bit Error Rate
BLS	Broad-band Light Source
CAPEX	Cost Capital Expenditures
CO	Central Office
CW	Continuous Wave
DBR	Distributed Bragg gratings
DFB	Distributed Feedback Laser
DSL	Digital Subscriber Line
EAM	Electro-Absorptive modulator
EDFA	Erbium-Doped Fiber Amplifier
EIN	Excess Intensity Noise
FP-LD	Fabry-Perot Laser Diode
FSR	Free Spectral Range
FTTB	Fiber-to-the-Building
FTTC	Fiber-to-the-Curb
FTTH	Fiber-to-the-Home
FWHM	Full-Width Half-Maximum
HFC	Hybrid Fiber Coax
HH	Heavy Hole
ITU	International Telecommunication Union
LD	Laser Diode
LH	Light Hole
MAN	Metro Area Network

NF	Noise Figure
NRZ	Non Return to Zero
ONU	Optical Network Unit
OLT	Optical Line Terminal
OSA	Optical Spectrum Analyzer
PDFA	praseodymium-Doped Fiber Amplifier
PDG	Polarization Dependent Gain
PIC	Photonic Integrated Circuit
PON	Passive Optical Network
PRBS	Pseudo-Random Bit Sequence
P2MP	Point to Multipoint
P2P	Point to Point
QW	Quantum Well
RIN	Relative Intensity Noise
RN	Remote Node
RSOA	Reflective Semiconductor Optical Amplifier
SCH	Seperate Confinement Heterostructure
SLED	Super Luminescent Light Emitting Diode
SMSR	Side-Mode Suppression Ratio
SNR	Signal to Noise Ratio
TDM	Time Division Multiplexing
TO	Transistor Outlook
TE	Transverse Electric
TEC	Thermo-Electric Cooler
TM	Transverse Magnetic
VOA	Variable Optical Attenuator
VCSEL	Vertical Cavity Surface-Emitting Laser
WDM	Wavelength Division Multiplexing
WiMAX	Worldwide Interoperability for Microwave Access

Chapter 1

Introduction

The ever increasing demand for larger bandwidth that supports Triple-play services (TPS), i.e. telephone, voice, and video, as well as the doubling rate of Internet users every 4 months, has caused an extensive evolution in communication network topologies over the past decade. As such, many new technologies have been deployed and standardized, with transmission media ranging from air, coaxial cables and classical twisted pair to optical fibers. Today, telecommunication network can be divided into four major sections:

- **Backbone network**: Consisting of switches and routers for few terabytes (TB) data transmission across continents and countries reaching several thousand kilometers.

- **Metro area network (MAN)**: Transfers traffic within cities to the destination access nodes. Usually based on a ring structure to interconnect nodes with up to a 200 km span. Transmission data rates can reach up to 40 Gbps per channel.

- **Access networks**: An interface between the backbone/MAN and the user premises. Today's access networks usually provide up to 50 Mbps for up to 60 km distance.

- **User premises**: Residential or business, which lie closest to the actual costumers.

Optical fiber has been deployed in long-haul communication networks for a long time because it possesses low loss (less than 0.2 dB/km of loss in the telecom range 1530-1610 nm). The Internet backbone and the MAN have been operating based on optical fiber technology for over 30 years, with optical-electrical (OE) conversion at the exit points. This allows the network to scale up the bandwidth easily using optical advancements

such as Wavelength Division Multiplexing (WDM). With increasing popularity of coherent detection being implemented with polarization diversity at the receiver, the polarization dimension can be used for advanced modulation formats [6]. This leads to optical communication links with coherent receivers at bit rates up to 100 Gbit/s [7], and aggregate transmission rates in the order of 102 Tb/s over transmission distances of greater than 200 km [8].

As for the access network known as the *last (first) mile*, the dominant network infrastructure is still based on copper-cable technologies. There is virtually 100% copper-access coverage in large areas, with examples of Asymmetric Digital Subscriber Line (ADSL), Very-high-bit-rate digital subscriber line (VDSL), and Hybrid fiber Coax (HFC). The performance metrics of these technologies are shown in Table 1.1. Copper-based technologies are close to their bandwidth limit, and provide only few Mb/s per user over a short distance. These technologies generate a bottleneck at the gateway of the backbone to the access networks, shown schematically in Figure 1.1. The access network should ultimately be supported with optical fiber. Although this requires extra expense of fiber installations, it will remove the present bottleneck.
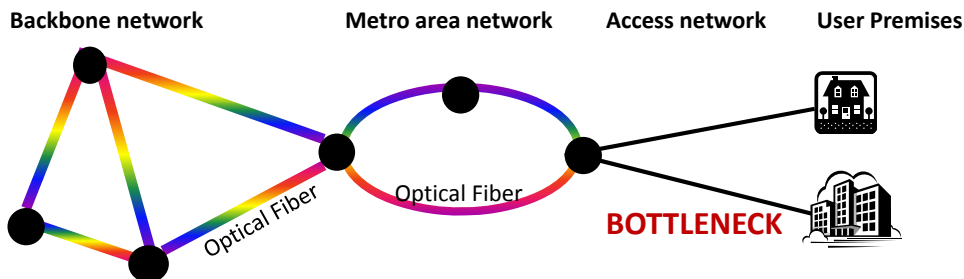
Figure 1.1: Bottleneck of present copper-based access networks

Fiber installations are happening at an exponential growth rate around the world with real data showing the trend in Figure 1.2. According to the FTTH council annual ranking for 2012 [9], which tracks global deployment of fiber access, 30 countries in the world have at least 1 % of their households connected through FTTH. This translates to over 8 million homes with fiber connections for early 2012. For North America, United States is building the infrastructure with 8 % of the households connected to FTTH. Canada has around 170,000 fiber-connected households, about 1.24 % of the total number of households in the country. Most of the fiber deployment in Canada is in the far east or the west of the country.
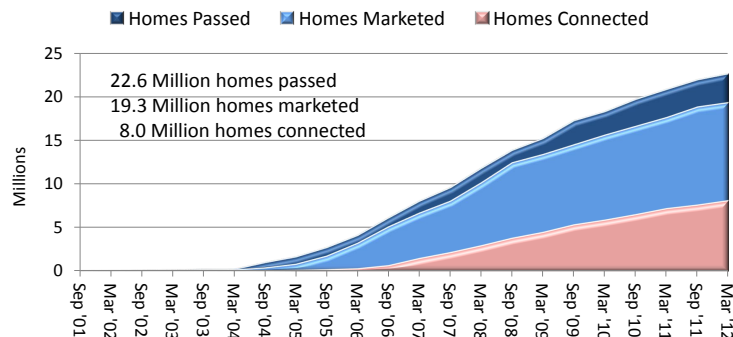
Figure 1.2: North american FTTH growth rate. (Source: FTTH Council)

Typically, fiber-deployed access networks utilize fiber in a more cost-effective point-to-multipoint (P2MP) scheme, where optical fiber is shared from a central office up to a remote node, from which a single fiber is assigned to the user-end. Depending on the user fiber termination point there are various classifications for the P2MP fiber access network, 1) Fiber-to-the-curb (FTTC), where the fiber drops at a cabinet several hundred meters away from the customer 2) Fiber-to-the-Building (FTTB), where the fiber drops at the basement, and 3) Fiber-to-the-Home (FTTH), where fiber is pulled to the customer home. The first two schemes require copper wire solutions to relay the data to the customer's home after the fiber drop. Alternatively, the first/last mile optical fiber access solutions (i.e., FTTX) can be combined with wireless technologies to connect multiple scattered WiFi/WiMAX base stations. WiFi-wireless local area network (802.11) and WiMAX-Worldwide Interoperability for Microwave Access (802.16) are the IEEE standards for wireless and broadband access networks. This integrated broadband network can take advantage of the bandwidth benefit of fiber communications, and the mobile inexpensive features of wireless communications for connection to sparsely populated areas [10].

The network topology of interest for most FTTX deployment is the *passive optical network* (PON). Next sections will provide a detailed overview of the PON technologies and the optical components required for their deployment.

1.1 Passive Optical Networks

Passive optical networks are P2MP networks, providing fiber connectivity to the user-end, and were originally proposed in 1988 [11]. The key feature of a PON is the presence of only passive components in the field, i.e. elements that operate without any electrical power.

As such, there are no amplifier or repeater elements in the field, and no need for electrical supplies. As such, PON architectures offer great advantages like low cost, high reliability and easy maintenance for network operators.
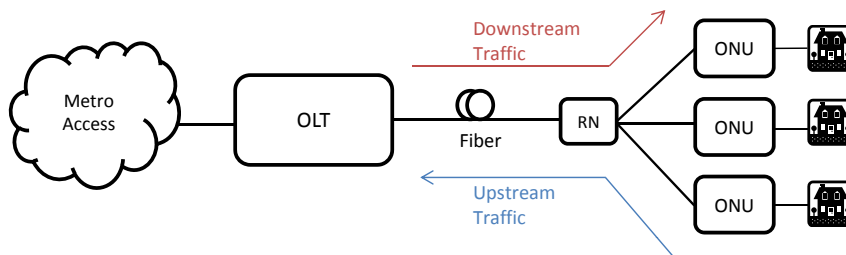
Figure 1.3: PON definition OLT: Optical Line Terminal ONU: Optical Network Unit RN: Remote Node

The PON topology and terminology is shown in Figure 1.3. Fiber connectivity is established from the optical line terminal (OLT) at central office (CO) to the optical network units (ONU) at customer premises. The passive elements are placed at the remote node (RN), which sits close to ONU. The data traveling from user-end towards OLT is known as *upstream traffic*, and the data traveling to the user-end nodes is known as *downstream traffic*. The bandwidth of the shared fiber must be allocated to each user based on de-multiplexing techniques by either time sharing using **time division multiplexing (TDM)** or **wavelength division multiplexing (WDM)**.

1.1.1   TDMA-PON

In a TDM-PON, a passive optical splitter is deployed at the RN as a cost-effective and simple device for splitting the incoming optical power into equal output power. The downstream traffic from OLT is distributed to ONUs through the passive splitter by broadcasting. The broadcast data is encrypted properly, so each ONU can only access its own data. The upstream traffic from all ONUs to OLT is multiplexed in the time-domain. This is shown in Figure 1.4 where the bandwidth of a single wavelength is time-shared between different users using various protocols. To separate the upstream and downstream traffic, a wavelength duplexing scheme is used. As an example, for downstream data, 1490 nm wavelength region is used while for upstream data 1310 nm region is deployed. The user-end at the ONU can compose of a single home, a building with many users or it can alternatively be a wireless access point.

4
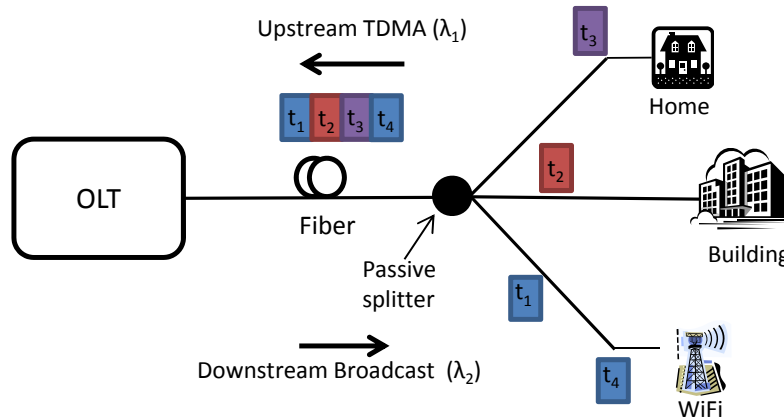
Figure 1.4: TDMA-PON bandwidth allocation using single wavelength for upstream data

Based on the time-multiplexing protocol, TDM-PONs are labeled and deployed appropriately. Broadband PON (BPON) uses the ATM protocol [12]. Ethernet PON (EPON) deploys the Ethernet protocol [13]. Gigabit PONs (GPON) carry ATM as well as Ethernet traffic [14]. GPON nicely combines the quality-of-service advantages of ATM with the efficiency of Ethernet. A more recent standard for data links covering shared data rates of up to 10 Gb/s has been standardized and named 10-G PON [15]. Depending on each protocol, aggregate data rates can range from 1-10 Gb/s, shared between 32-128 user nodes, and covering ranges up to 30 km. Table 1.1 compares these technologies based on bitrate, distance covered and number of power splitting nodes. TDM-PONs have some drawbacks which hinder their future-proof application. These shortcomings can be outlined as follows:

- Security issues due to broadcasting nature of downstream traffic.
- Bandwidth sharing of upstream traffic which diminishes the maximum bandwidth offered by a single wavelength.
- Short coverage reach due to the power split losses associated with the optical splitter.
- Complicated bandwidth allocation protocols.
- Requirement for ranging protocols and timely synchronization between nodes.

1.1.2 WDM-PON

Wavelength division multiplexing is the ultimate solution for fast, efficient and secure bandwidth allocation in passive optical networks, and the subject of research proposals for

Technology	Standard	Downstream Rate	Upstream Rate	Reach	Nodes
ADSL	ITU G.992	24 Mb/s	3 Mb/s	1 km	n/a
VDSL	ITU G.993	100 Mb/s	100 Mb/s	300 m	n/a
HFC	IEEE 802.14	40-100 Mb/s	10 Mb/s	3.6 km	n/a
WiFi	IEEE 802.11	<600 Mb/s	<600 Mb/s	<250 m	n/a
WiMax	IEEE 802.16	<750 Mb/s	<750 Mb/s	<50 km	n/a
BPON	ITU G.983	622 Mb/s	155 Mb/s	20 km	32
EPON	IEEE 802.3ah	1.25 Gb/s	1.25 Gb/s	20 km	64
GPON	ITU G.984	2.5 Gb/s	1.25 Gb/s	20 km	64
10G-PON	ITU G.987	10 Gb/s	2.5 Gb/s	25 km	128

Table 1.1: Summary of Broadband Access Technologies, the bitrates are based on latest technology developments

next generation broadband access. WDM-PONs were first proposed in [16], where every user is assigned a dedicated wavelength, with the flexibility of wavelength add or drops over a single shared fiber. In essence, a virtual point-to-point link is made between the OLT and each ONU in a P2MP PON architecture. Each ONU can operate at the maximum bit rate of a wavelength channel, and support multiple services from wireless to coaxial. The WDM-PON example is shown in Figure 1.5, where a separate wavelength channel is used from the OLT to each ONU.

In the downstream direction of a WDM-PON, the wavelength channels are transmitted from the OLT to the ONUs on a single fiber using an array of tunable lasers located at the OLT. The wavelength channels are then demultiplexed by an arrayed waveguide grating (AWG) router located at the passive RN, and a unique wavelength is assigned to each ONU port. The AWG ports are periodic in nature, where multiple spectral orders of input wavelength channels are routed to the same output port. This cyclic feature of the AWG allows for downstream and upstream transmission to occur in different wavelength windows. Within each wavelength window, the wavelengths are separated with wavelength spacings determined by AWG ports. The Wavelength spacings and wavelength bands are further discussed in the next section.

Every ONU is equipped with a transmitter laser source for transmitting upstream traffic to the OLT, and receiving downstream traffic from it. At the OLT, the upstream signals are received through a demultiplexer device and a receiver array. The demultiplexer device can be another AWG similar to the one deployed at the RN.

As a future-proof solution, the WDM-PON should be scalable in terms of number of user-nodes and bandwidth. The present research on WDM-PON aims to achieve simple, cost-efficient and easy to operate solutions based on single type of optical components.
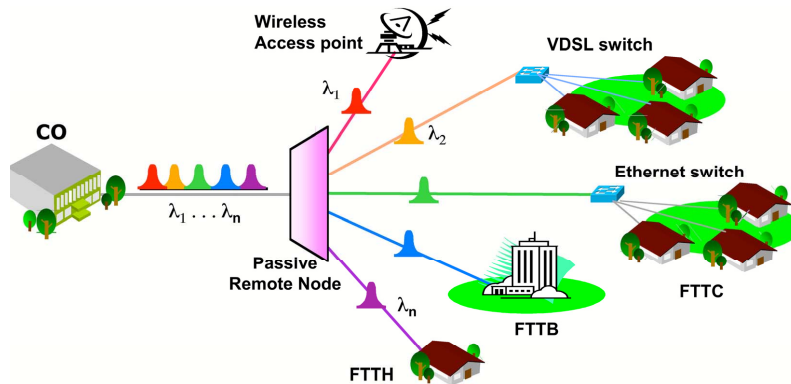
Figure 1.5: Schematic of a WDM-PON system supporting multiple services [1]

Wavelength Division Multiplexing

Wavelength-division multiplexing (WDM) is a method of combining multiple laser wavelengths for transmission along optical fiber media. This method increases signal capacity in addition to allowing for bidirectional communication links over a single fiber. WDM allocates operational wavelengths to users in a systematic manner. The wavelength spacing for WDM networks can be categorized as either Coarse WDM (CWDM) with around 20 nm spacing, or dense WDM (DWDM) with less than 1 nm spacing. The spectral grid for CWDM is defined in ITU G.694.2, with a wavelength spacing of 20 nm [17]. If the full wavelength band from 1270-1610 nm is used, it can house 18 individual wavelength channels seen in Figure 1.6. CWDM networks have less stringent operational requirements for temperature-controlled environments due to larger spectral range. However, using a conventional single-mode optical fiber for these systems limits the number of available channels due to the presence of water peak attenuation in the 1370-1410 nm range. The wavelength spacing in a CWDM for all wavelength bands is shown in Figure 1.6.

In DWDM, on the other hand, the wavelength spacing can be as narrow as 0.2 nm (25 GHz) [18]. Because DWDM can allocate many wavelength channels within a narrow range, it is considered the ultimate solution for WDM-PON. The devices used for DWDM applications need to be controlled for cross talk between adjacent channels and also temperature controlled. Therefore, the DWDM scheme introduces more cost than CWDM. The multiplexing devices must also support the requirements for dense channel spacing with low channel cross-talk. The standardized wavelength spacing for 0.8 nm (100 GHz) channel spacing is shown in Figure 1.6.

In Figure 1.6, the conventional telecom wavelength bands are depicted. The operational
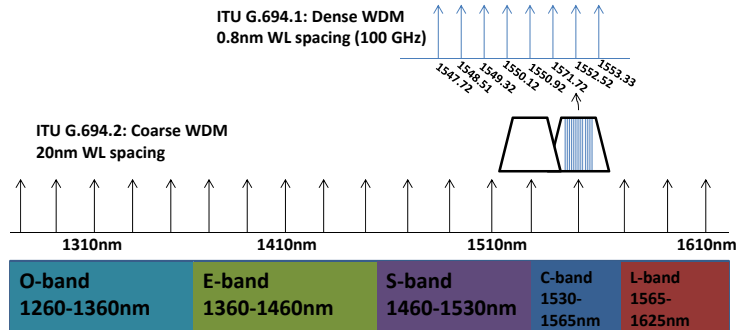
Figure 1.6: CWDM and DWDM wavelength grids based on ITU standards

optical wavelength will affect losses in the WDM-PON system as well as impose some dispersion effects. Some wavelength bands exist where these effects are weakest, and have been standardized for optical communication. The most favorable windows of operation are the S (short), C (common) and L (long) bands, because the optical fiber losses are minimal in these bands. The C-band and L-band have the lowest fiber attenuations, and facilitate optical amplifications.

Earlier, the E (extended) band was avoided due to the water peak region, and the presence of high-attenuations. Today, however, optical fiber manufacturers have dramatically reduced losses in this region, and look at this region for future extensions to the O (original) band [19]. The operable E-band bridges the gap between other wavelengths bands. As an example, a field trial for WDM-PON was performed in Korea, where the Common-band (1534-1559 nm) was used for the downstream data, since the loss of the fiber is minimal at this band, and for upstream data, E-band (1426-1449 nm) was chosen to have a sufficient guard band for future extensions [5].

Multiplexing Devices

The RN in a WDM-PON is placed close to the user-end and performs multiplexing/demultiplexing of individual wavelengths on a fiber for distribution to various nodes. Unlike TDM-PONs, optical splitters cannot be deployed in WDM-PON remote nodes. If an optical splitter is used at the RN for WDM-PON applications, wavelength specified filters must also be placed after the optical splitter.

Thin-film filters or multilayer interference filters are an alternative solution as wavelength multiplexers. By positioning cascaded filters in the optical path, wavelengths can

be de-multiplexed, and vice versa. Each filter is designed to transmit a unique wavelength while reflecting others. This type of filter is better for CWDM applications [20].

An Arrayed waveguide grating (AWG) manufactured by silica-based technology is a widely used industry de-multiplexer for large number of wavelengths (>16), which is considered for WDM-PON applications. Parameters of importance in an AWG are 1) insertion loss, 2) polarization dependence, 3) free spectral range (FSR), and 4) cross-talk. A desirable AWG should possess low insertion loss and polarization dependence with any achievable FSR. For a channel spacing of 100 GHz, the insertion loss is at maximum 5.5 dB for Flat-band AWG and 3.5 dB for Gaussian AWG. The polarization dependent loss is reported to be less than 0.5 dB, with less than -20 dB cross-talk [3].

The AWG structure is presented in Figure 1.7(a). It consists of two slab regions, surrounding a grating section. The grating section consists of several waveguides with a constant length increment between adjacent waveguides. This causes a phase difference in the light traveling through them. The incoming light to the first free-propagation region is distributed among the grating waveguides. The output of each grating waveguide enters the second slab where it interfere with other beams to create different wavelengths at each output port [21]. An important property of the AWG is that there is a period where the output wavelength repeats itself, known as the Free Spectral Range (FSR) of the AWG. A wavelength can only occur at an integer space of the FSR, leading to a *cyclic property* of the AWG.

AWGs can be used both as multiplexer and de-multiplexer at the same time. It is common to use different wavelength bands for upstream and downstream data transfer, and use the cyclic property to assign a single AWG port to each ONU. This is shown in Figure 1.7(b), where sample $\lambda_1 - \lambda_4$ are assigned to downstream traffic, and consequently $\lambda_5 - \lambda_8$ are allocated for upstream traffic. If the same wavelength band is used for upstream/downstream signal transmission, a wavelength re-use scheme along with 2 fibers is deployed, and the AWG must have twice number of ports [22]. This is shown in Figure 1.7(c), where two separate ports are assigned to each ONU, and a wavelength reuse of the upstream transmission along with two sets of fibers is deployed [23].

AWGs have one drawback, and that is the wavelength shifts about 0.01 nm/°C with variations in temperature. This is due to the refractive index change of silica waveguides. The AWG at the passive remote node is located at outdoor plants with variant temperatures, with no electrical coolers. Therefore, it is essential to deploy temperature insensitive AWGs. Developmental efforts have been made to reduce the temperature dependence of AWG channel wavelength. Recently, athermal AWGs have been realized which are very reliable, and provide exact wavelength matching with the optical source despite variations
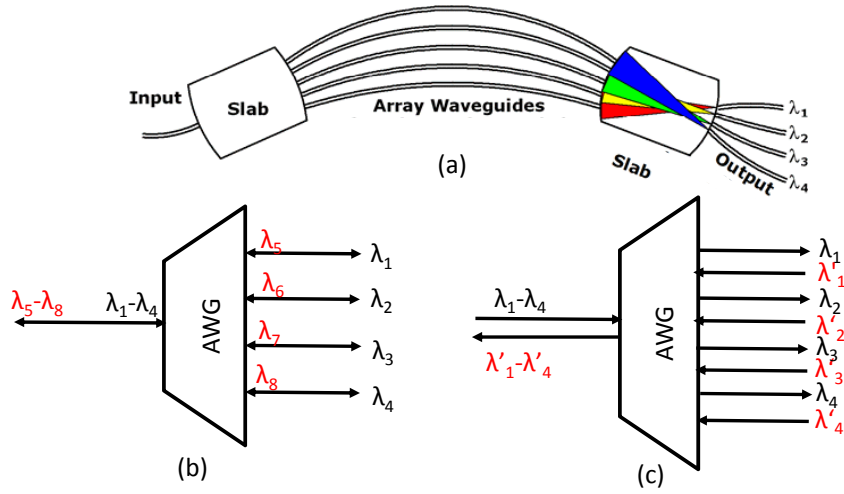
Figure 1.7: AWG operation for (a) AWG structure (b) bi-directional link (c) uni-directional link

in environmental conditions [24, 25, 26]. The athermal solution is achieved by inserting a compensating material with a different temperature coefficient than silicon to adjust the optical path length.

1.2   Devices for WDM-PON

The ONU has a direct impact on the cost capital expenditures (CAPEX) per customer, which is the money spent to acquire or improve long term assets. In terms of economics, the requirement for a low cost and low maintenance laser source is essential. Therefore a single type of device is desired at all ONU terminals, which is operable over a wide wavelength range with a centralized upstream wavelength assignment. These transmitter sources should operate independent of wavelength (*colorless*), and should be temperature invariant (*cooler-less*). This would enable lower operation and maintenance costs, and eliminate the need for sophisticated thermoelectric (TE) packaging. In what follows, several attractive proposals for ONU sources are discussed, and are classified as tunable lasers, broadband light sources, and reflective devices.

1.2.1 Tunable Lasers

Fast tunable lasers are widely deployed in long-haul WDM transmission systems. The existence of these lasers with switching times in the range of nanosecond makes these devices attractive for a WDM-PON network. Such lasers can be employed for both downstream data transmission, and for the generation of CW seeds to be used in the ONUs for upstream data modulation. Tunable lasers can be designed using a gain medium, and reflective mirrors. Some designs are based on the distributed feedback (DFB) laser. Examples include the temperature tuned array of DFB lasers [27]. Other designs of such lasers include the external cavity tunable laser [28, 29], and use of the distributed Bragg-reflector (DBR) grating as the mirrors [30], along with electro-absorption modulator.

One obvious application of tunable lasers in a WDM-PON is at the OLT for downstream traffic generation. With fast tunable lasers optical modulation can be performed at greater bit rates. An OLT in a WDM-PON is made of the OLT transceiver arrays, with low-cost tunable lasers monolithically integrated on a single chip [31]. The integration circuit is considered necessary in order to reduce both power consumption and form factor in the OLT .

Tunable lasers can also be considered for generating an upstream signal at the ONU. The concept is shown if Figure 1.8. A dedicated tunable laser along with an external modulator is deployed at every ONU node. The laser spectral width is narrower than AWG spacing. Such deployment offers great optical performance and flexibility in terms of wavelength. The number of ONUs supported will be determined by the channel spacing of the AWGs, and the tuning range of the laser. The problem with this scheme is the high cost of a much more sophisticated laser at the source, need for maintenance, and an internal wavelength locker to ensure the laser operates at the correct wavelength channel. Furthermore, to maintain a stable laser operating regime, external modulation rather than simple direct laser modulation is preferred. Cost reduction is also limited due to the low production yield of the device. As such, despite excellent performance, the tunable-laser scheme is cost prohibitive [32].

1.2.2 Spectrally-Sliced Sources

Spectrum slicing using a broad-band incoherent light source (BLS) has been proposed as an efficient technique that requires only single type of device at all nodes [33, 34]. Generally, a BLS can consist of a super luminescent light emitting diode (SLED), an erbium-doped fiber amplifier (EDFA), or FP laser diode (FP-LD). These devices provide amplified spontaneous

11
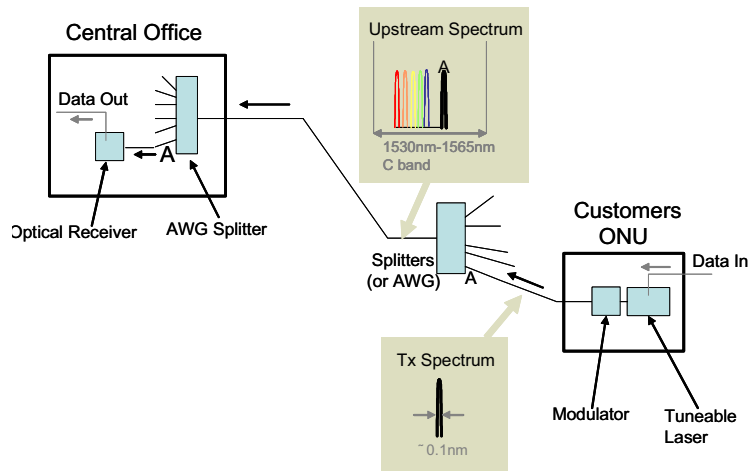
Figure 1.8: Tunable laser at an ONU in a WDM-PON [2]

emission (ASE) spectrum, and can be deployed at the ONU as well as OLT. If the BLS is placed at the OLT, local modulation of the downlink data can be achieved, or it can act as a source for generating seed light for upstream data signals. At the ONU, it can be used as a light source for generating upstream traffic. All techniques are convenient in the sense that a single type of device could be deployed at all ONUs. In addition, these devices are inexpensive for mass production, and would not require wavelength management at the user end.
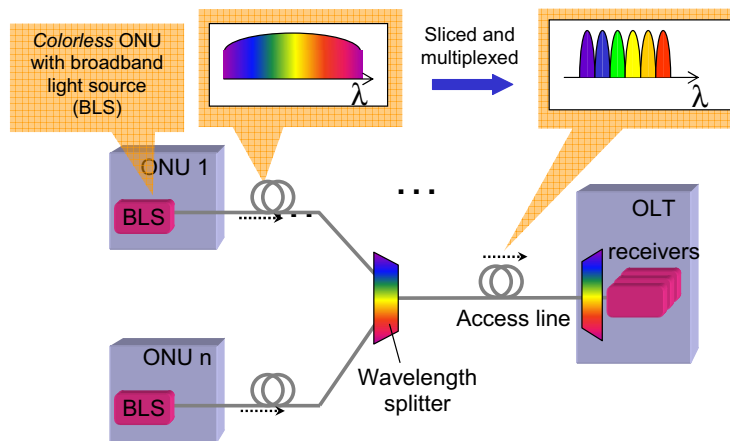
Figure 1.9: WDM-PON with spectral slicing [3]

12

The concept of spectrum slicing in a WDM-PON in the downstream direction is shown in Figure 1.9. The spectrum, with at least full width half maximum (FWHM) equal to the wavelength band of the WDM system, is band-pass filtered by an AWG. By this means, only a narrow spectrum part of the spectrum is used per ONU, allocating dedicated bandwidth is to every ONU. As a result of spectral slicing, the source usually lacks power, requiring an optical amplifier.

Specifically, the SLED can be fabricated at a low cost and modulated directly, however there is a limit on the number of ONU node splits, due to output power limitations. The ASE from an EDFA has much higher output power, however its deployment requires an external modulator which adds to cost.

The biggest disadvantage of the spectral slicing scheme is the presence of noise sources in the broadband sources. This imposes a limitation on the most achievable modulation speed. The noise consists of mode-partition noise, intensity noise, and optical beat noise. As a result, higher data rates would not be achievable for this scheme, and a few upstream data channels of 155 Mb/s are realizable.

1.2.3 Reflective Devices

In this scheme, a separate seed wavelength located at the OLT is used to allocated upstream data traffic. A reflective device at the ONU modulates the seed light, and reflects it back as upstream traffic. The seed wavelength could be from a coherent laser source, such as a DFB laser [35], or from an incoherent laser source such as a BLS [36]. The advantage of this scheme is that optical power produced by the ONU transmitter is now all within the required spectral channel.

However, low cost transmitter sources at the ONU are still an issue. Two solutions have been proposed for the purpose of cost-effective reflective architecture, and are classified as the injection-locked Fabry-Perot laser source, or the single polarization/polarization independent reflective semiconductor optical amplifier (RSOA). Both devices modulate, amplify and reflect the upstream data signals to the central office.

Figure 1.10 represents the proposed WDM PON architecture based on reflective devices. The downstream signals are generated using one DFB laser per ONU, and operate in the C-band wavelength region. They are multiplexed onto the shared fiber using an AWG at the OLT and demultiplexed later at the RN by another AWG for distribution to the corresponding ONU. A C/L band WDM filter separates up and downstream wavelengths at the ONU. Downstream signals can easily achieve bit rates of 1.25 Gb/s and higher.

13

The upstream signals are seeded by a BLS source like a SLED emitting incoherent light at the OLT over the L-band. The seed light is sent over the optical fiber using a 3-dB coupler and is then spectrum sliced through the AWG. The optical fiber can reach to over 20 km in distance. The ONUs each receive an incoherent spectrum slice of 0.2, 0.4 or 0.8 nm bandwidth depending on the AWG bandwidth. The sliced spectrum is then modulated with upstream data in L-band, amplified and reflected back through the shared fiber and the AWG. The upstream data is then demultiplexed by OLT AWGs and detected by the corresponding receivers.

The reflective scheme for WDM-PON has attracted quite a lot of attention, due to elimination of wavelength management at the user end, potential low cost of such components, and ability to achieve higher bit rates. Much experimental research has been done to implement reflective architectures, which are reviewed in the next section.
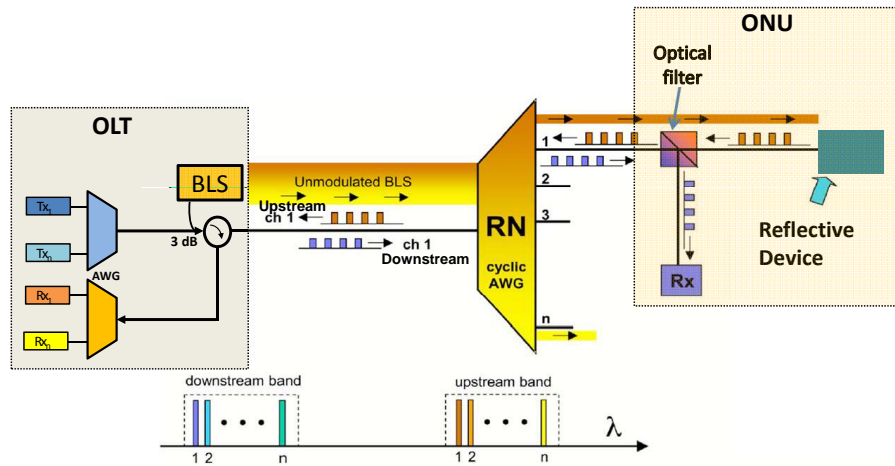
Figure 1.10: Reflective architecture for a WDM-PON

1.3 Reflective Transmitters at ONU

Reflective devices at the ONU provide the functionalities of amplification, reflection, and modulation of upstream traffic. In addition, a single type of device can be deployed at all nodes. This section reviews the prior research and techniques related to deployment of reflective SOAs and Fabry-Perot lasers as two main candidates for this purpose.

1.3.1 Reflective SOAs

Dual port semiconductor optical amplifiers (SOA) have been around for many years, for various applications. Figure 1.11(a) depicts the experimental setup requirement to deploy SOA devices at the ONU. The SOA device would require a 3-dB coupler to split the upstream/downstream signal on the shared fiber. The input and output ports of the SOA are connected to the two ports of the 3-dB splitter with an isolator in one arm. The input signal is split into two ports with a 3-dB splitter and one signal is send through the SOA while other is isolated with an isolator. The signal after amplification through the SOA is coupled back to the input fiber with the 3-dB coupler. However, this architecture has some serious issues especially with the inherent 3-dB loss per pass in the coupler resulting in increased noise figure. By applying a reflective coating on one facet of the SOA device, a single port device is originated as shown in Figure 1.11(b). The single-port reflective SOA device eliminates dual fiber couplings, and use fewer optical components. In addition, the RSOA device has simple and cost-efficient packaging using conventional transistor outlook (TO)-cans [37].
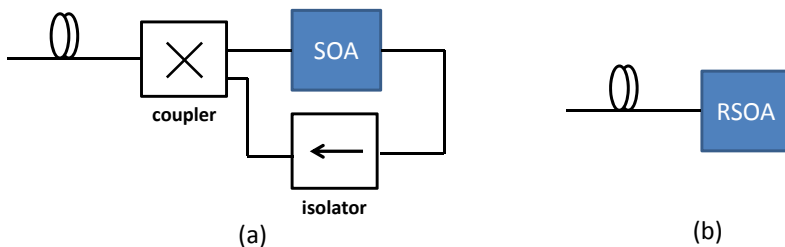
Figure 1.11: RSOA at the ONU vs. SOA with more sophisticated packaging

RSOAs were originally proposed as single port devices in mid '90s [38]. They were used as WDM modulators in local access networks and experiments demonstrated modulation rates of 100 Mb/s. These devices provide high output power and low noise performance due to amplitude squeezing when operated near saturation regime.

The use of a spectrally-sliced WDM with RSOAs was first demonstrated in [39]. Seeded traveling-wave reflective SOA modulators were used. A dense WDM comprising of eight l nm slices, modulated at a data rate of 1.25 Gbps are shown to operate over 25 km of standard fiber. The RSOA used is single-polarization, and therefore polarization controllers are required.

The duplex WDM-PON using remodulation of the downstream traffic by an RSOA was proposed in [40]. A downlink signal, modulated at 2.5 Gb/s, was remodulated at

900 Mb/s in the upstream direction. The downstream signal achieved good performance, but the upstream signal induced huge power penalties compared to back-to-back in the order of 10 dB. As such, a bidirectional WDM-PON was demonstrated which deploys gain-saturated reflective SOAs [41]. The RSOA had input saturation power of -13 dBm and gain of 13 dB within the C-band for arbitrary polarization states. The upstream signals were generated by remodulating the downstream signals using the RSOA. Experiments over 20 km transmission showed bidirectional transmission with 1.25 Gbps for upstream and 2.5 Gbps for downstream data rates. Similar work has also been done in [42].

In [35], a WDM-PON system is proposed which uses the laser light injected RSOA as the optical transmitter. The optical carrier of laser light consists of a pair of the perpendicularly polarized laser lights to avoid the polarization dependence of the RSOA. This scheme introduces more cost, so the authors mention sharing of the optical carrier by several WDM-PON systems to save the cost. The transmission performance of the RSOA was measured by modulating the polarization mixed injection laser at 1.25 Gbps. In this scheme, the combined effect of Rayleigh backscattering [43] and the noise induced by the feedback of optical signals into the RSOA increases the required level of optical injection power into the RSOA.

[44] and [45] present a different solution where self-seeding of an RSOA is used to directly modulate it, therefore the presence of a laser source at the central office is eliminated, and a passive reflective path is placed at the remote node to reflect a spectral slice of the broadband ASE light emitted from each RSOA. The reflected spectral slice, termed as a seeding light, establishes a self-seeding of the RSOA, and the transfer rate is 622 Mbps, therefore there is no clear advantage to such scheme.

In [46], the feasibility of implementing a 10 Gbps WDM-PON by using directly modulated RSOAs together with electronic equalizers is investigated. The modulation bandwidth of the RSOA, limited by carrier lifetime, is about 2 GHz, and can be increased by electronic equalization techniques.

In [47], a Fabry-Perot etalon is proposed for use at each ONU before the receiver, which can extend the transmission distance by reducing the transient chirp. This way low ER modulation signals can be deployed for WDM-PONs with RSOAs at the user ends to reduce the intensity fluctuation of the RSOA remodulated upstream signals. The etalon performs spectral reshaping and waveform reshaping to the downstream signals. The same etalon can be used for multiple wavelength channels. Performance improvement on WDM-PONs with 10 Gbps and 1.25 Gbps data rates for the downstream and upstream transmission has been reported over a 25 km fiber span.

[48] reports on the operable ranges of temperature and wavelength for a 1.25 Gbps

WDM PON implemented by using uncooled RSOAs, since both the gain and modulation bandwidth of the RSOA are substantially reduced at high temperatures. As a result, it is difficult to achieve the error-free operation at temperatures above 40°C. The authors have implemented a simple bias-control circuit, in which the bias current is increased with the operating temperature of the RSOA. Therefore, the operable wavelength range of the WDM-PON system is around 55 nm in the temperature range of -20°C to 60°C.

In all above schemes, a few issues remain to be tackled. Mainly, the RSOA device itself needs to possess low noise characteristics, and polarization independence for practical applications. Also, the direct modulation imposes a bit rate limitation of 1.25 Gbps for the device because of the carrier lifetime limit on the RSOA.

1.3.2   Injection-Locked Fabry-Perot Lasers

In [34], FabryPerot lasers for use as upstream transmitters in a WDM-PON were first proposed, and transmission of a 10 Mb/s signal through each port of a wavelength-grating router followed by 18 km of fiber was demonstrated. The authors promote the use of FabryPerot lasers due to providing more output power than low-cost light-emitting diodes. However, the bit-rate of such system is limited, due to multi-mode nature of FP laser diodes. Mode-fluctuations due to heating of laser and random spontaneous emission coupling produce noise when transmitted through the system. As such, these devices need to be injection-locked for higher operational bit-rate. In the following, various seed light sources for injection-locking are described.

Incoherent Injection

Injection-locking can be performed by using a BLS as the seed source for an ONU Fabry-Perot laser diode. In [49], the first demonstration of a WDM source employing an uncooled FabryPerot laser diode using injection-locking was presented. The output wavelength of FP SLD was locked to the externally injected narrow-band ASE source, resulting in single mode operation with a measured side-mode suppression ratio of the wavelength-locked FP mode of around 29 dB. The transmission rate was reported to be 155 Mb/s over 120 km of nondispersion-shifted fiber. Later, in [50], a bidirectional 12-channel WDM-PON with 50 GHz channel spacing based on wavelength-locked FabryPerot laser diodes was demonstrated. The proposed WDM-PON system could accommodate 80 channels with erbium-doped fiber amplifier-based broad-band light sources, and transmit downstream and upstream at rates of up to 155 Mb/s.

Using FP-LDs injection-locked by spectrum-sliced broad-band incoherent light source, the data rate is limited because of the conversion of excess intensity noise (EIN) from the seed light to the FP-LDs. Therefore, in order to further increase the data rate, the use of high-quality seed light sources with low IN is essential.

Coherent Injection

To improve the injection-locking mechanism, a WDM-PON architecture using FP-LDs that are injection-locked by continuous wave (CW) coherent seed light such as DFB laser has been presented [51]. The CW seed light sources were located at the central office, which could be shared by many WDM-PONs and hence keep the implementation cost potentially low. 16 FP-LD cavity modes were individually selected for 10 Gb/s transmission by a direct modulation scheme.

The advantage coherent injection is that it does not need an amplifier and an external modulator at each ONU. However this scheme is not cooler-less, so a change in temperature would shift the FP modes, and the seed light would lose locking.

1.4   Objective

To drive forward the deployment of WDM-PONs in next generation access networks, the focus is on transmitter sources at the ONU, which determine a majority of implementation cost. The first goal of this research is to identify transmitter source designs for ONU which satisfy the requirements for deployment of colorless and cooler-less devices, and highlight limitations and requirements of practical WDM-PON systems. The second goal is to develop design solutions for colorless transmitters using III-V material, through theoretical and simulation models as well as experimental verifications.

During a review of current research on WDM-PON components, we could not decide whether ILFP or RSOA was the better choice for application and integration at the ONU. The RSOA devices offer noise reduction of the seed signal excess intensity noise when driven in saturation [39]. However, the cost parameters of RSOAs is still a main deciding factor. ILFP lasers on the other hand, are cost effective solutions due to the low-cost fabrication. But, ILFP laser is mainly limited by its locking stability and perhaps excess intensity noise in case of incoherent injection. Therefore we decided to investigate each device in depth.

In order to develop RSOA designs, we first looked into well-known SOA devices, and their design solutions. From the established knowledge of these devices, a simple and practical design solution for RSOAs can be found. As for the SOA devices, there exist no realizable L-band operable solution for deployment, although some efforts have been made in literature with limiting performance [52]. L-band operation is important for RSOA devices in PON applications due to the dual wavelength band operation of upstream and downstream traffic, where downstream traffic is realized on C-band, and upstream traffic should be placed on L-band. These two wavelength bands inhabit the natural region for low optical losses in glass fiber. As such, we decided to look into a design solution for L-band polarization-independent RSOA device by using earlier knowledge of the SOA design.

Further, the noise of RSOA device and it's effect on overall system performance were neglected. One claim made was that the noise figure (NF) of the RSOA is the same as SOA [53]. However, all practical demonstrations of RSOAs had a poor NF, in some cases as high as 15 dB. This was attributed to losses due to poor coupling of RSOAs. To our initial understanding, we expected the NF to be degraded for RSOAs compared to SOAs. An analytical model was needed to compare the performance of both devices in terms of carrier dynamics and NF, and study RSOA NF effects on WDM-PON systems.

For spectrally-seeded RSOA-based WDM-PONs, the AWG spectral shape should have an effect on WDM-PON performance due to signal filtering. System test demonstrations in the literature replace the AWG with a wide-band filter at the receiver, and show adequate bit-error-rate (BER) performance, but this does not represent an actual WDM-PON system. Therefore the BER performance analysis of WDM-PON systems with Gaussian/Flat-band AWGs is required to determine feasibility and requirements.

As another perspective, FP laser sources have been investigated, and the issue of these devices with mode instability has been approached through increasing the device length to decrease wavelength spacing. But if the FP laser source can be modified in such a way to compensate for the mode drifts, better device gain performance, lower operating current, and more stable device can be achieved.

1.5   Thesis Contributions

The contributions of this research to the devices for WDM-PONs are summarized as follows:

1. An L-band polarization-independent RSOA is presented for the first time with gain greater than 20 dB, and polarization-independent gain of less than 1 dB with satu-

ration output power of around 0 dBm. The device covers the operational telecommunications L-band required for upstream data transmission.

2. Noise figure of an RSOA is analyzed in detail through a numerical model, and compared to the conventional SOA with the same characteristics. It is shown that the RSOA device is inherently higher in NF than the SOA. System level simulations of incoherent-injected RSOAs in a WDM-PON show that the power penalties associated with increased NF of RSOAs are in the order of at least 4 dB.

3. In incoherent-injected WDM-PONs deploying RSOAs, it is shown through simulations and experiments that Flat-band athermal AWGs have improved performance in terms of BER than their Gaussian-shape counterpart due to the effect of signal filtering, and the power penalties associated with their deployment is at least 2.5 dB.

4. An injection-locked laser is proposed which consists of a gain section monolithically integrated with a phase section to achieve mode locking stability over large temperature and current ranges. The phase section allows for adjusting the wavelength of the internal Fabry-Perot mode to match the input injected signal and counter any mode drifts. With a current of 14 mA, 100% phase shift is achieved.

1.6   Organization

In Chapter 2, an analytical model is presented to compare the performance of an SOA with an RSOA in terms of gain and saturation output power. After that, a novel polarization independent RSOA design is presented, which is operable at the L-band. At last, the device measurement results are presented. Chapter 3 investigates the value of RSOA NF through an analytical model and in comparison to the SOA. The model is later supported by experimental measurements of device NF. Later, the effect of RSOA NF on system performance is investigated through a simulation model, and associated power penalties are discussed. Chapter 4 is focused on the AWG filtering effects in spectrally-sliced WDM-PONs deploying RSOAs. The power penalties associated with Gaussian and Flat-band AWGs are investigated through system modeling and experiments. The effect of AWG center wavelength detuning on WDM-PON performance is also investigated. In Chapter 5, first the principle operation of injection-locked Fabry-Perot lasers are discussed. Next, a novel FP laser with an integrated phase modulator is proposed and demonstrated for use in WDM-PONs to counter mode drift issues. Later, measurement results of this device are presented. Finally, chapter 6 summarizes the knowledge gained throughout the research and present conclusions and recommendations for further research.

Chapter 2

Reflective Semiconductor Optical Amplifier (RSOA)

Semiconductor Optical Amplifiers have several advantages such as potential low fabrication cost, small dimensions, monolithically integrable, wide bandwidth, and fast time response. In contrast, they possess high-coupling loss, and polarization dependence. SOAs are widely and most commonly used for non-linear applications like, detection, modulation, wavelength conversion and signal regeneration. As such, they are a potential candidate as opto-electronic transceivers in WDM PON systems; they are able to carry on with the transmission and, at the same time, with the amplification of signals at the user premises. In this chapter, reflective SOAs will be investigated for WDM-PON applications. At first a theoretical model is described which predicts the optical gain and the saturation power of RSOA and compares it to an SOA made of the same material. This comparison will help to understand the RSOA behavior based on that of the well-known SOA. After that, the design of a polarization-independent RSOA for the telecom wavelengths will be presented, and experimental results from the RSOA design will be discussed. To our knowledge, this is the first demonstration of an L-band (1560-1610 nm) RSOA. The design can be easily shifted to C-band by changing the band gap of the active region. At last, the gain recovery of RSOA devices for nonlinear applications is investigated, and compared to the SOA.

2.1   Optical Amplification Principles

To achieve optical amplification, an active region is required, in which recombining carriers lead to a gain mechanism and photon emission. Carriers are supplied by a current

source and injected into the active region. The carriers occupy energy states in the conduction band of the active region material, leaving holes in the valence band. Every time an electron-hole pair is recombined, a photon is involved. The recombination of carriers can occur by three radiative processes, as spontaneous emission, stimulated emission, and stimulated absorption. In stimulated absorption, an incident light photon of energy sufficient for bandgap energy stimulates a carrier from the valence band to the conduction band. This is a loss process, because the incident photon is absorbed.

In the spontaneous emission process, the carrier decays to the valence band to spontaneously recombine with the hole, emitting a photon with random phase and direction. Spontaneously emitted photons have a wide range of frequencies, and are generally considered to be noise which lead to reduction of carrier population. If a large number of such events occur, relatively incoherent emission results, and the photons would not contribute to a coherent radiation field. This mechanism is a direct consequence of the amplification process and cannot be avoided.

If a photon of light with energy equal to the band-gap of the active region is incident on the device, it can cause stimulated recombination of the electron-hole pair. Through this recombination process, the carrier loses its energy in the form of a photon of light. The recombination process generates a photon with the same energy and phase as the incident photon, namely coherent interaction. Stimulated emission is the necessary positive gain mechanism for lasers to operate, and could happen when the number of carriers in the conduction band exceeds that of the valence band, called *population inversion*. In this case, the likelihood of stimulated emission is greater than stimulated absorption, and so the device will exhibit optical gain.

The difference between a semiconductor laser diode and a SOA is shown in Figure 2.1. A Fabry-Perot (FP) laser diode consists of a resonating cavity with the gain medium placed between the mirrors. By increasing the current above a certain threshold, population inversion is achieved, and stimulated emission overcomes spontaneous emission. So the optical power increases substantially by increasing the current beyond threshold. The laser emits coherent light only at certain wavelengths determined by its design, known as the laser modes and shown by the intensity-wavelength curve.

The SOA device has a strong anti-reflection (AR) coating applied to both facets as shown in Figure 2.1. This would keep the signal from traveling in the waveguide more than once, so the device is not as sensitive to bias current and temperature fluctuations and has less gain ripples. The SOA achieves its maximum gain through increase in current injection, so by applying more current, more optical power is achieved. The amplifier device has an amplified spontaneous emission (ASE) intensity spectrum over a broad range
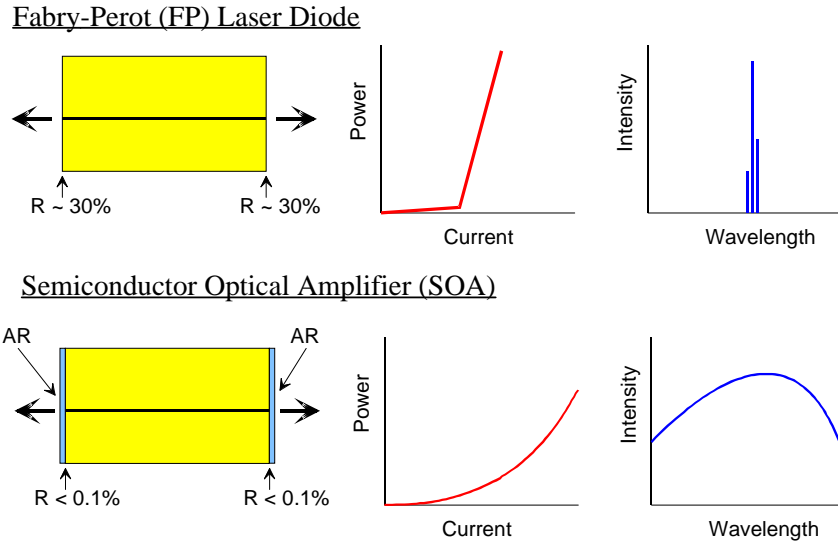
Figure 2.1: Comparison of a Fabry-Perot laser diode to a semiconductor optical amplifier in terms of power-current and intensity-wavelength curves

of frequencies, related to the spontaneous emission phenomena. The amplified input signal sits on top of the ASE noise spectrum. Although the first studies on SOAs were carried out in the 1960's, it was not until the late 1980s that studies on InP/InGaAsP SOAs were carried out to operate in the 1.3 μm and 1.55 μm regions.

2.2   SOA Specifications

SOAs are made from group III-V compound material like InP/InGaAsP or GaAs/AlGaAs, and are used in fiber optic telecommunication systems as booster amplifiers, and pre-amplifiers. They operate at telecom wavelengths for 0.85-1.6 μm. These devices are small in size, and can be integrated with lasers and modulators on a single chip. In general, several important characteristics of semiconductor optical amplifiers greatly influence the design and the operating conditions of these devices, and are introduced as follows,

- Optical gain (G): Relates to the ratio of the optical output power to the input power. Devices with high gain above 20 dB are desirable.

- Polarization dependent gain (PDG): The gain of the amplifier must support all polarization states of the incoming light, and provide equal gain to them. PDG

is defined as the ratio of amplifier gain in transverse electric (TE) mode to the gain in transverse magnetic (TM) mode, and should be equal unity for polarization independent devices designs. If polarization independent devices are not achieved, then polarization maintaining fibers are required.

- Output Saturation Power (P_{sat}): It is defined as the output power for which the amplifier gain G is reduced by a factor of 2 (3 dB) from its peak value. Increasing the input power beyond saturation point will not increase the output power further. This parameter can range from 0-10 dBm based on applications.

- Optical Bandwidth (B_o): The wavelength range for which the device is operational, and provides gain. This parameter can be presented as 1-dB bandwidth where the gain drops by 1-dB, or 3-dB bandwidth for the wavelength range before gain drops by half. In a SOA, typically 3-dB bandwidth of greater than 40 nm is desired.

- Wavelength operation (λ): The device must be operational at telecom wavelengths ranging from 800-1650 μm.

- Noise figure (NF): This parameter defines the amount of noise generated in the amplifier by spontaneous emission photons. It is a performance limiting parameter that should be as low as possible. Typical numbers range from 6-13 dB.

- Speed of device: Relates to the speed for which the device can switch between zero and one bits for direct modulation of the device. The small-signal modulation bandwidth of the SOA is limited because of its dependence on carriers lifetime, (τ),

$$f_{3dB} = \frac{1}{2\pi\tau} \tag{2.1}$$

The carrier lifetime decreases with increasing bias current, but is typically greater than 100 ps in III-V materials. This is opposed to the laser, where its modulation speed is not dependent on carrier lifetime, and its carrier density is clamped at lasing. The speed of laser is determined by the stimulated carrier density which is dependent on laser photon density [54].

The above parameters should be considered for SOA designs, and modified based on intended applications for these devices.

To introduce the operation principles behind the reflective SOA (RSOA), a schematic of this device is shown in Figure 2.2. It consists of an active gain region with higher refractive index surrounded by lower refractive index semiconductor material to keep the
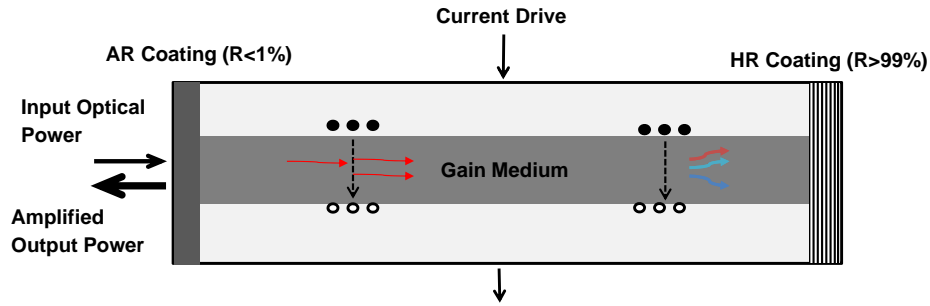
Figure 2.2: Reflective SOA devices structure

optical wave confined. Injected carriers recombine through both stimulated emission as well as spontaneous emission. The RSOA amplifier receives a low power input signal, amplifies the signal, performs any modulation, and reflects the amplified output power back.

The input facet of an RSOA is anti-reflective coated, and the other facet is highly-reflective (HR) coated with 100% reflectivity. The AR coating can be made by using multiple layers of titanium oxide/silicon oxide (TiO2/SiO2), the reflectivity will then be reduced to around 10^{-4}, with lower gain ripples. SOAs require effective reflectivity lower than 10^{-5}, which is achieved by introducing angeled facets. When light enters the cavity, it is reflected back to the input port so the RSOA has only one optical port. This is advantageous when RSOA is used at the ONU, because no additional optical element is needed for terminating the downstream signal and feeding the upstream signal onto the same fiber. The advantage of RSOA over SOA for PON applications has been discussed in the previous chapter and the schematic shown in Figure 1.11.

Figure 2.3 presents a theoretical simulation of the output vs input power of the RSOA. As the input power to the device increases, the output power starts saturating. As such, there exists two regions of operation for the RSOA device. (1) The linear region, where the input power is a linear function of the output power, and the slope is device gain. (2) The saturation region, where the output power saturates for increase in input power, and the device gain decreases. For WDM-PON applications, the RSOA must be operated in the saturation regime. This is because the slope decreases near saturation, and the input fluctuations become less apparent. It can also be seen in Figure 2.3 that the input power fluctuations due to noise are suppressed near output saturation region.
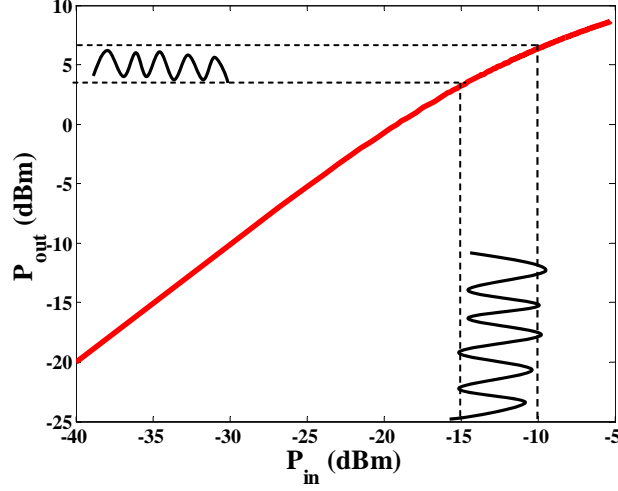
Figure 2.3: The output power of RSOA vs. input power and the saturation region

2.2.1 Optical Gain

In general, the relationship between input power P_{in} and output power P_{out} in an SOA operating at linear regime can be presented by device gain G as follows:

$$G_{SOA} = \frac{P_{out}}{P_{in}} \tag{2.2}$$

Since RSOA is a reflective device, the signal passes through it two times and the RSOA linear gain is square of the SOA linear gain,

$$G_{RSOA} = G_{SOA}^2 \tag{2.3}$$

The gain equations above do not indicate the dependence of device gain on device design and material properties. For this purpose it is best to analyze the gain as it travels through the device. The small-signal peak gain of the device, G_0, is related to the material gain g_0 as an exponential term over length of SOA, L

$$G_0 = exp(g_0 L) \tag{2.4}$$

The change in optical power at distance Z from the input end is a function of peak material gain in that section g_0, and the material saturation properties of that section P_s [55]

$$\frac{dP}{dZ} = \frac{g_0 P}{(1 + \frac{P}{P_s})} \tag{2.5}$$

26

From the above equation, the optical gain of the SOA, G, is determined by integration over L and using boundary conditions of $P(0) = P_{in}$ and $P(L) = P_{out}$ [56]

$$G = G_0 \cdot exp\left[-\frac{(G-1)}{G}\frac{P_{out}}{P_s}\right] \tag{2.6}$$

The above relation shows that the amplification factor G drops significantly from its peak value G_0 when the output power P_{out} becomes comparable to saturation power P_s. As such, P_{out} is used to characterize saturation power value for the amplifier.

2.2.2   Saturation Output Power

In order to understand the parameters effecting P_s, it is best to derive the relations that lead to saturation. To discuss gain saturation, the peak gain is assumed to increase linearly with the carrier density N

$$g(N) = a_1(N - N_0) \tag{2.7}$$

where a_1 is the differential gain (dg/dN), and N_0 is the transparency carrier density. The carrier density obeys the rate equation [54]

$$\frac{dN}{dt} = \frac{I}{qV} - \frac{N}{\tau_c} - g(N)\frac{P}{h\nu} \tag{2.8}$$

In the above equation I is the injected current, P is the input signal power, q is the electron charge, τ_c is the carrier lifetime, and V is the volume of the active region. Also h is the Planck constant, and ν is the optical frequency. Under steady-state operation, dN/dt=0 and the value of N can be obtained by substituting Eq. 2.7 in Eq. 2.8 and solving for N

$$N = \frac{PN_0}{P - P_s'} \tag{2.9}$$

P_s' is defined as the saturation intensity and given by $P_s' = \frac{h\nu}{a_1\tau_c}$. Subsequently, the saturation power P_s is defined as [57]

$$P_s = \frac{A}{\Gamma}\frac{h\nu}{a_1\tau_c} \tag{2.10}$$

Where A is the active region cross-section area, and Γ is the confinement factor. A/Γ is the amplifier mode cross-section area. Hence P_s not only depends on carrier lifetime, but also on the mode cross-section. It is also inversely proportional to the differential gain.

27

It's important to investigate the change in output saturation power (P_{sat}) with respect to changing values of saturation power P_s, and gain peak G_0. Since at output saturation power the peak gain is reduced in half that is $G_0/2$, by substituting this in Eq. 2.6, a linear dependence between P_s and P_{sat} can be found

$$P_{sat} = \frac{ln(2)G_0}{(G_0 - 2)}P_s \qquad (2.11)$$

In real applications, G_0 is much greater than 2, with numbers in order of 100 and above (>20 dB). Therefore, the Eq. 2.11 can be reduced to $P_{sat} \approx (ln(2))P_s \approx 0.69P_s$. As such, P_{sat} becomes independent of gain for large gain values.

2.3   Numerical Model for RSOA

Mathematical modeling helps the design of SOAs and predict their operational characteristics. Many models have been presented, and implemented extensively, however the assumptions made limit their capabilities, and for most of the models experimental fit parameters are used [58, 59, 57]. The most comprehensive wideband model of an SOA is based on using two complex traveling waves in negative and positive directions of a multi-section model with photon rates equal to the modulus squared of the amplitude of the traveling wave. The signal and spontaneous emission photon rates are estimated for every section, and through carrier rate equations an algorithm is run that adjusts the carrier density so the carrier rate of change at every point in the amplifier is zero. The resultant output spontaneous emission power spectral density, and signal gain are calculated. The average output photon rate and the amplifier gain profile are obtained by fitting a cubic spline to the resonant frequency points [57].

Because much experiments and designs have been accomplished for SOAs, by correlating RSOA expected performance to SOA performance, one can use this knowledge base. As such, the objective of this section is to come up with a theoretical model for RSOA based on that of an SOA. By doing so, the SOA models built over the past years could be implemented for RSOA design [60]. The two devices, SOA vs. RSOA differ mainly in their saturation characteristics, and therefore a model to compare the saturation power of the two devices under similar drive conditions is desirable. Unlike SOA, the RSOA has highest optical power at its front facet. Thus, it is expected that the saturation power of the RSOA should be lower than that of an SOA under same conditions.

In order to generate a model for gain and saturation characteristics of the RSOA, a multi-section model is used. The sections in a multi-section model are such that carrier
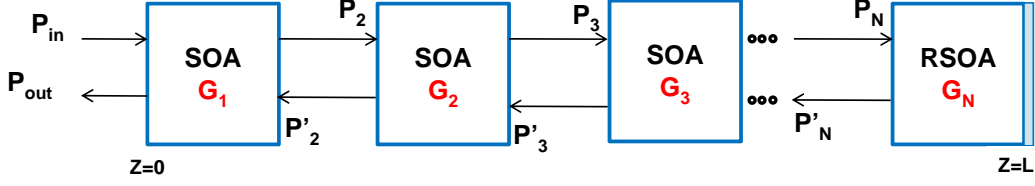
Figure 2.4: Lumped sum element approximation of RSOA

distributions are uniform across each section, and the optical gain does not change over the length of an individual section. In the model shown in Figure 2.4, the RSOA is divided into N sections. Assuming G_0 to be peak gain for single pass length of the device, the signal gain of each section is given by $G_0^{1/N}$. Following Eq. 2.6, the gain in bidirectional section k can be written as

$$G_k = \lim_{N \to \infty} G_0^{1/N} \cdot exp\left[-(G_k - 1)\frac{P_{in}(k)}{P_s}\right] \tag{2.12}$$

Every section k has two input optical signals from adjacent sections; one from forward traveling wave out of section $k-1$ and another from the backward traveling wave as an output from section $k+1$. The last section labeled by N is a reflective section, and the input power includes the forward traveling wave from section $N-1$ and the reflected amplified wave created in that section. In mathematical format, $P_{in}(k)$ is defined as the total power entering section k

$$P_{in}(k) = \begin{cases} P_k + P'_{k+1} & k \leq N-1 \\ P_k + G_k P_k & k = N \end{cases} \tag{2.13}$$

The value of G_k is dependent on the forward and backward traveling powers of the neighboring sections respectively and can be written as

$$P_{k+1} = G_k \cdot P_k$$
$$P'_k = G_k \cdot P'_{k+1} \tag{2.14}$$

Based on this model, an iterative run can be conducted for a given input power P_{in} until the output power P_{out} is stabilized to the desired accuracy. The relation between P_{in} and P_{out} determines device gain based on Eqs. 2.2 and 2.3. In the first iteration, the input and output power for all the sections are initialized to zero except for the first section, where $P_1 = P_{in}$. In subsequent iterations, the input to each section is adjusted based on the

results of the previous iteration. By using this model, an accurate comparison between the SOA and RSOA devices with same exact properties can been made. The next few plots show some results based on this analytical model.

An amplifier with N=250 sections for L=1 mm was chosen, so that each section has 4 μm length. This selection is made based on the knowledge that SOA carrier distribution is constant across this short section, and the solution converges accurately. For these sections, an iterative run was done on RSOA and SOA device considering P_s=10 dBm and the peak signal gain G_0=10 dB.

Figure 2.5 shows the normalized gain for RSOA and SOA as a function of output power. In this simulation, the SOA and RSOA have same length and current, so the gain of SOA is roughly half of RSOA. The gain for each device is normalized to its peak value. From this figure, a difference of 3.8 dB between the saturation power levels of the two device can be detected, where the RSOA is saturated earlier than the SOA. This difference is due to the reflective nature of the RSOA.
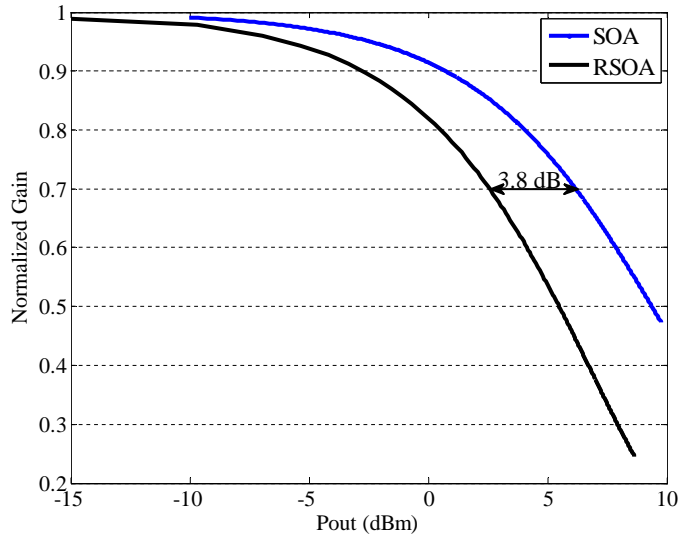
Figure 2.5: Normalized gain vs. output power for both devices

This difference is not due to the dual-length nature of RSOA; As an example, if the SOA length is doubled and the bias current is kept the same, the P_{sat} value would drop by exactly half (3 dB). Also, if both the SOA length and the current are doubled, the value of P_{sat} would not be effected. This unique difference can be written in the general form,

$$P_{sat}(SOA) - P_{sat}(RSOA) = 3.8 \ dB \tag{2.15}$$

The relation between P_{sat} and P_s for both devices is depicted in Figure 2.6. The value of P_s depends on the material and waveguide properties of the device. It is observed that the saturation power for both the RSOA and SOA increases with increasing P_s, however the difference in the saturation power levels of the two devices remains constant. Similar simulations were done by changing the G_0 while keeping P_s constant, and a constant difference between P_{sat} of the two devices was seen.

As a rule of thumb, the saturation power of an RSOA can always be considered to be roughly 3.8 dB lower than that of an SOA made from the same material and under similar drive conditions. To design a RSOA, one can just make a SOA with 4 dB higher saturation power than intended, and apply HR coating on end facet. It should be reminded that this reduced P_{sat} is not detrimental to WDM-PON performance as the application actually requires low P_{sat}.
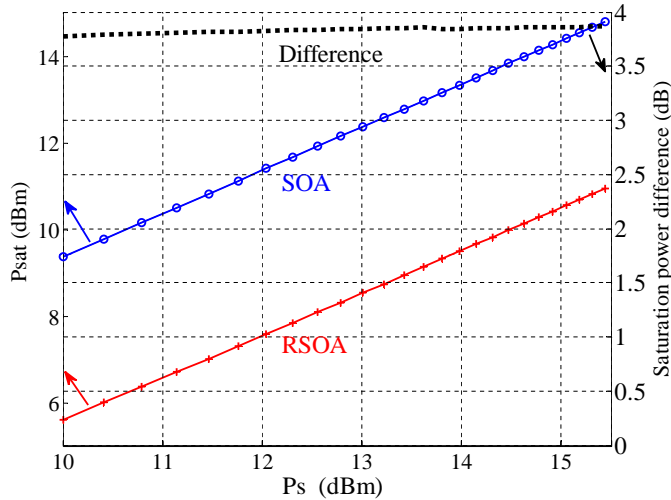
Figure 2.6: P_{sat} for SOA and RSOA as P_s is changed (G_0=10 dB)

For better understanding of the RSOA device behavior, the optical power traveling through the length of the device is depicted in Figure 2.7. The input power is chosen such that the RSOA is 3-dB saturated, but the SOA is still in linear regime. It is observed that the slope of the optical power with length for RSOA is lower in the front facet of the device, whereas it matches the SOA slope at the back facet. This means that the power at the input facet is decreased due to saturation, and the RSOA saturates at the front facet where the signal is weakest.

Figure 2.7 also shows a simulated RSOA device where the value of saturation power is set to a larger value for the front sections of this device, and reduced at the remaining

length of RSOA, while keeping the average P_s=10 dBm. By doing this, the saturation is eliminated, and the traveling power level increases at the input facet. Since saturation power is related to current flow, this suggests that increasing the current flow to the input facet of RSOA, and decreasing it at the back facet may help eliminate saturation at RSOA input facet, and improve device performance in terms of noise and P_{sat}.
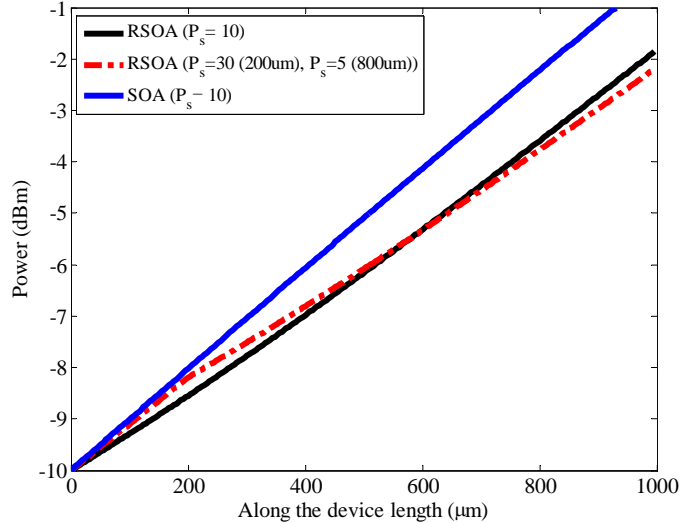
Figure 2.7: Forward traveling output power for an input power of 200 μW

2.4 L-Band RSOA Design

Polarization-independent S and C-band (1460-1530 nm) RSOAs are easily achievable with minor modification to the SOA designs [61]. However, polarization insensitive L-band SOAs have only been demonstrated in research through complex quantum well designs to provide gain at 1620 nm, and not commercially available [62]. The complexity lies in the bandgap of a latticed-matched material to InP. The compound with bandgap near the 1.65 μm region is the $In_{0.535}Ga_{0.465}As$ itself. By adding Phosphorous to this compound, the bandgap increases, which results in shorter wavelength operation.

Figure 2.8 shows the computed bandgap wavelength of InGaAs, which is the upperbound for achievable wavelength, as a function of tensile strain requirements [63]. By varying the In/Ga ratio in such a way that the lattice mismatch generates tensile strain, polarization independent operation can be achieved. From the figure it is concluded that

32

increased material tensile strain results in lower bandgap wavelength as the operational wavelength shifts to the blue side of the spectrum. Therefore it is not straight-forward to achieve longer wavelength operation with tensile-strained InGaAsP composition.
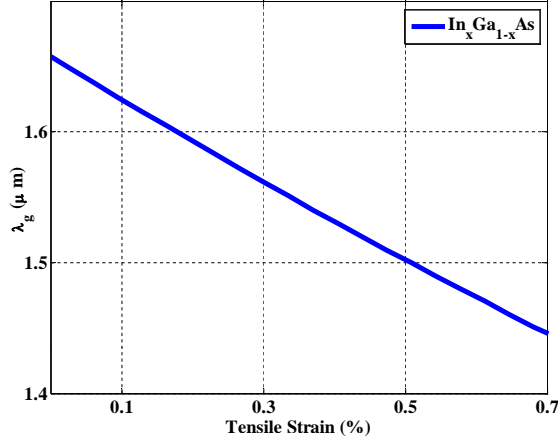
Figure 2.8: Bandgap wavelength achieved for varied tensile strain composition

However, despite SOAs, RSOA design in L-band is still possible. This is because RSOAs at ONU desire lower saturation output power, and lower carrier concentrations, which contribute to smaller bandgap filling, and longer wavelength operation. The use of lower carrier concentration requirement for this design is a novel replacement for the complex QW designs, so that well-used thin-bulk active regions with tensile strain can be deployed [64].

In this section, design and experiment of an L-band RSOA with optical parameters chosen based on system performance requirements is presented as follows: G> 20 dB over the band, PDG < 1 dB, and P_{sat}=0 dBm. These parameters were chosen based on literature search for optimized system conditions. This work is the first reported demonstration of L-band polarization insensitive RSOAs [65]. Later, other demonstrations of L-band RSOAs were reported [66].

2.4.1   Polarization-Independence

The polarization dependency of RSOAs can greatly be reduced by introduction of strain in the active region material. The material system for fiber optics telecommunication is the In_{1-x} Ga_x As_y P_{1-y} which is grown on top of InP substrate to form layers of various

energy gaps. It is found that choosing $x \approx 0.46y$ results in approximate lattice matching to InP, which is necessary to avoid defects. But for a thin active region, a small lattice mismatch can be tolerated by changing In and P composition. In this case, the material lattice structure distorts to fit the substrate lattice. This is called *strain*, and could be represented in two forms as *tensile* for smaller lattice constant ($x > 0.47$) or *compressive* strain for greater lattice constant ($x < 0.47$) than InP [67].

The gain of unstrained material exhibits strong polarization dependency, where the transverse electric (TE) gain is higher than transverse magnetic (TM) gain. This is because approximately 2/3 of the optical gain for TE comes from the interaction between conduction band (CB) and heavy hole (HH) band, which is more favorable, while 1/3 of it comes from CB and light hole (LH) band. The TM gain comes from induced optical transition only from the CB band to the LH band, which is less favorable. Under compressive strain, the HH band is closer to the CB edge than the LH band edge, and the TE mode gain is enhanced while the TM gain is further reduced. Compressive strain is used in lasers to increase gain and enhance lasing in the TE mode. Tensile strain is used to shift the HH band down in energy, and the LH up in energy. This will help enhance TM mode to exceed TE mode, and to offset the polarization dependency of active structures.

The gain of SOA devices is presented by $G = e^{(\Gamma g - \alpha)L}$, where Γ is the mode confinement factor, g is the material gain, α is the material losses, and L is the device length. Neglecting polarization dependent losses, PDG can be written quantitatively in terms of modal gains [68],

$$PDG = \frac{G_{TE}}{G_{TM}} = e^{\left(\Gamma_{TE} g_{TE} - \Gamma_{TM} g_{TM}\right) L} \tag{2.16}$$

It can be seen from the above equation that to achieve PDG of less than unity, both waveguide mode shapes and active region design needs to be considered. Applying the correct amount of strain balances the gain difference induced by the confinement factors and minimizes PDG.

2.4.2   Modal Properties

The confinement of TE mode in the active region is greater than TM mode, i.e., $\Gamma_{TE} > \Gamma_{TM}$. To compare the mode shapes, a simulation was run using *FIMMWAVE* mode solver package, which uses Finite Element Method [69], to visualize optical modes and calculate mode confinements.

The modeled structure of the RSOA is based on the design rules of the commercial foundry that fabricated the device. The design rule asked for the waveguide width to be

3.2 μm, and the length of the chip to be 1 mm. The active region of the structure is sandwiched by a double step Separate-confinement heterostructure (SCH) layer of 100 $\mathring{A}$ and 200 $\mathring{A}$ each. The SCH is a thin layer of higher bandgap material with an index between that of the active material and the substrate, which helps with carrier confinement as well as modal confinement. Further, the InP cladding layer is etched to ensure proper modal confinement for this waveguide width, and the residual cladding thickness is 200 nm.

The modal analysis is shown in Figure 2.9, where the fundamental TE mode shape of the rib device is compared to its TM mode. It can be seen that the TM mode is further spread out of the active region in vertical direction, and so its confinement is less.

(a)   (b)
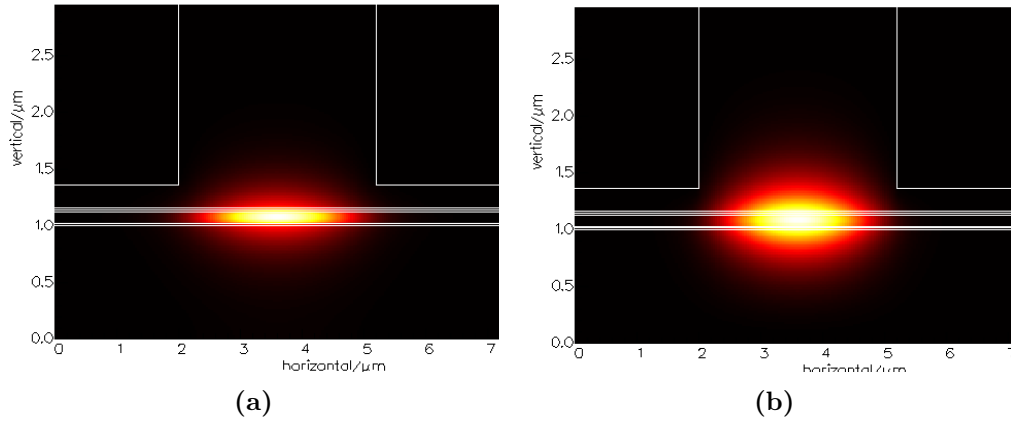
Figure 2.9: RSOA device mode analysis (a) Fundamental TE mode, (b) Fundamental TM mode of the device

Also, decreasing the active layer thickness increases the confinement ratio between the TE and the TM modes, Γ_{TE}/Γ_{TM}, which is shown in Figure 2.10. Hence, more tensile strain is needed to compensate for increased TE-TM optical confinement ratio. Increased tensile strain requirement due to very thin active regions inhibits operation in the L-band by decreasing the bandgap wavelength, shown in Figure 2.8.

2.4.3 Active Region

Figure 2.11 shows the calculated strain required to keep the PDG $\leq$ 1 dB over the complete L-band for different thickness in the active region. In this calculation, the difference due to the confinement factors for the quasi TE and TM modes and the coupling efficiency due to difference in mode shapes were taken into account. In order to achieve PDG of less than 1 dB, the strain requirement varies from 0.1% to 0.33% in the active region.

35
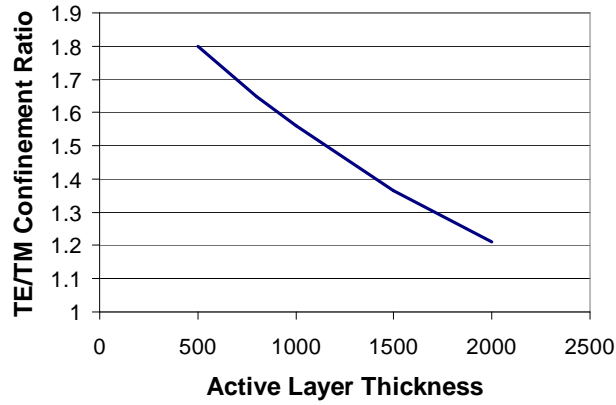
Figure 2.10: TE/TM confinement ratio difference for different active layer thickness

For this design, the active region of the device was chosen to consist of a 0.1 μm thick 0.17% tensile strained InGaAsP bulk layer containing of 2% P content. The active region thickness below this increases the tensile strain in such order that reduces the bandgap wavelength well below 1.6 μm, as depicted in Figure 2.8. Therefore good L-band operation cannot be achieved with lower than 0.1 μm active region thickness.
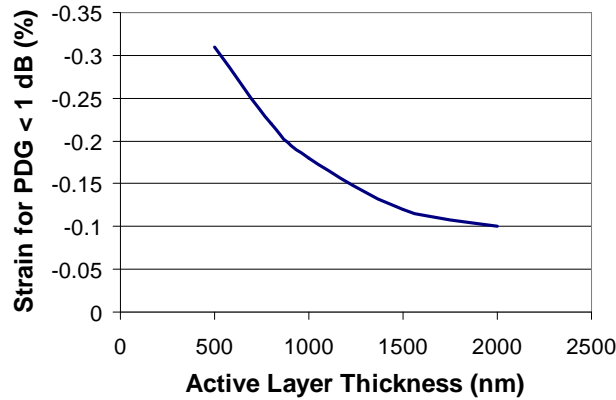
Figure 2.11: Strain required for PDG of less than 1 dB over the L-band

2.4.4 Single-Angled Facet

SOA devices can provide amplification when reflection feedback from the end facets is suppressed, where the reflectivity must be extremely small (<0.1%). The tolerable value of

the facet reflectivity can be estimated by considering the small-signal gain of a Fabry-Perot SOA, and calculating the ratio of maximum to minimum gain of the amplifier [55]. This ratio is called the amplifier *gain ripple* (ΔG), and written as a factor of facet reflectivities R_1 and R_2 as well as Gain G,

$$\Delta G = \frac{1 + G\sqrt{R_1 R_2}}{1 - G\sqrt{R_1 R_2}} \tag{2.17}$$

To obtain a gain ripple of less than 1.5 dB at an amplifier chip gain of 28 dB, the geometric mean facet reflectivity is calculated from Eq. 2.17 to be $\sqrt{R_1 R_2} < 3.17 \times 10^{-4}$. For an RSOA with back facet reflectivity of R_2=0.9, the required facet reflectivity for front facet is therefore $R_1 < 1.1 \times 10^{-7}$. This requirement cannot be achieved with just AR coating, and a special device structure is needed.

For this purpose, an angled facet structure can be deployed such that the waveguide is at an angle to the facet, and reflectivity is less than 10^{-4} due to the angle itself. Since a RSOA needs high reflectivity at the back facet, the waveguide needs to be of normal incidence to the back facet. As such, a bend in the waveguide can be used to accomodate the angled front facet design. Such type of waveguides are called 'single-angled facet' (SAF) waveguides.

To calculate the desired angle for reflectivity, the reflection loss should be less than 10^{-4} for the design. The reflectivity from an angled facet can be approximated by the following, assuming a Gaussian field distribution [70]

$$R = R_0 \cdot exp\left[-(\frac{2\pi n_2 W_o \theta}{\lambda})^2\right] \tag{2.18}$$

R_o is the Fresnel reflectance between the waveguide and air, given by $R_0 = (\frac{n_2 - 1}{n_2 + 1})^2$ when the transmission and reflection are at the right angle to the facet. n_2 the effective refractive index of the waveguide, W_o the mode width, θ the angle from normal of the facet, and λ the wavelength of the device. The mode width is related to the waveguide width W through the following relation [70]

$$\frac{W_o}{W} = \frac{1}{\sqrt{2}}\left[9.2063 \times 10^{-3} + \frac{1.7265}{\sqrt{V}} + \frac{0.38399}{V^3} - \frac{9.1691 \times 10^{-3}}{V^5}\right] \tag{2.19}$$

The V-number of the waveguide is presented as follows where n_1 is the effective refractive index of the cladding region

$$V = \frac{\pi W}{\lambda}\sqrt{n_1^2 - n_2^2} \tag{2.20}$$

37

For this design, by choosing the angle $\theta = 6^o$ and for n_1=3.2, n_2=3.22, W=3.2 μ m, and λ=1.55 μm, the reflections back into the waveguide due to angled facet are around 10^{-6}.

Further, the bend in the SAF design needs to accommodate bend losses up to a maximum of 0.5 dB. Since bend in the waveguide can induce mode leakage, the bend loss is represented by $P(s) = P(0)exp(-\alpha_b.s)$, where α_b is the attenuation coefficient [71]. By choosing a 6° angle, a bend radius of 3 mm is accommodated with losses less than 0.5 dB. This along with 2 layer AR coating reduces the reflections below 10^{-6}.

2.4.5 Final Device

Considering the above design parameters, the final RSOA design geometry is shown in Figure 2.12, and the material layer structure is presented in Table 2.1. The RSOA consists
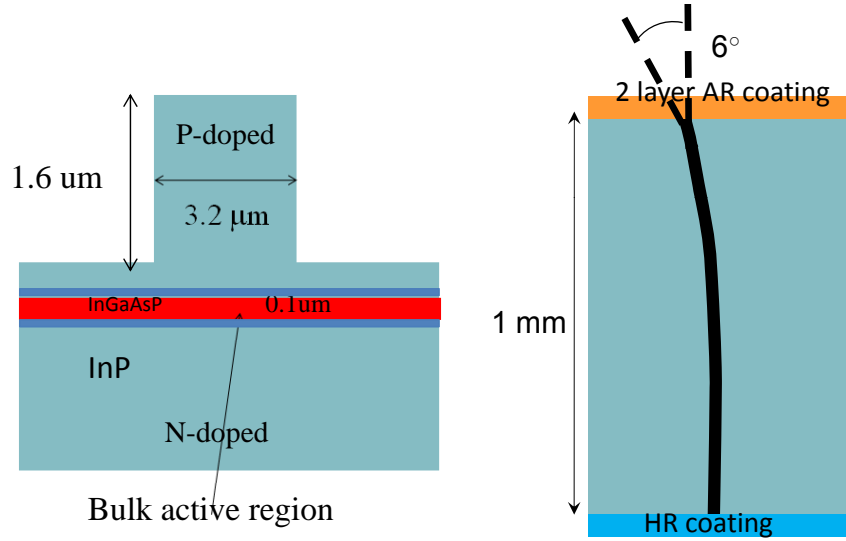
Figure 2.12: RSOA ridge angeled device to reduce reflections

of 0.1 μm active region (InGaAsP) surrounded by two separate confinement heterostructure layers (SCH) of 100 $\mathring{A}$ and 200 $\mathring{A}$ each (InGaAsP with larger bandgap). The upper clad (InP with large bandgap) is p-doped, and the doping in the amplifier is varied exponentially from 3e17 to 1e18 cm^{-3}. The n-doping in the lower clad (InP) is n = 7e17 cm^{-3}. The cap layer consists of P$^+$ doping of P$^+$ = 2e19 cm^{-3}. The cap layer is below the metal layer, and together they form the Ohmic contact. The metals on the substrate n-doping are Ni/Ge/Au/Ni/Au. For the p-doping contacts, the metal layers are Ti/Pt/Au.

Layer No.	Layer Name	Material	$\lambda_g(\mu m)$	Strain %	Thickness (μm)	Index
9	Cap	InGaAs	1.64	0	0.1	3.643
8	UpperClad	InP	0.92	0	1.8	3.167
7	SCH	InGaAsP	1.1	0	0.02	3.282
6	SCH2	InGaAsP	1.25	0	0.01	3.378
5	Active region	InGaAsP	1.58	-0.17	0.1	3.59
4	SCH2	InGaAsP	1.25	0	0.01	3.378
3	SCH	InGaAsP	1.1	0	0.02	3.282
2	Lower clad	InP	0.92	0	1	3.167
1	Substrate	InP	0.92	0	100	3.16

Table 2.1: L-band RSOA material structure

The wafer for the device was grown in a commercial foundry with solid-source molecular beam epitaxy (MBE). A 3.2 μm ridge semiconductor single-angled stripe with an angle of 6° on the front facet was processed using standard lithography and metalization techniques [72]. The back facet was coated at greater than 90 % reflectivity. The RSOA chip was mounted p-side down on a ceramic sub-mount. Further, the chip was packaged in a 14-pin butterfly package with standard single mode fiber. The coupling loss between the RSOA chip and the optical fiber was estimated to be 4 dB.

The angled waveguide facet of 6° helps eliminate reflections back into the device, and along with the AR coating will reduce reflections to 10^{-6}, and also eliminate higher oder modes. This RSOA rib-structure device supports 2 fundamental modes. The higher order asymmetric modes are very difficult to excite due to low current density and low output powers in the order of μW.

2.5   Experimental Measurements

To measure the performance of the device, a setup shown in Figure 2.13 was used. The input optical signal from a 1590 nm DFB laser was injected into the device through a variable optical attenuator (VOA), which is used to adjust the input signal power. A polarization controller is used for the purpose of tuning the input signal polarization, and measuring the polarization dependent gain. The RSOA device must accompany a circulator, since both the input and output ports are the same. The circulator device is only for testing purposes, and is not required in deployment of RSOA at WDM-PON ONUs. The coupling loss per port for the circulator is 1 dB and has been corrected for the results shown later in this text. The input power signal was tapped by a 10:90 division coupler

and calibrated to estimate the input power while measuring the saturation characteristics of the device.
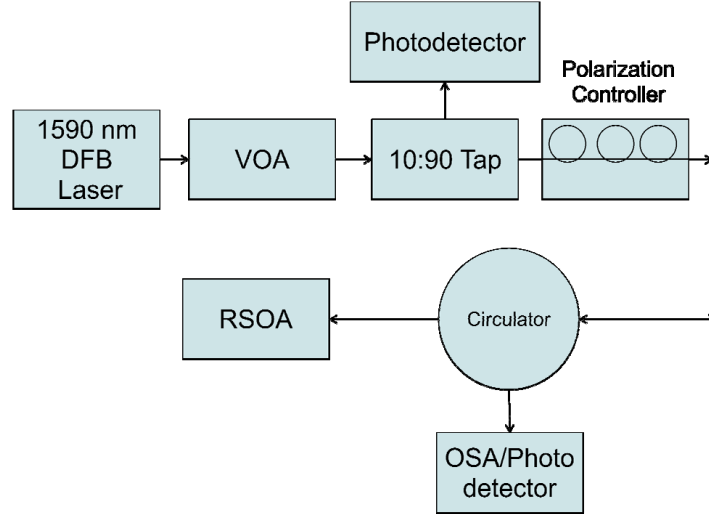
Figure 2.13: Experimental Setup for measuring RSOA characteristics

Figure 2.14 shows the polarization resolved ASE spectrum from the unpackaged chip. To measure the polarization resolved spectrum, the ASE from the chip was collimated and passed through a polarizer and coupled into an optical spectrum analyzer through a single mode fiber. The TE and TM spectrum were measured by changing the state of polarization. Further, to account for any coupling changes, the polarization resolved optical power was also measured and the measured spectrum was normalized by respective optical powers. The 3-dB bandwidth for the TE and TM modes were approximately 42 nm and 45 nm respectively. The peak wavelengths for both the polarizations were nearly 1575 nm.

The ASE noise spectrum of the RSOA is presented by $P_{ase} = h\nu n_{sp}(G-1)B_o$, where $h\nu$ is the photon energy, n_{sp} is the population-inversion factor, B_o is the optical bandwidth, and G is the device gain. Due to the direct relation of P_{ase} and G, the ratio of ASE spectra for TE and TM modes depicts PDG.

The PDG ascertained from the ASE measurements is measured to be less than 0.8 dB over the complete L-band and is plotted on the same chart. Also the gain flatness over the complete L-band (1570-1610 nm) was better than 4 dB. The peak gain was intentionally kept at a lower wavelength as the NF increases appreciably for wavelengths shorter than

40

the peak gain. However, if better gain flatness is required, the same design can be shifted in wavelength by approximately 20 nm using a ternary InGaAs material with the same strain. The gain ripple was also measured and found to be 1.06 dB.
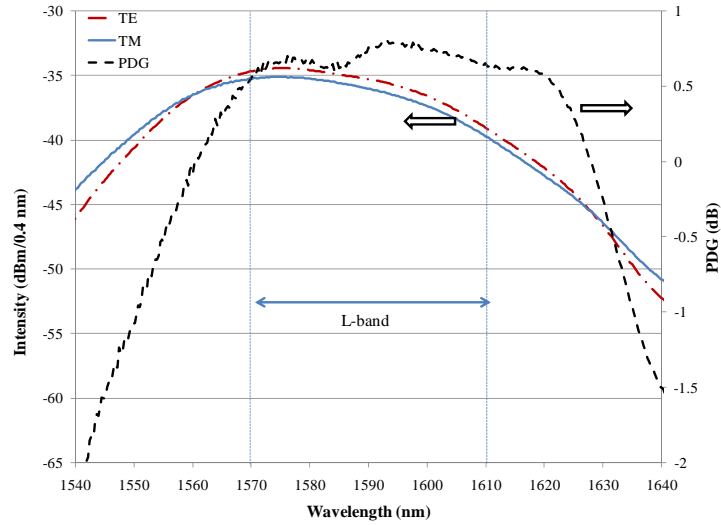
Figure 2.14: Polarization resolved ASE spectrum for RSOA

The fiber to fiber packaged gain versus output power is shown in Figure 2.15 at a bias current of 200 mA and chip temperature of 25 ^{o}C. The simulated curve is also plotted. For the calculation, a value of G_o was fit to match the maximum gain curve and was found to be 16 dB. P_s=9 dBm was determined from theoretical models. A packaging loss of 4 dB was also accounted for in the calculations. A minimum optical gain of 24 dB is achieved at 1590 nm at a current of 200 mA.

Using the ASE curve as reference, the optical gain should be greater than 21 dB over the complete L-band. The PDG was less than 0.6 dB and compares very well with the expected PDG from the spectral measurements at 1590 nm (0.76 dB) validating the fact that the PDG will be less than 1 dB over the whole L-band. The output P_{sat} was approximately -1.0 and -0.7 dBm for the maximum and minimum gain, respectively. It is approximately 1 dB less than the modeled value. A similar difference is generally seen in our SOA modeling also.

The optical gain was also measured with different operating current from 160-300 mA and is shown in Figure 2.16 for the two polarization states. The optical gain increases with current while the PDG also increases but remains below 1.2 dB even for currents up to
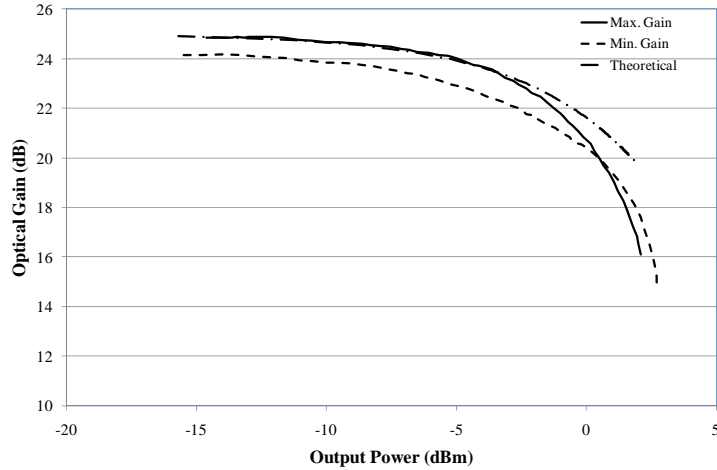
Figure 2.15: Gain versus output power for the RSOA

300 mA. It should be noted that the peak gain value and the spectral width change with increasing current. At I=300 mA, the peak gain is at 1570 nm and the 3 dB spectral width is at 48 nm.

For comparison, an SOA of same length and ridge width was also made from the same wafer and packaged in the same way and had an output saturation power of 3.2 dBm at an operating current of 200 mA. Thus, the difference in saturation powers was 4.2 dB as opposed to 3.8 dB expected by theory.

NF in the signal-spontaneous beat noise limit for the RSOA and SOA was also measured. While the RSOA exhibits a NF=10 dB, the SOA has a NF=8 dB. The accuracy of the measurement was around 0.5 dB. Since the coupling efficiency is expected to be similar, we believe this difference in NF is due to the fact that the RSOA is saturated at the input itself. The NF of an RSOA is described in detail in the next section.

2.6   Speed of RSOA Device

RSOAs at the ONU are used for intensity modulation. Intensity modulation can be achieved by modulating the amplifier current with a data stream of bits. The current modulation effects the carrier density in the amplifier, and thereby the input signal. The carrier density temporal response is dependent on the carrier lifetime, and so the modulation bandwidth is limited by the amplifier carrier lifetime. The modulation bandwidth
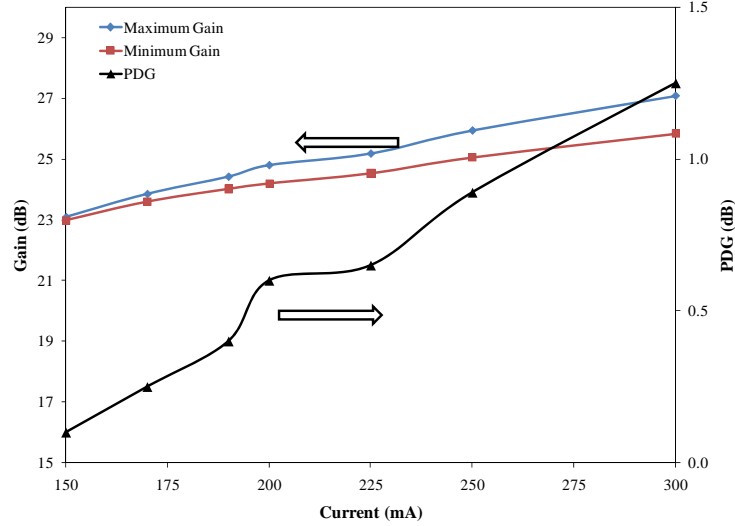
Figure 2.16: Maximum and minimum gain for different operating currents

can be measured by applying a small signal electrical current to the RSOA devices, and measuring the modulated optical output power. The electro-optic (EO) ratio of the two measurements is presented by,

$$EO(f) = \frac{\Delta P(f)}{\Delta I(f)} \tag{2.21}$$

The frequency at which the EO ratio drops to half of the maximum value indicates the RSOA modulation bandwidth [73]. The modulation characteristic of the RSOA was measured at input power of -20 dBm. The bias current on the RSOA was 200 mA and a small signal modulation was added through a bias T. The EO modulation characteristics was manually measured by using a pulse generator for sinusoidal modulation and looking at the response on a digital communication analyzer for change in peak-to-peak amplitude of the sinusoidal wave with increased frequency. The relative EO response was then calculated,

$$EO_{rel}(f) = 10 \cdot LOG \left(\frac{EO(f)}{EO(100Hz)} \right) \tag{2.22}$$

The relative EO response is shown in Figure 2.17. An external 47 Ω RF load was placed in series with the RSOA to match the impedance. The 3-dB bandwidth for the device is measured to be 1.3 GHz. As such the device should be suitable for 1.25 Gbps modulation and may even be suitable up to 2.5 Gbps modulation depending on the modulation format.

43
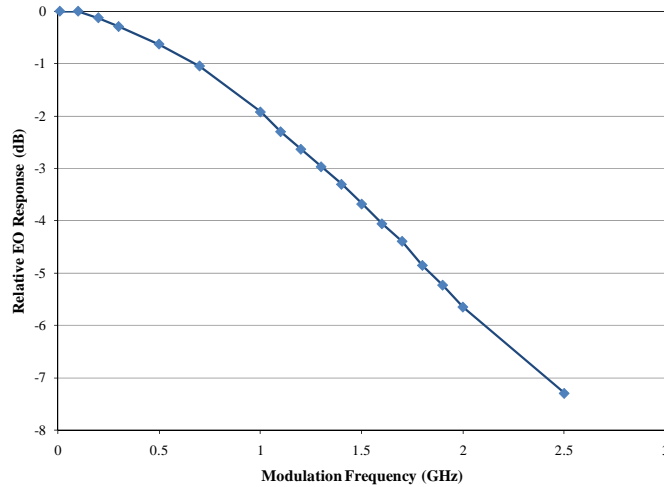
Figure 2.17: Modulation characteristics of the device

Although 2.5 Gbps transmission can be achieved [74], direct modulation of the RSOA limits the performance. Further compromise has to be made between the modulation and optical gain functionalities of the device as high speed modulation desires short length device where as longer length works better for high gain functionality. Therefore, to increase the bit-rate of an RSOA-based system, an external modulator should be monolithically integrated with the RSOA to separate the two functionalities. The modulator can be an electro-absorptive modulator (EAM) or an electro-refraction based Mach-Zehnder modulator. By separating the two functionalities, it is possible to make a device that can operate at speeds greater than 10 Gbps. Although we had this shortcoming in mind, and started proposing such solution, we later came across similar work in [75, 76], therefore this problem has been approached with a reasonable solution.

2.7 RSOA Dynamic Response

Earlier it was seen that the RSOA has approximately 3.8 dB lower output saturation power as compared to the SOA. The difference in carrier dynamics of the two devices can modify the gain recovery response of the two devices. The gain recovery time is defined as the time it takes for the gain to reach from 10% to 90% of the maximum value; i.e the time it takes for the carrier density to replenish itself, after a saturating pulse has passed through the device. The gain recovery time is of the order of 10 ps to 1 ns [77]. A simple model

shows the dependance of gain recovery on P_{sat}, G and τ_c. The model assumes no ASE noise, exponential power increase along the length of amplifier [78]. The recovery time can be approximated as

$$\Delta t = \frac{2.2\tau_c}{1 + G_{probe}\frac{P_{probe}}{P_{sat}}} \tag{2.23}$$

From the above discussion, assuming two devices with similar dimensions and device parameters, the RSOA will possess faster gain recovery time, due to higher gain and lower P_{sat}.

A numerical simulation was also run to compare the carrier dynamics of two devices in further detail. For this purpose, the pump-probe configuration is used. The sketch of the method is shown in Figure 2.18. A train of short pico-second pulses (pump) are sent through the device, which is operating under a cw laser source (probe), and the response is captured using an oscilloscope. The schematics of the VPI model and the parameters used for the active region of devices are illustrated in Appendix A. The parameters are taken from real values found in literature [77].
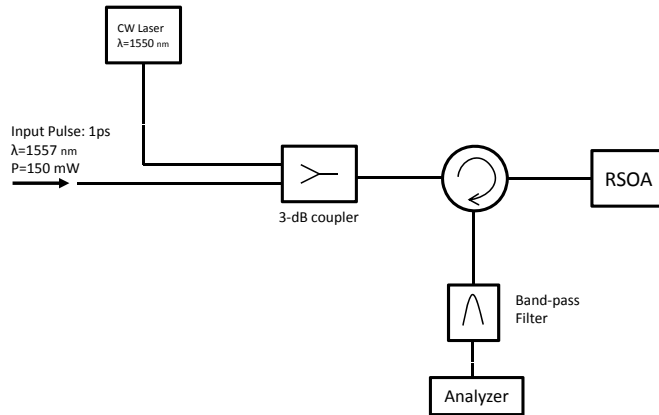
Figure 2.18: Configuration of pump-probe measurements for RSOA

A continuous wave probe signal at a wavelength of 1553 nm with -14 dBm input power was injected into the devices. For direct comparison, 2 devices were considered, the RSOA, and the SOA with twice the length and operating at twice the current. This is to equalize the gain produced by both devices, because response time is directly proportional to device gain and carrier density. The pump pulse was injected into the devices to drive the device in saturation, and was filtered with an ideal optical filter and the optical power on the probe signal was calculated. Figure 2.19 shows the evolution of the optical power in the

probe signal for the SOA and the RSOA respectively. For the SOA, the gain recovery time is measured to be 200 ps whereas for the RSOA, it is 176 ps. An improvement in gain recovery time of 13% can be achieved in the RSOA as compared to the SOA. This is because of the different saturation dynamics which happen in RSOA, and have been discussed in Chapter 3.
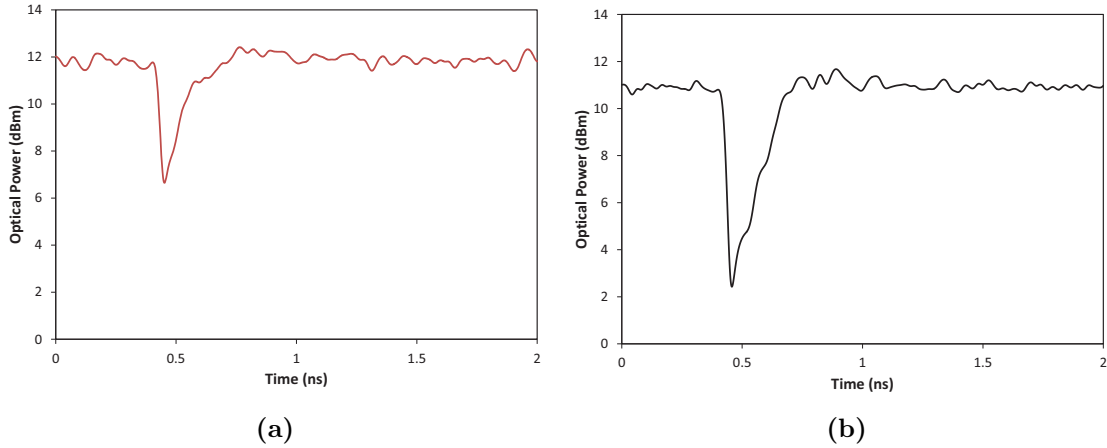
Figure 2.19: Dynamic Response of optical amplifiers (a) SOA (b) RSOA

Instead of using a standard SOA, if we make a reflective SOA from the same material, the gain recovery time is inherently improved. RSOAs can be made suitable for optical non-linear applications. In these applications, the device is driven into saturation by high input power which results in different non-linearities like the cross gain modulation (XGM), cross-phase modulation (XPM), and four wave mixing [79].

2.8 Summary

SOAs are not appealing for applications as inline amplifiers, as they cannot compete with Erbium doped fiber amplifiers (EDFA) due to low saturation output power, and the requirement to operate them in linear regime. However, the ability to perform as transceivers, small size, and the ability to integrate them with other optical functionalities on a single chip make these semiconductor amplifier devices very attractive for optical communication applications.

For WDM-PON ONUs, with single fiber terminations, it is desired to combine input/output ports into one, and reflective SOAs are a better solution. RSOAs with HR

Parameter	Desired	Min Achieved	Max Achieved
Peak Wavelength	L-band	1570 nm	1610 nm
Gain	> 20 dB	23 dB	26 dB
P_{sat}	0 dBm	-0.7 dBm	-1 dBm
PDG	< 1 dB	0.6 dB	1.2 dB
NF	low	-	10 dB
Gain ripple	low	-	1.06 dB
3-dB Bandwidth	> 40 nm	-	48 nm
Bias Current	low	160 mA	300 mA

Table 2.2: Desired and achieved specs for L-band RSOA operating at I=200 mA

coating on one facet reflect the signal power out the same port while amplifying it, they can also modulate the light at the same time. For this application, it is desirable to operate near the saturation region of these devices to lower the RIN noise due to input power level fluctuations.

Although SOA amplifiers are well-understood and commercially available, they have higher saturation output powers, and therefore the designs could be different from a reflective SOA. To use previous knowledge on SOA design to properly demonstrate an RSOA which is polarization-insensitive, it's important to compare the features of the two devices. The analytical model was created for this purpose, and it's shown that the RSOA saturation power is 3.8 dB less than that of SOA. In addition, the device saturates at its input facet, so the saturation power is low.

Based on known SOA designs, L-band RSOA was designed, where by introduction of slight tensile strain in the active region, polarization independence was demonstrated. The device uses thin bulk active region in InGaAsP surrounded by P and N doped layers of InP. The rib structure was simulated to be 3.2 μm, supporting two TE modes. The waveguide was angled to reduce reflections and dissipate higher order modes. In this device, polarization dependent gain was measured to be around 1 dB over the L-band. Optical gain of greater than 21 dB and gain flatness better than 4 dB is also achieved. The RSOA design can easily be shifted to other operational bands by changing the phosphorous composition. The desired and achieved specs for this device are listed in Table 2.2.

Another feature of RSOA devices is the improved gain recovery time which makes these devices suitable candidates for non-linear applications. It was numerically shown that gain recovery time of RSOA can be improved compared to SOA made from the same material and operating under identical conditions. A 13% improvement in gain recovery time is shown with the RSOA using half the length and half the current for the SOA.

Chapter 3

Noise performance of RSOAs

The performance of semiconductor optical amplifiers can be effected by the amount of noise they add to the optical systems. As in electronics, it is common to quantify the effects of noise on a device using its NF, which is a parameter showing the amount of noise added to the signal due to the amplification process of spontaneously generated photons in the amplifier. In an optical amplifier, a lower NF is desired for optical performance, and to achieve higher bit error-rates (BER) [80]. The noise figure is usually expressed in dB with typical values of 6-12 dB for commercial SOAs. The NF is considered to be a critical parameter for RSOA applications in WDM-PON and should be as low as possible if used as a preamplifier, since it determines the lowest achievable sensitivity value [81].

During our literature search [74] and comparison of commercially available devices from *Kamelian* [37] and *CIP Photonics* [82], the NF of RSOA is higher than that of the SOA though it is generally attributed to lower coupling efficiency. In addition, for the reported devices in chapter 2, a higher NF in RSOA was observed as opposed to SOA for the same device configuration. We believe this increased NF could be due to the fact that the RSOA saturation and hence the carrier density is lowest in the input where the signal is the weakest.

In this chapter, the increased RSOA NF is theoretically modeled and related to the carrier dynamics of the device. In addition, and the operating conditions effecting the NF are experimentally verified. Later, the effect of RSOA NF on WDM-PON system performance in conjunction with receiver noise statistics is investigated through theoretical modeling as well as system-level simulations.

3.1 Analytical Analysis of RSOA NF

In this section, the goal is to determine the carrier dynamics throughout the device length and thus the NF of amplifier device. NF of the amplifier is related to the ASE noise power generated in the device. If P_{in} is the input power to the RSOA device, it's output power P_{out} consists of amplified input power by the amplification factor gain, G in addition to the added ASE power P_{ase}

$$P_{out} = GP_{in} + P_{ase} \tag{3.1}$$

The ASE noise power (P_{ase}) of an RSOA over the optical bandwidth B_o is presented by [83]

$$P_{ase} = mh\nu n_{sp}(G-1)B_o \tag{3.2}$$

In the above equation h is plank's constant, m is the polarization factor, ν is the operating frequency, and n_{sp} is the population inversion factor. ASE noise degrades the system performance by increasing the bit error rate of the system.

In terms of definition, noise figure is defined as the ratio of electrical signal-to-noise ratio (SNR) detected at the input of the amplifier (SNR_i) to that of the signal at the output of the amplifier (SNR_o), and for large enough amplifier gain can be approximated by the n_{sp} factor assuming most amplifier noise is due to signal-spontaneous beating terms [84]

$$NF = \frac{SNR_i}{SNR_o} = \frac{2n_{sp}(G-1)+1}{G} \approx 2n_{sp} \tag{3.3}$$

The theoretical lower limit for NF is when the SNR degrades by a factor of 2 (3 dB), resulting in NF=2. In ideal case, total population inversion is achieved and N_1=0. However, in reality an SOA will exhibit higher noise figure due to presence of spontaneous emission factors, as well as low coupling efficiencies at the input. When population inversion occurs, the n_{sp} factor determines the amount of carrier inversion, and can be written as follows assuming material loss to be α

$$n_{sp} = \frac{N_2}{N_2 - N_1}\frac{g}{g-\alpha} \tag{3.4}$$

In the above equation, N_2 is the population of electrons in the excited state, N_1 is the population of electrons in the ground state, and g is the linear gain coefficient. The relation between optical gain (G), and gain coefficient (g) is an exponential of the form $G = exp(gL)$, where the total device length is given by L.

N_2 can be written as a function of N_1, through the gain coefficient g, and the peak gain coefficient g_o

$$N_2 = \frac{g}{g_o} + N_1 \tag{3.5}$$

Combining Eqs. 3.4 and 3.5, n_{sp} can be expressed through known initialized parameters as a function of g

$$n_{sp} = \frac{g + g_0 N_1}{g - \alpha} \tag{3.6}$$

To help understand the carrier dynamics along the length of amplifier device, we develop a multi-section model similar to the model described in Chapter 2 with N sections, so that gain of section k is determined by the following relationship with the assumption that P_s is the material saturation power and G_0 is the peak gain of the RSOA device,

$$G_k = \lim_{N \to \infty} G_0^{1/N} \cdot exp \left[-(G_k - 1) \frac{P_{in}(k)}{P_s} \right] \tag{3.7}$$

The input power to each section of the device, $P_{in}(k)$, is from the output of the previous section plus the ASE power generated in that section. The traveling power into each section of the multi-section model is labeled in Figure 3.1. Since the RSOA device is of double pass nature, the input power to each section consists of forward and backward traveling signals. Assuming P_i to be the input to section k, and P_o to be the backward traveling signal into that section, the expressions relating the power distribution to each section k can be written as follows

$$P_i(k) = G(k-1)[P_i(k-1) + P_{ase}(k-1)] + P_{ase}(k)$$
$$P_o(k+1) = G(k+1)[P_o(k+1) + P_{ase}(k+1)] + P_{ase}(k)$$
$$P_{in}(k) = P_i(k) + P_o(k+1) \tag{3.8}$$

For the last section N with high-reflective coating, $P_i(N+1) = P_o(N+1)$.

By inserting the input power value for each section into Eq. 3.7, the gain of that section can be determined. Through multiple iterations, the values of gain and input power are stabilized to the calculated values. The total gain of the device can then be obtained from the resultant output power of the device P_{out}. The total ASE output power from the multi-section device is the value of $P_{ase}(1)$ for the RSOA and $P_{ase}(N)$ for the SOA device. The n_{sp} factor can be calculated form the total ASE power output from the device using Eq. 3.2. Finally, the NF of the device can be obtained using Eq. 3.3.
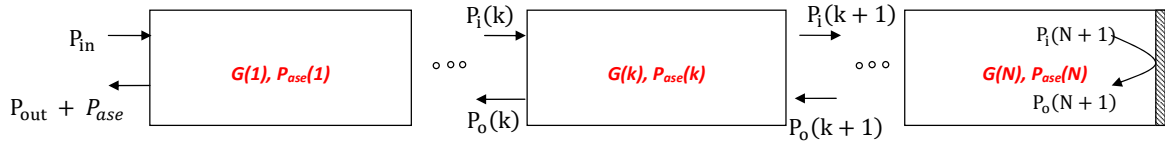
Figure 3.1: Multi-Section model to analyze RSOA noise

In this model, similar to Chapter 2 simulations, the device has N=150 sections with total device length of L=600 μm. The single-pass device gain is set to G=16 dB, and the material loss is assumed to be α=30 cm^{-1}. The optical bandwidth of the device is assumed to be B_o=3 THz equivalent to about 25 nm.

Figure 3.2 illustrates the carrier dynamics throughout the RSOA length. The initial carrier density is given the value N_1=1.5$\times10^{24}$ m^{-3}. The initial carrier density is chosen based on standard values found in literature. Figure 3.2a shows that through carrier inversion, the carrier density of RSOA decreases by more than an order of magnitude before saturating at the input facet. Also, as the input power into the device increases, more carriers are injected, so the saturation effects are greater. This is the reason for gain saturation of SOA type devices at a certain input power threshold.

(a)

(b)
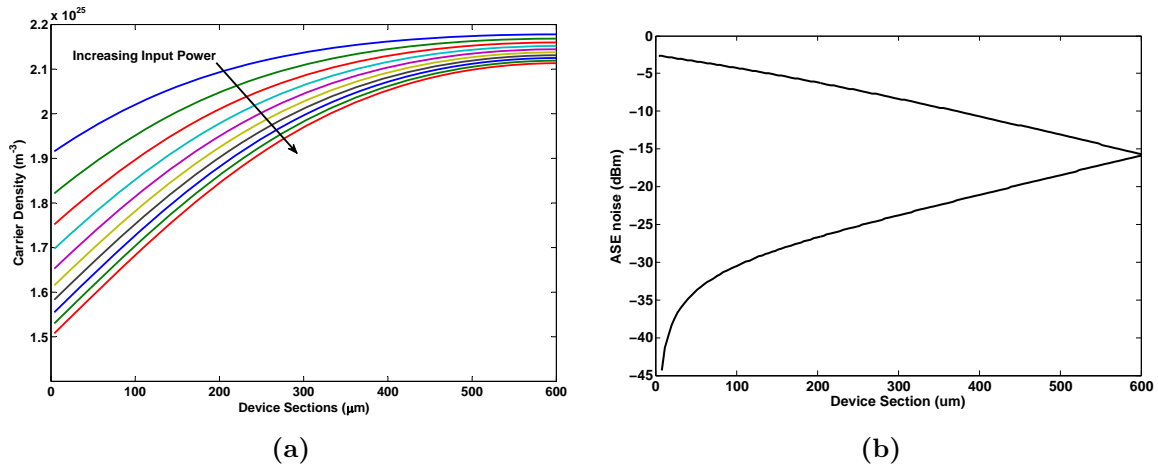
Figure 3.2: Carrier dynamics of RSOA (a) Carrier saturation near the input of the device (b) ASE noise amplification throughout the length of device

The ASE noise (P_{ase}) amplification process is shown in Figure 3.2b for an input power value of P_{in}=10 μ W. The spontaneous emission phenomena is an unwanted side effect from the semiconductor amplifier devices, which amplifies throughout the length of the

device. Further, more spontaneous emission (SE) noise is generated as the signal travels through the device. P_{ase} reaches its maximum value at the front facet of the RSOA, the amplification process decreases as the carriers move into saturation for the second pass into the device.

In Figure 3.3, the NF of both devices RSOA and SOA are plotted as a function of output power. As the input power of an amplifier device increases, the NF of that device increases, and the saturation effects are much greater for the RSOA device. In this example, the RSOA NF increases by 1.5 dB as the device moves into saturation. For the SOA device however, the increase in NF is less than 0.5 dB. It should be noted that both devices possess the same material and device characteristics, as well as same operating conditions.
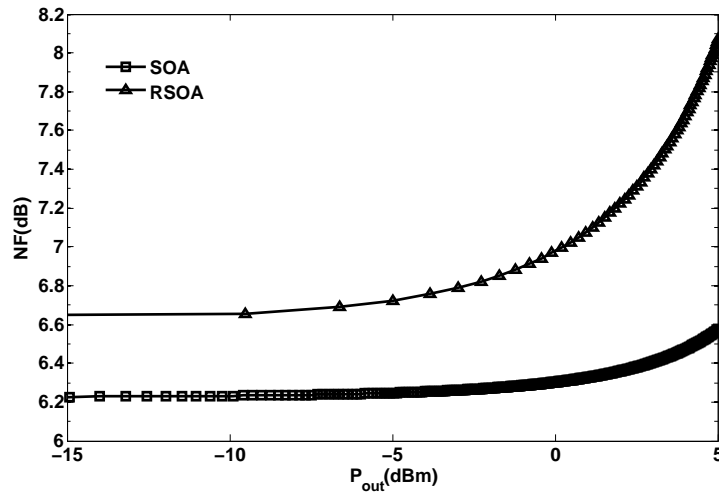
Figure 3.3: Comparison of NF variations between SOA and RSOA as a function of output power

The above analysis assumes no fiber coupling loss of the amplifier, so the chip NF in the plot assumes 100% coupling efficiency. Coupling losses degrades the noise figure of the amplifier. Assuming the coupling efficiency, C, to be a fraction of unity, NF of the amplifier degrades as [84]

$$NF_c = C \cdot NF \tag{3.9}$$

The SOA devices are usually packaged in a *butterfly package* to allow for 2-port fiber coupling. The butterfly package has coupling efficiency of around C=0.65, increasing the packaged SOA NF by an addition 2 dB. On the other hand, RSOAs are packaged in a *TO-can*, with single count fiber-port and much cheaper packaging. The coupling efficiency

52

for this packaging is around C=0.35, which imparts an additional 4.5 dB degradation of RSOA NF.

3.2 Experimental Characterization

At the time of this thesis, very few commercial RSOA devices existed. The RSOA reported in this section was purchased from *Kamelian* [37], and the measurements were performed on the device *RSOA-18-TO-C-FA*. This RSOA is reported to be polarization-independent, operating in the C-band, with maximum optical gain of 25 dB. The device is operational within temperatures of 0-60° C. This device was chosen because of its lower NF value compared to the L-band RSOA we reported in Chapter 2.

The setup consists of a DFB laser source operating in the C-band which provides fixed optical power. A variable optical attenuator (VOA) controls the input power to the device. An isolator is placed to eliminate back-reflections into the laser source. The front facet of the RSOA is controlled by a 3 port circulator. The output of the RSOA is connected to an optical spectrum analyzer (OSA), or an optical power meter. For controlling the RSOA operating conditions, a temperature controlled mount, the *Thorlabs LDM21*, is used that supports both the functionalities of TEC driver and laser diode (LD) driver. The gain, ASE, ASE ripple, and NF of the RSOA device are measured for variations in temperature, operating current and operating wavelength.

3.2.1 Optical Gain

As mentioned before, the gain of the amplifier device is the ratio of output to the input power. At normal operating conditions, i.e. room temperature and operating current I=60 mA the device gain is G=26 dB, with P$_{sat}$= 3 dBm. Figure 3.4 shows the gain for various operating conditions. By changing the device bias current, the amplifier peak gain is effected, this is depicted in Figure 3.4a. By increasing the bias current from I=50-100 mA, the peak gain increases from G=22-26 dB, before saturating at maximum gain. In addition, the saturation power changes with bias current operations. The saturation power variation is P$_{sat}$=-0.5-0.3 dBm, about 0.8 dB for I=50-100 mA.

In another measurement, the operating current is fixed to I=60 mA and bias temperature is varied by T=15-40 °C. By increasing the temperature, the gain of the amplifier device drops significantly. This is due to the increased carrier mobility, which decreases

(a)

(b)

(c)
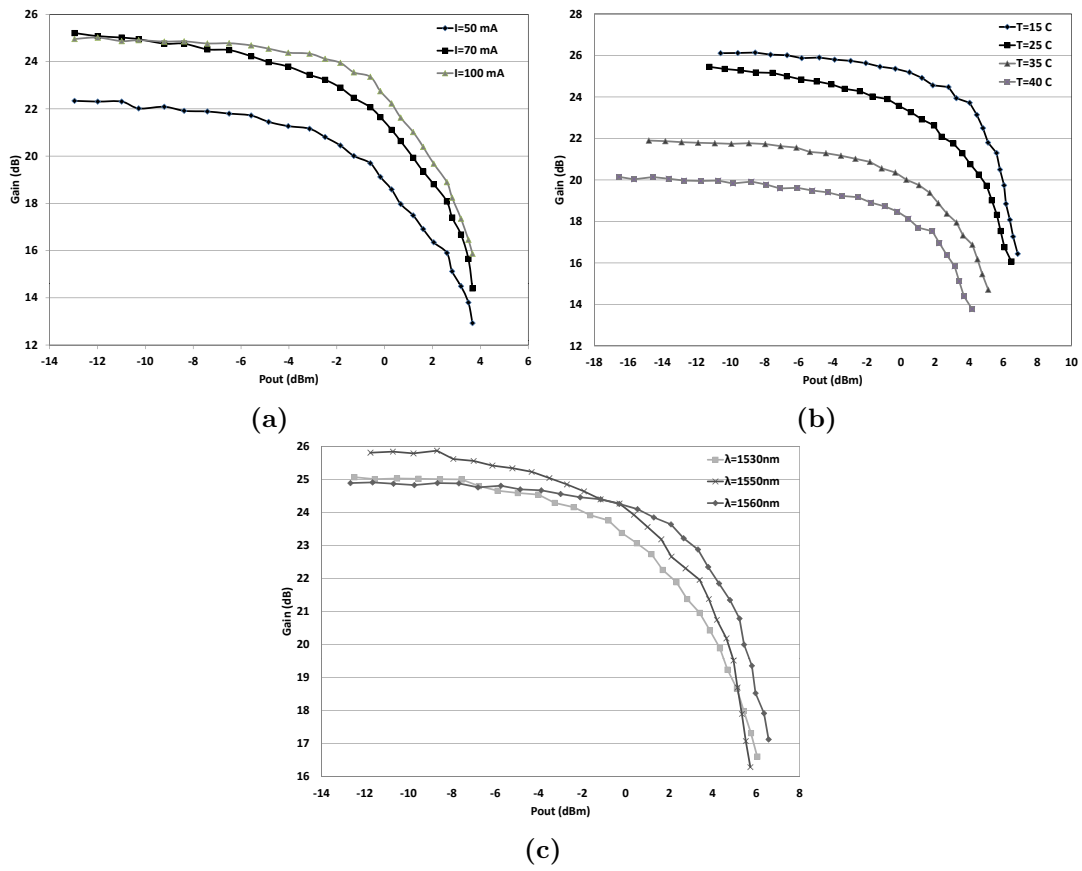
Figure 3.4: Measured Gain (a) Change in biased current (b) Change in temperature (c) Change in operating wavelength

differential gain of the optical amplifier. Figure 3.4b illustrates the gain for various operating temperatures. The peak gain at T=15 °C is measured to be 26 dB, and drops to 20 dB at T=40 °C. Therefore, for ΔT=25 °C, the RSOA peak gain can drop by 6 dB. In addition to the gain drops, the P_{sat} also drops from a peak of 4.5 dBm at T=15 °C to 2.2 dBm at T=40 °C.

By varying the input wavelength to the RSOA, its effect on amplifier gain can be measured. The measured gain for various operating wavelengths is shown in Figure 3.4c. This device was tuned to provide maximum operable gain at 1550 nm wavelength. Therefore operation at 1530 nm and 1560 nm wavelengths decrease the maximum gain by around 1dB to G=25 dB. In addition, the P_{sat} increases with increased operational wavelength. The change is from P_{sat}=1.7-4.3 dBm, about 2.6 dB increase.

In the above measurements, the effect of operating temperature on amplifier gain is the greatest. Operational wavelength greatly effects the saturation output power. Therefore, stable operating conditions of RSOA device at the ONU are necessary for predictable performance.

3.2.2   ASE Spectrum and Ripples

The spontaneous emission spectra of the RSOA for several bias currents as well as the ASE ripples are presented in Figure 3.5. The ASE noise power increases considerably with bias current, which is given by the area underneath the ASE curve. Also, there is a blue shift in peak wavelength by increasing the bias. This is due to the increased band filling effect, which increases the band gap, and subsequently decreases the peak wavelength of the band. By increasing the bias current from 40-100 mA, there is about 30 nm blue shift in the ASE peak wavelength, decreasing from 1550-1520 nm.

Figure 3.5b which is a closeup of ASE spectrum, depicts the gain ripples increase with the bias current. The gain ripple measures 4dB for the highest current of I=100 mA, while it drop to 0.5 dB for lower bias current of I=40 mA. Generally, operating at higher gains will induce greater ripples in the system. These ripples are a critical factor for signal transmission.

In another measurement, the effect of temperature on RSOA ASE spectrum was analyzed. The ASE measurements are shown in Figure 3.6 for bias current of I=60 mA and bias temperatures ranging from T=15-35 °C. An increase in device temperature will cause a shift to longer wavelengths. For increase of ΔT=20 °, about 15nm reduction of peak wavelength is seen from 1545-1530 nm. In addition, the total ASE power is decreased at
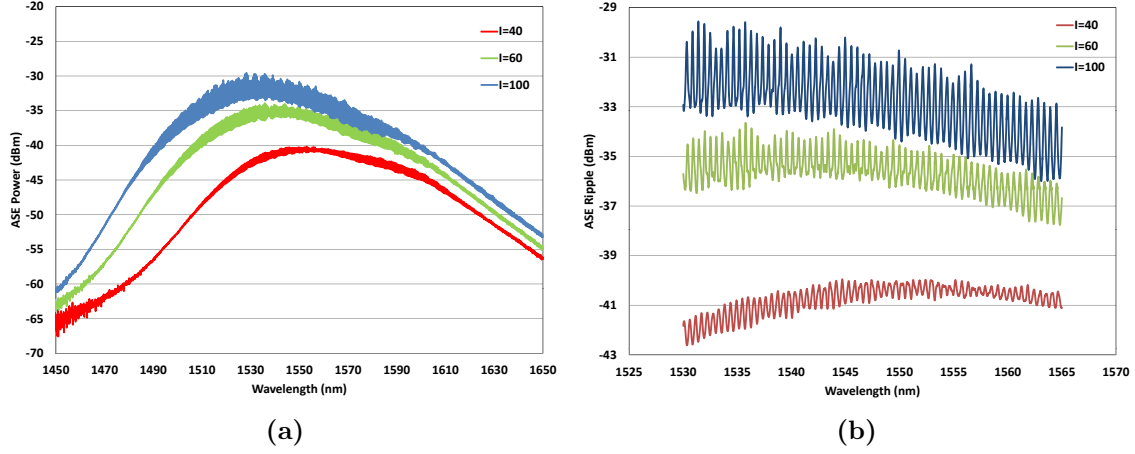
Figure 3.5: The ASE Spectrum of the RSOA with change in bias (a) Blue shift with increase in current (b) Increased ripples with increased current bias

higher temperatures. Higher temperatures induce more carrier spontaneous recombinations, which in turn decrease the number of carriers. This results in smaller bandgap and hence larger wavelength.

The ASE ripples for various operating temperatures are also shown in Figure 3.6b. The ripples are greater at cooler temperatures, where the gain is higher. At room temperature, around 1 dB ASE gain ripple exists in the spectrum, which decreases to 0.5 dB for higher temperature of T=35 °. Although operating at higher temperatures reduces the ripples, a requirement for better modulation, it also decreases device gain, and increases device NF.

The observations above match the theory for gain ripples brought up in Eq. 2.17. The factors that increase gain have an effect of increased ripple. Therefore, a tradeoff must be made between operating conditions, and ripples.

3.2.3 NF Measurements

The NF of the RSOA can be measured through measurement of its ASE power P_{ase}, and gain G by using Eqs. 3.2 and 3.3. In addition, the source spectral density power P_{sse} at the signal wavelength must be measured and subtracted from P_{ase} for correct results. This technique is called the *optical source subtraction method* and is formulated as [73],

$$NF = \frac{P_{ase}}{Gh\nu B_0} + \frac{1}{G} - \frac{P_{sse}}{h\nu B_0} \tag{3.10}$$
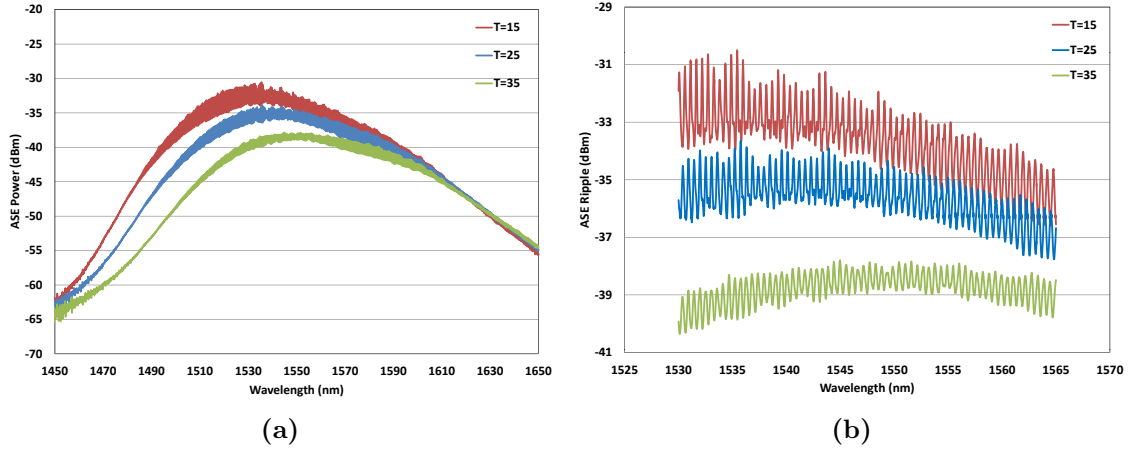
Figure 3.6: The ASE Spectrum of RSOA (a) Red shift with increase in temperature (b) Decrease in ripples with higher temperature

In the measurements, both P_{ase} and P_{sse} are measured for all polarizations. The optical bandwidth B_o is related to the optical bandwidth of the OSA for power measurements. In this case, the optical bandwidth is in the range of 1nm, which is approximately 120 GHz, based on operation in the 1550 nm wavelength region. Moving forward, NF of the device has been calculated for variations in wavelength, current and operating temperature. Due to measurement errors, these measurements have an error bar of $\pm 0.25 dB$ associated with them.

The effect of current bias on NF of the device is depicted in Figure 3.7. In the experiment, the bias current of the amplifier device was varied from 40-100 mA for operating wavelength of λ=1550 nm and room temperature operation of T=25 °c. Depending on the amount of injected carriers into the device, if too low or too high, NF increases. When the injected carriers into the amplifier are low due to smaller bias current, carrier depletion occurs during amplification process. This results in spontaneous emission noise to dominate, and therefore NF to increase. On the other hand, increased bias current will result in higher amplifier gain, which in turn results in higher gain ripple. Therefore SNR decreases, resulting in higher NF for the amplifier device.

In another measurement, the temperature effect on the noise characteristics of the RSOA was studied. In this measurement, the bias current was fixed to 60 mA, the temperature was varied from 20-35 °C, and the NF was measured. The results are shown in Figure 3.8a. As the temperature of the device increases, the device gain decreases, therefore a NF increase of 1.2 dB is seen for 15 °C of temperature change. The temperature change will
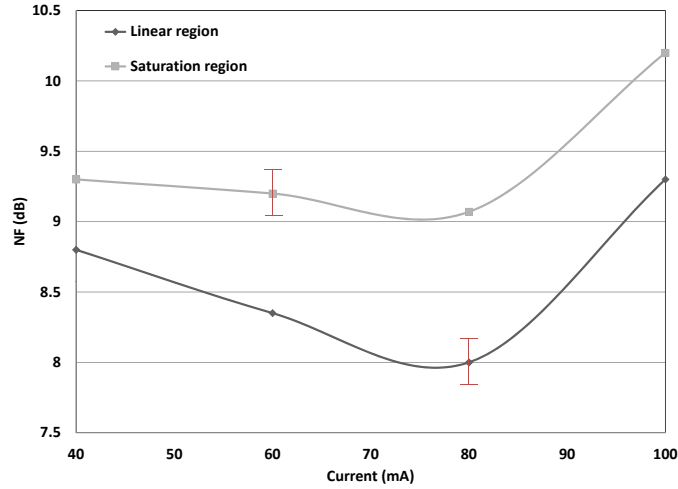
Figure 3.7: Change in NF by varying bias current.

impose increase in amplifier device noise, and therefore the NF of the device.

The operating wavelength effects the amplifier induced noise, and NF of the device, where the relation can be seen in Eq. 3.10. Figure 3.8b shows the measurements of the RSOA NF for change in wavelength of the device, at room temperature and operating current of I=60 mA. At around saturation power, for a wavelength of 1560 nm, the NF of the amplifier is measured to be around NF=8 dB, while this number increases to NF= 10.3 dB when the RSOA is operated at 1530 nm. As a result, for $\Delta\lambda$=30 nm, the NF can deviate by more than 2 dB.

To summarize, the measurements show that NF of the RSOA is high, and it's varying with operating conditions. As such, a possibility exists that greater noise characteristics could impose greater system penalties in a WDM network. In the next section, system performance is analyzed in terms of BER and eye diagrams for the high NF of RSOA device as well as its change over operating conditions.

3.3 Receiver Noise Analysis

To understand the effect of ASE amplifier noise on detected signal, and system performance, a scenario like Figure 3.9 is considered. The output power of the amplifier device is detected by a *PIN* direct detection receiver. The photodetector produces a current that is proportional to the incident optical power from the amplifier, P_o. As such, the photocurrent
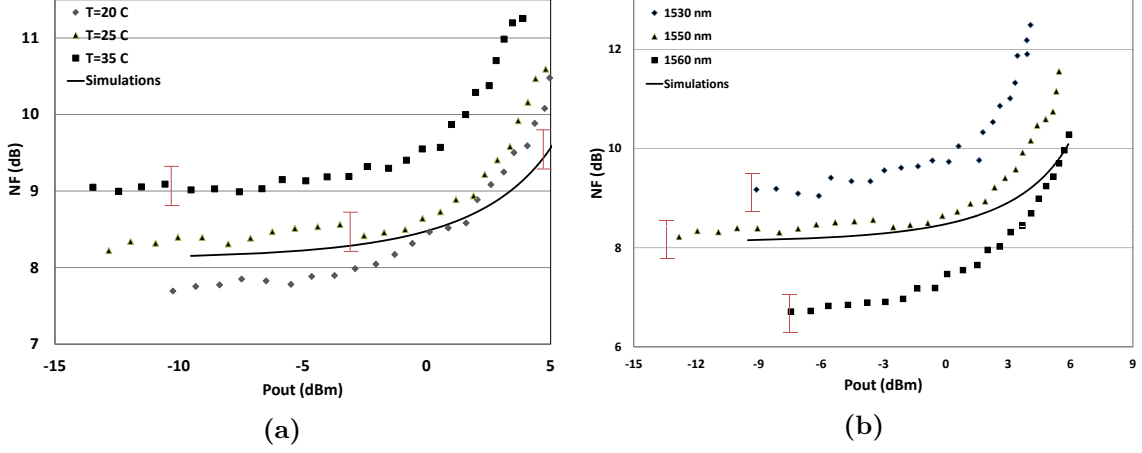
Figure 3.8: Experimental measurements of RSOA NF (a) NF dependence on Temperature for λ =1550 nm (b) NF of RSOA device for change in signal wavelength.

is given by $I_{pd} = RP_o$, where R is the *responsivity* of the photodetector. R is defined as the ratio of generated electrical current to received optical power. It can be represented by $R = q/h\nu$, and depends on the operation wavelength. $q = 1.6 \times 10^{-19}$ c is the electron charge. The photo detector has an electrical bandwidth of B_e.

The pin photodetector contributes to two major noise factors in the process of generating the photocurrent. The first noise factor is *thermal noise*, which is due to the random motion of electrons present at all temperatures. The other noise factor is called *shot noise*, which relates to the random nature of electron distributions generated by photocurrent, even at constant optical power intensities. In other words, the shot noise current is a representation of the variability in the generated photocurrent.

The thermal noise of the photodetector load resistor, R_L results in a random electric current, where the noise power can be characterized by

$$\sigma_{th}^2 = (4kT)/R_L \tag{3.11}$$

In the above equation k is the Boltzmann constant, $k = 1.38 \times 10^{-23}$J/K, and T is the temperature in Kelvin scale. The shot noise power can be written as

$$\sigma_{shot}^2 = 2qI_{pd} \tag{3.12}$$

When the output of an SOA amplifier is detected at the receiver, the output power contains two portions, the signal itself and the ASE signal. The optical detector is a
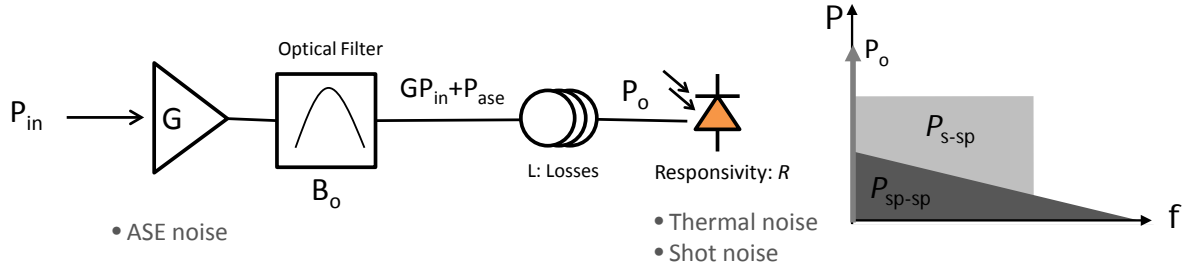
Figure 3.9: Reciever model to evaluate detected signal quality based on major noise sources.

square-law device; The photocurrent is related to the optical power, and the optical power is proportional to the square of electrical field. A square law detector will cause mixing between the different frequency components of the optical signal. This results in a detected electrical spectrum that contains additional mixing components that correspond to the frequency differences between the spectral components of the optical field. Therefore at the detector, beating happens between the signal and spontaneous emission fields. These beating terms are named *signal-spontaneous* beat noise, and *spontaneous-spontaneous* beat noise [84]. The detected power, P_o, and the beating terms are shown in a plot of power vs. frequency in Figure 3.9.

To formulate the existent noises at the detector, a setup similar to Figure 3.9 is considered. In the setup, incoming signal to the amplifier P_{in} is amplified by G gain of the RSOA. Detected signal, P_o is effected by the L loss between the optical amplifier and receiver at OLT. Therefore, the output can be presented by $P_o = P_{in}GL$. The optical bandwidth B_o is determined by the optical filter that is placed after the optical amplifier. At the detector, the presence of thermal and shot noise will add other noise terms to the received signal. The optical beating terms between signal and ASE noise, signal-spontaneous noise and spontaneous-spontaneous noise currents at the receiver are calculated to the values below [84]

$$\sigma^2_{ssp} = 4R^2 P_{ase} P_o \times B_e \tag{3.13}$$

$$\sigma^2_{spsp} = R^2 P^2_{ase} \times (2B_o - B_e) B_e \tag{3.14}$$

In addition, the noise variances due to thermal and shot noise of the detector are represented by

$$\sigma^2_{shot} = 2eR(P_o + P_{ase}) \times B_e \tag{3.15}$$

$$\sigma^2_{thermal} = 2(4kT)/R_L \times B_e \qquad (3.16)$$

To understand the contribution of individual noise terms on the total received noise power, noise terms versus received power have been plotted in Figure 3.10. An RSOA with NF=9 dB is considered for the simulations. In low received powers, the thermal noise of the detector is dominant of all noises. As the received power increases other noise factors contribute as well. Therefore, the contribution of noise is from detector if the received power is low, while noise contribution for higher received powers is mainly from the amplifier itself. For an optical amplifier input of -40 dBm, the total noise contributions comes from both signal spontaneous beating as well as spontaneous spontaneous beating noise, this is shown in Figure 3.10a.

By increasing the input power to -20 dBm, the contribution of spontaneous-spontaneous noise decreases, and the total noise is mainly due to the signal-spontaneous beating noise, this can be seen in Figure 3.10b. From these figures, it can be concluded that RSOA amplifier noise is dominant over detector noise if the received power is not too low. The treatment of noise sources for Avalanche photodetector (APD) receivers for WDM applications is presented in [85], and will not be discussed here.
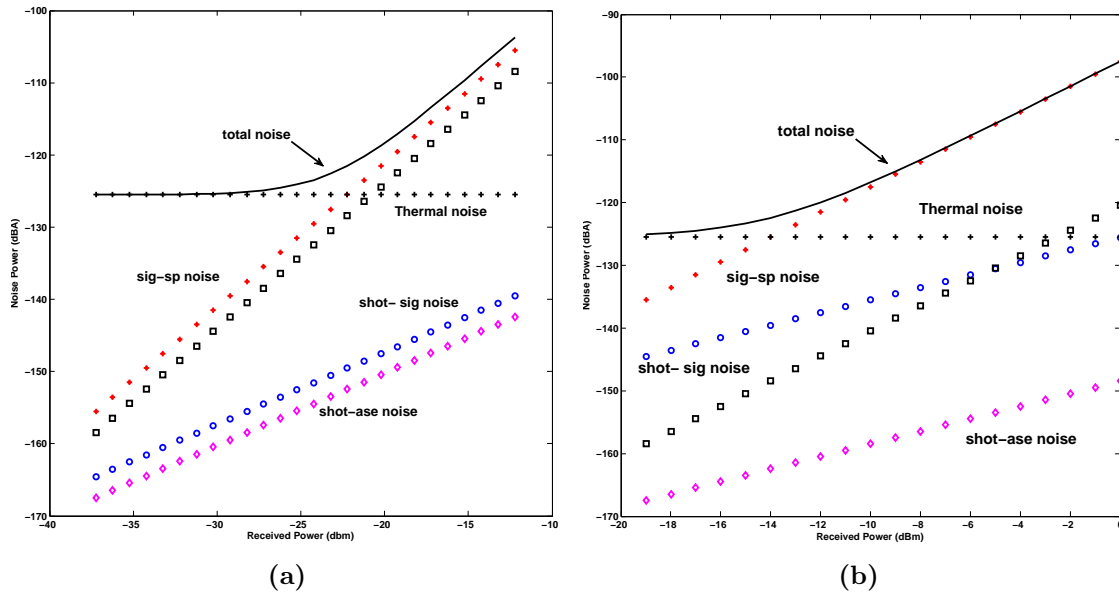
Figure 3.10: Noise Contributions of PiN receiver for optical amplifier NF=9 dB (a) $P_{in}=$ -40 dBm (b) $P_{in}=$ -20 dBm

As mentioned earlier in this chapter, noise figure is defined as the ratio of electrical

signal-to-noise ratios (SNR_i) detected at the input of the amplifier to that of the signal at the output of the amplifier optically (SNR_o). For calculation purposes, the SNRs are referred to the output of an ideal photodetector with 100 percent quantum efficiency. SNR is obtained by detecting the amplifier input directly into a shot-noise limited photodetector. Such definition is critical to the NF measurement. Therefore the input SNR can be shown as

$$SNR_i = \frac{(RP_{in}L)^2}{2eRP_{in}B_e}$$ (3.17)

The signal-to-ratio at the output for spectrally-sliced signals is a result of the signal and ASE power beating terms over the optical bandwidth

$$SNR_o = \frac{(RP_o + RP_{ase})^2}{\sigma_{ssp}^2 + \sigma_{spsp}^2 + \sigma_{shot}^2}$$ (3.18)

From Eqs. 3.17 and 3.18, the NF is calculated as mentioned in Eq. 3.3.

When the optical input power to the RSOA device at ONU is high, the SNR_o of the upstream signal at the receiver depends on the signal-spontaneous noise. However, when the input power level is low, the beat noise of the ASE-ASE also plays a dominant picture. As such, a narrow sliced bandwidth, B_o degrades the SNR_o and impacts the receiver sensitivity. This is known as the spectrum-sliced effect [86]. The effect can be seen in Figure 3.11. For P_{in}=-20 dBm, SNR level is higher than P_{in}=-40 dBm, and does not degrade with lower optical bandwidth. While for P_{in}=-40 dBm, the SNR degrades further for narrower spectral slices.

3.4   Bit Error Rates

In a direct detection receiver, by sampling of the photocurrent, the receiver decides if bit 0 was transmitted in each bit interval or bit 1. Due to noise currents present, the receiver could make a wrong decision resulting in erroneous bit results, therefore the error rate depends on the SNR at the receiver. A simple way to measure the error rate in the detected data stream is to divide the number of errors occurring over a certain time interval by the number of bits (ones and zeros) transmitted during this interval. This is called the *Bit Error Rate*, shown as BER. Acceptable BERs for optical communication systems typically range from 10^{-9}-10^{-12}.

Mathematically, BER can be estimated by calculating the probability of error. A relatively simple and accurate model would be to assume the received 1 and 0 bits as
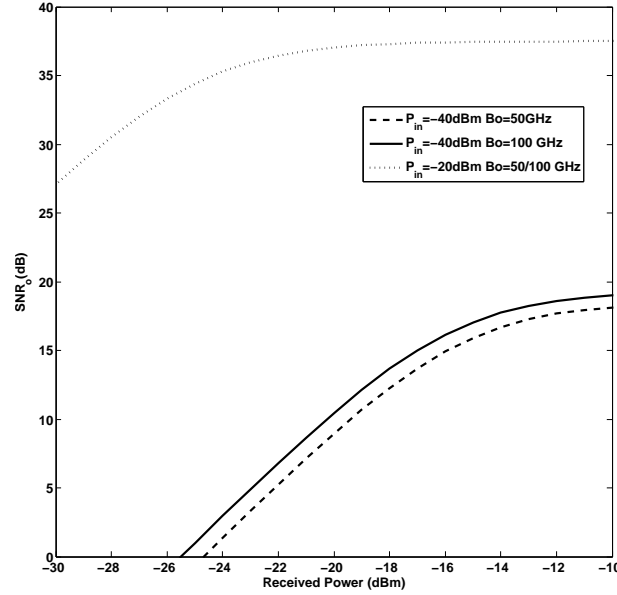
Figure 3.11: Signal-to-noise ratio as a function of received power at the detector for spectrally-sliced signals

Gaussian random variables with mean I, and variance σ. If the probabilities of 0 and 1 bits occurring are equally likely, the probability of error is when a 0 bit is detected as 1, and vice versa. This can be shown as [84]

$$
\begin{aligned}
BER &= \frac{1}{\sqrt{\pi}} \int_{Q/\sqrt{2}}^{\infty} e^{-x^2} dx \\
&= 0.5 \times erfc(\frac{Q}{\sqrt{2}}) \\
&\approx \frac{1}{\sqrt{2\pi}} \frac{e^{-Q^2/2}}{Q}
\end{aligned}
\tag{3.19}
$$

Where Q is defined as

$$
Q = \frac{I_1 - I_0}{\sigma_0 + \sigma_1}
\tag{3.20}
$$

Considering Gaussian statistics, I_1 and I_0 represent the photocurrent sampled by the receiver during a 1 bit and a 0 bit. Also, σ_1 and σ_0 represent the noise variances at each bit sample. For signal level of zero $I_0 = 0$. σ_0 relates to variance with the thermal noise of

63

the amplifier and σ_1 is the total noise variance in the amplifier. In terms of formulations, for ASE injected RSOA that has been directly modulated, the photocurrent, and variances for levels 0 and 1 can be written as

$$
\begin{aligned}
I_0 &= 0 \\
I_1 &= R(P_o + P_{ase}) \\
\sigma_0 &= \sigma_{th} \\
\sigma_1 &= \sigma_{ssp} + \sigma_{spsp} + \sigma_{shot} + \sigma_{th}
\end{aligned}
\tag{3.21}
$$

The Q factor is a wide-used parameter for determining the receiver performance, since it relates to the SNR required to achieve a certain BER. The relation between the two parameters can be seen in 3.12, for example a Q=6 refers to BER requirement of 10^{-9}, and for BER of 10^{-12}, a Q of greater than 7 is required.
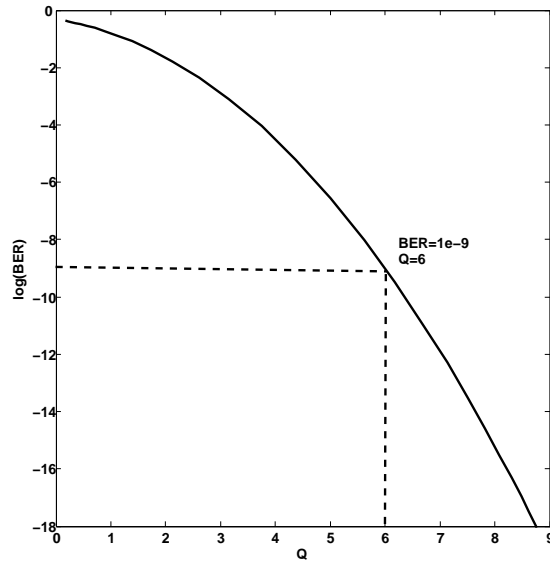
Figure 3.12: Relation between required BER and Q factor of the system

The BER of the spectrally-sliced RSOA has been evaluated for various operating conditions, depicted in Figure 3.13. The input power level to the device has an strong effect on the number of errors detected at the receiver. In Figure 3.13a the BER for different input levels has been compared to the back-to-back measurements where the BER is calculated at the input of the RSOA device. Weaker input power results in stronger ASE noise amplifications, and greater thermal noise impact which in turn leads to worse error rates. If the input power is sufficiently low, as a sample of P_{in}=-50 dBm, the device does

not reach the requirement for acceptable BER of 10^{-9}. At low input levels spontaneous noise levels dominate over signal levels.
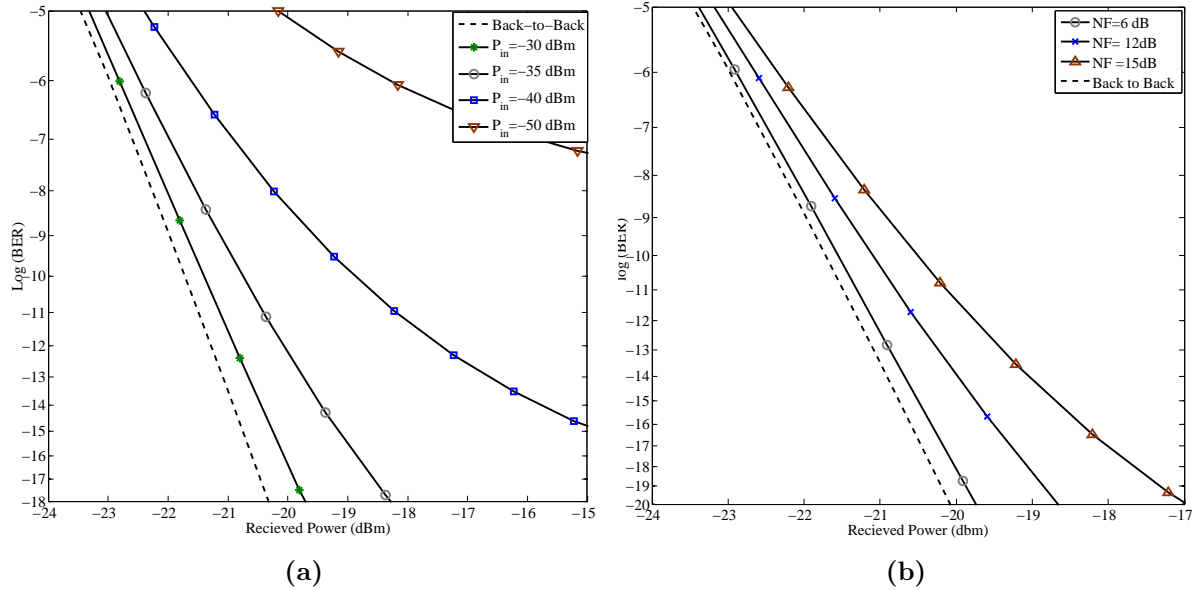
Figure 3.13: RSOA BER as a function of received power (a) With change of amplifier input power P_{in} when device NF= 9 dB (b) With change of amplifier NF when P_{in}=-30 dBm

If the input power is sufficiently high, the NF of the RSOA device change the BER levels, and can induce power penalties in the system. The plot in Figure 3.13b illustrates the BER for NF ranging from 6-15 dB. The input power to the device is fixed to P_{in}=-30 dBm. The power penalty to achieve BER=10^{-9} compared to back-to-back measurements is 1.5 dB, where received power increases from -22 dBm to -20.5 dBm. If the BER requirements become more stringent, for BER=10^{-12}, the power penalty associated increases to 2.5 dB compared to back-to-back measurements. Back-to-back measurements are when the input signal bypasses RSOA, and is directly input into the receiver.

When the RSOA device NF is high, ASE noise level increase, which lead to poor BER. Recall that previous RSOA measurements show how the NF can vary by change in operating conditions like wavelength, temperature, and current. As a result, there exists a minimum of 1.5 dB system power penalty to achieve low error rates of 10^{-9}.

3.5 System Simulations

To confirm the theoretical formulations, system measurements were performed by a simulation model using *VPIphotonics* [87] simulation tool. These measurements account for fiber dispersion effects and other non-linearities which were not considered in the previous analytical model.

The system under test consists of directly modulated RSOA as the transmitter, with 20 km of optical fiber to the receiver, the setup is explained and the model shown in Appendix B. The injected signal into the RSOA can be either from a coherent source, such as a narrow-band laser source, or from a broad-band light source such as a SLED. For coherent injection , optical power from a DFB laser was used while for incoherent injection, ASE power from an EDFA was spectrally sliced using a flat-band AWG and injected into the RSOA. RSOA modulation bandwidth is at 1GHz and it is modulated at a bit-rate of 1.25 Gbps using a pseudo-random bit sequence (PRBS).
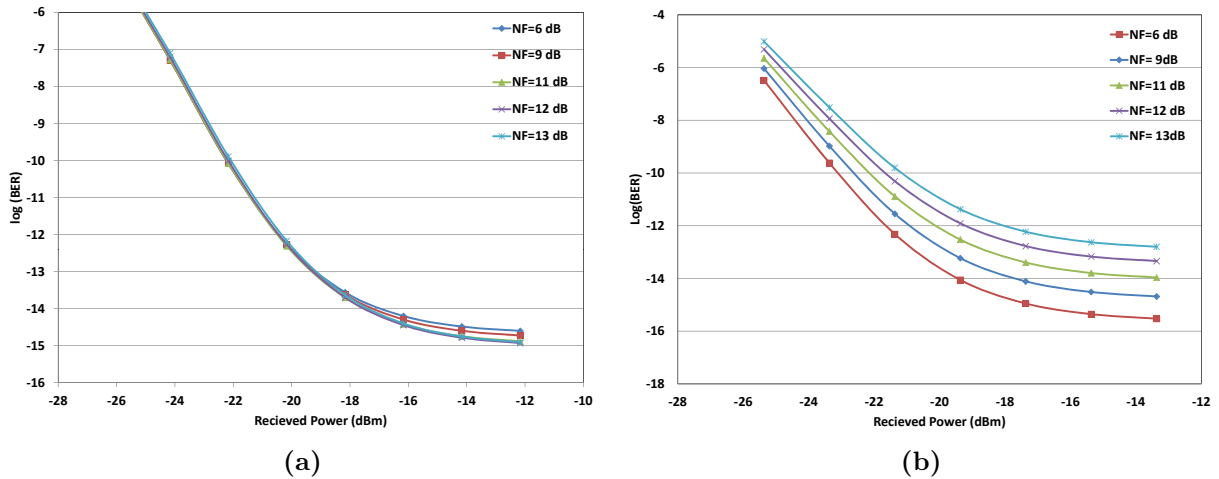
Figure 3.14: BER measurements of upstream data in WDM-PON using directly-modulated RSOA (a)CW seed source (b)Spectrally-sliced seed source

To study the effect of RSOA NF on system performance, the NF parameter of the RSOA was varied by changing the n_{sp} parameter, and BER measurements were then taken for different received powers. The results of coherently-injected WDM-PON systems are shown in Figure 3.14a, where the BER measurements show that with an increase in the device NF, there is minimal power penalty induced upon the system. From the simulations, it can be deduced that when RSOA-based WDM-PON systems use CW coherent injection

source, the signal level dominates over ASE noise and its effect on the system. As such, with coherent injection, the RSOA NF does not affect system performance.

On the other hand, when RSOA is injected with an incoherent spectral-sliced signal, the effect of RSOA NF on performance is somewhat different. Figure 3.14b shows the BER for different received powers when RSOA has different NF parameters. When NF parameter is changed from 6-13 dB, the power penalty required for achieving BER of 10^{-9} is 2dB from the lowest NF=6 dB to highest NF=13 dB. When requirement for BER=10^{-12} is detected, the power penalties increase to 4 dB.

For incoherent-injected WDM-PONs a lower BER floor of 10^{-12} is observed for RSOAs which have large NF. The BER floor gets worse for longer PRBS streams. This is due to the deterministic jitter induced by the ASE signal. Therefore, it is of utmost importance for RSOA designs to possess lower NF, as well as the packaging. If not, the high ASE noise levels deteriorate the upstream signal, and even with advanced equalization techniques, the original data might not be retrieved.

For low cost incoherently injected systems, various methods could be considered to decrease RSOA NF. One method is by use of varying current density along the length of the RSOA to push the saturation region away from the input facet. In the proposed method, by increasing the density of dielectric contact vias at the input facet of RSOA, more carriers exist at the input of the device where the signal is weakest, therefore the signal becomes amplified early on. Such a method has been demonstrated previously for reduced NF in SOAs [64], and will improve the NF of device by around 1dB.

3.6   Summary

The RSOA device possess large NF, due to amplification of the spontaneous emission noise. We have shown through analytical analysis that compared to SOAs, RSOAs have larger chip NF. Device coupling due to packagings further increases the NF of an RSOA by another 4dB. The operating conditions such as bias current, temperature, and operating wavelength also influence the device NF. Through experimental characterization on a commercial RSOA device, we have shown that the NF can increase by another 3 dB when operated at higher temperatures or lower wavelengths or low bias conditions.

The device bias conditions effect the gain of the amplifier as well. We have depicted this through experimental analysis, and have shown that increased bias current and reduced operating temperatures, increase the gain. When the gain of the device is higher, the

ripples in that device increase. It is important to balance the operating gain in order to reduce ripples, where reduced ripples help with direct modulation of the device.

The effect of increased RSOA NF on system has been investigated through theoretical modeling. By considering Gaussian statistics for the received signal, the BER can be calculated from Q-factor. Through incoherent injection, the ASE power of RSOA is a portion of transmitted signal. Therefore the effect of RSOA n_{sp} factor on system BER is significant. We have shown that by change of RSOA NF=6-15 dB, to achieved BER=10^{-12}, a power penalty of 2.5 dB will be imposed on the system, with less stringent requirements, BER=10^{-9} the power penalty is still 1.5dB.

In system level analysis, where the RSOA was placed at the ONU of a WDM-PON, through 20km of optical fiber the upstream data was analyzed. When the seed light is from a CW source like DFB laser, the modulated amplified output of RSOA is far greater in power than the ASE noise. Therefore, the effect of RSOA NF on coherently-injected system is negligible, and great system performance is achieved. In summary, coherently-injected RSOAs using single-wavelength laser sources do not create power penalties for system level applications due to reduced ASE noise effects.

On the other hand, when the seed-signal comes from an EDFA source, the amplified modulated upstream data by RSOA contains ASE noise, and the effect of RSOA NF plays a big part in system performance. Although the BER floor is still achievable, but change of NF=6-13 dB, imposes 4dB power penalty on the system.

For this reason, various measures can be taken to reduce the effect of NF. The first thing is to make sure there is enough input power into the RSOA device. As shown earlier in this chapter, higher input power levels reduce the effect of ASE-ASE beating noise terms. Another method is to design an RSOA with lowest possible NF. For this, the carrier distribution into the RSOA can be modified.

Chapter 4

Effect of AWG Filtering on Spectrally-Sliced WDM-PONs Deploying RSOAs

In this chapter, the performance of a WDM-PON system deploying incoherent-injected RSOAs, and consisting of AWG filters at the remote node and at the OLT will be investigated. The AWG filter in reality can possess two spectral shapes, namely the Gaussian and the Flat-band shape. When upstream data signal travels through multiple AWGs, part of the signal is filtered, and the received signal is degraded. As good performance measures, the eye diagrams and the BER of the received signal at every stage of the system are analyzed, and the power penalties associated with filtering effects are calculated. The degradation of signal by the filtering effect is proven through system simulations, theoretical formulations, and experiments. It is proven that Flat-band AWGs are essential in achieving low probability error in WDM-PON systems. Further, the effect of frequency detuning between AWG devices at the OLT and RN are investigated, where the detuning between AWG center wavelength can impose additional power penalties to the system.

4.1   AWG Filtering Effect

Reflective architectures using spectrum sliced incoherent broadband seeding light source are a promising technology for WDM-PON. The AWG takes care of spectrally splicing the ASE output spectrum of a broadband light source, so that each ONU is given a portion of

the signal. Because there are no power lines in the field, a-thermal AWGs are preferred. Athermal AWGs avoid temperature variations which otherwise cause the AWG to shift alignment. Temperature insensitive AWGs are very reliable, and provide exact wavelength matching with the optical source despite variations in environmental conditions, with at most 20pm of wavelength detuning for variations in temperature of -40 to +80° C [88].

Figure 4.1 shows the schematic diagram of a typical WDM-PON system architecture. Two AWGs are involved in the upstream signal transmission. For the upstream signal, the first AWG lies in the field, and multiplexes the incoming signal into a single fiber for transmission to the central office. Further, this AWG spectrally slices the broadband seed light for each ONU. The second AWG which lies in the central office de-multiplexes upstream traffic from each ONU, before being received by the detector.

AWG filters do not possess an ideal filter shape, and commercial AWGs usually have a Gaussian band shape or mimic the Flat-band filter shape. AWGs with Gaussian-type spectral shape have a narrow 3-dB bandwidth compared to the channel spacing. Flat-band AWGs, on the other hand, mimic an ideal filter, and possess larger 3-dB bandwidth.
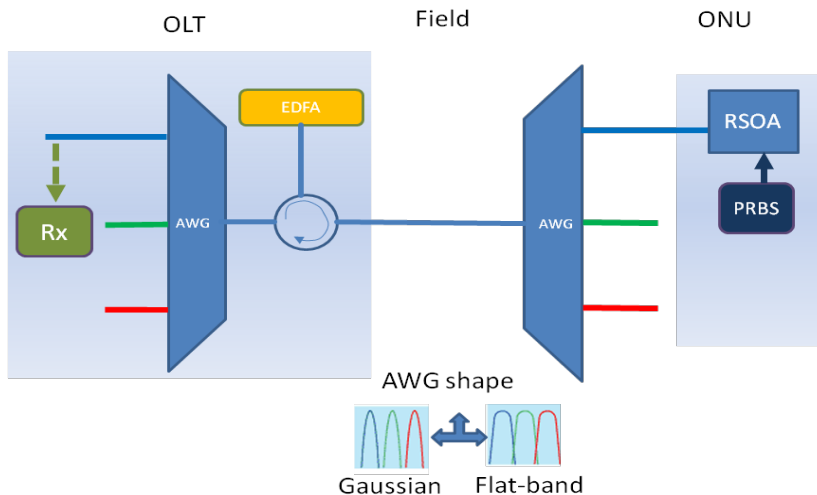
Figure 4.1: Incoherent-injected WDM-PON deploying two AWG filters (Gaussian-shape or Flat-band)

The spectral response of AWGs will have a bearing on the incoherently injected WDM-PON systems. While WDM-PON systems have been considered before, to our knowledge the effect of the AWG filter shape on the performance of devices have not been considered before. To describe such effect, consider the input to the RSOA to be spectrally sliced from

a broad-band source (e.g. EDFA) by the field AWG. The input signal has the same spectral shape as that of an AWG assuming that the broadband source is nearly flat over the AWG bandwidth. The signal is amplified and modulated by the RSOA, thereby broadenings its frequency component slightly. If all the modulation terms are to be conserved, such a signal must then pass through a filter with a wider pass-band than itself.

In a WDM-PON, the upstream signal passes through the field AWG, with the same pass-band as itself. At the OLT, the signal passes through a similar AWG at the receiver. Therefore, parts of the data would be lost due to filtering effect of AWG, not once but twice, and the eye diagram would close up substantially. In earlier WDM-PON system measurements using incoherent injection of the RSOA, such problems have been avoided by deploying a wide-band filter at the receiver end [89, 46]. However in WDM-PON implementations, the AWG device in the field is replicated at the receiver, and therefore such problem cannot be avoided.

4.2   Theoretical Analysis

For more detailed analysis of the filtering effect that happens in a WDM-PON deploying AWGs, it is essential to discuss the mathematical formulation. In low-pass filter formulation, we assume that the AWG possesses a Gaussian transfer function centered around zero frequency in terms of E-field as follows [90]:

$$H(f) = exp\left(-\frac{f^2}{2f_c^2}\right) \tag{4.1}$$

Where f_c is the cut-off frequency related to the 3-dB bandwidth, B_{3db}, as follows,

$$f_c = \frac{B_{3dB}}{2\sqrt{ln2}} \tag{4.2}$$

The input power to the RSOA, P_{in}, has the same spectral band-shape as the AWG filter used for spectrally-slicing it, with E-field transfer function of form H_{awg1},

$$P_{in}(f) = aH_{awg1}^2(f) \tag{4.3}$$

Where a is the factor representing the power level of the RSOA input.

The input power to the RSOA is amplified with Gain G, so the spectral power shape of the RSOA output (P_{rsoa}) has the form of $P_{rsoa} = GP_{in}(f)$. This signal is multiplexed

by the field AWG for upstream transmission, and the output power spectrum after the field AWG filter (P_{awg1}) is of the form $P_{awg1} = P_{rsoa}H_{awg1}^2(f)$. As a result, the modulated RSOA output is filtered by the field AWG transfer function, resulting in loss of modulated signal.

Assuming link losses to be negligible, the upstream signal is de-multiplexed by the AWG located at the OLT with transfer function of H_{awg2}, before being detected by receivers. The spectral shape of the received power (P_{rec}) at the central office has the form of $P_{rec} = P_{awg1}H_{awg2}^2(f)$.

For a modulated signal, this effect will filter the tails of the modulated signal resulting in loss of information and deteriorating the output signal. It is obvious that at the OLT further filtering of this signal before the receiver would worsen the BER of the upstream signal, with output power levels as

$$P_{rec} = P_{rsoa} \cdot H_{awg1}^2(f) \cdot H_{awg2}^2(f) \tag{4.4}$$

Based on the above analysis, the filtering effect for an un-modulated signal is shown in Figure 4.2 for a system deploying Gaussian-type AWGs. P_{rsoa}, P_{awg1} and P_{rec} are plotted based on above equations. The total received power is the sum of power over all frequencies, calculated to be -8.3 dBm, -7.5 dBm, and -6 dBm respectively. In these calculations, the Gaussian AWG has a bandwidth of 50 GHz, and the channel spacing is considered to be 100 GHz. From the figure, it can concluded that in addition to decrease in optical power, spectral components are lost resulting in pattern dependent effects and degradation of the eye diagrams.

4.3   System Simulations

In order to quantize the pattern dependent filtering effect of AWGs, incoherently-injected WDM-PON system is analyzed using VPI Photonics. The system setup is depicted in Figure C.1, and described in Appendix C. The parameters of the RSOA are adjusted to match the performance of the RSOA demonstrated in Chapter 2.

In this simulation, the broadband light source is achieved by using an EDFA which is modeled by an erbium-doped fiber, injected with a high-power CW laser source. The source output is then spectrally-sliced using an AWG. The input to the RSOA is -20 dBm, which is amplified and modulated, the output is varied to measure power penalty effects. The optical gain within the RSOA chip is 28 dB. The optical fiber length is 20 km, and the fiber loss is 0.2 dB/km.

72
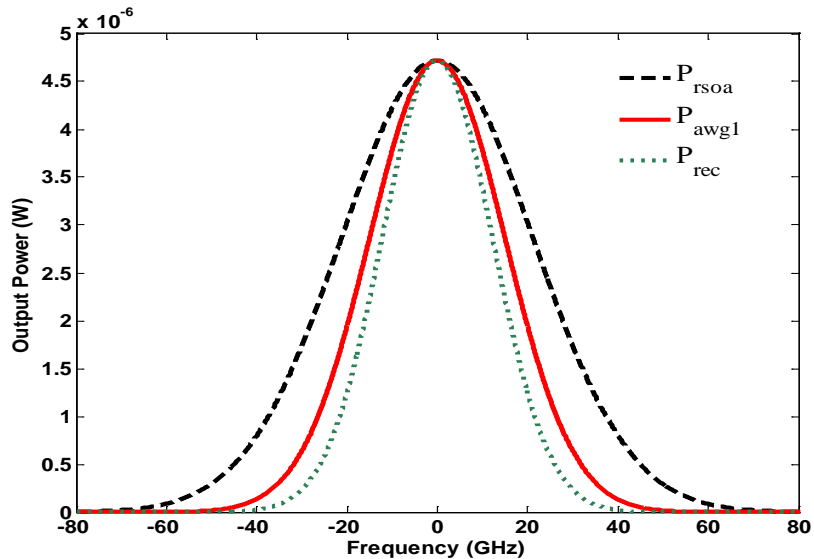
Figure 4.2: Spectral power change of the upstream data after each AWG

The RSOA is directly modulated by a 1.25 Gb/s PRBS data stream and sent through the optical fiber to the OLT. The AWGs consist of 100 GHz channel spacing, with a Gaussian filter 3-dB bandwidth of 50 GHz, and flat-band AWG 3-dB bandwidth of 75 GHz. The parameters for the AWG are derived from commercially available devices from *NTT Electronics*. Considering no insertion loss, and no chromatic dispersion for the AWG devices, the band shape of these devices are shown in Figure 4.3.

To calculate the effect of signal loss on this system, the output and BER of the signal is measured after passing through each AWG. The eye diagram of the data signal after each filter is shown in Figure 4.4 at an average received power of 8 dBm. The top row corresponds to eye diagrams for Gaussian AWG, and the bottom row depicts the eyes when Flat AWGs are used. At the receiver end, complete closing of eye is observed after the Gaussian AWG, while a Flat AWG maintains the eye opening.

Figure 4.5 shows the BER of the upstream data at the receiver end using two different types of AWGs. By deploying an athermal Gaussian AWG in Figure 4.5a, it is evident that for BER of 10^{-9}, a power penalty of more than 3 dB exists after the field AWG and the BER curve does not even reach the BER of 10^{-9} at the receiver merely due to the filtering effect of an AWG. A floor in the BER curve is observed at the receiver at a value of around 10^{-8}, and therefore performance requirements are not achieved. From these results, it is suggested to avoid use of Gaussian type AWGs in WDM-PON systems.

73
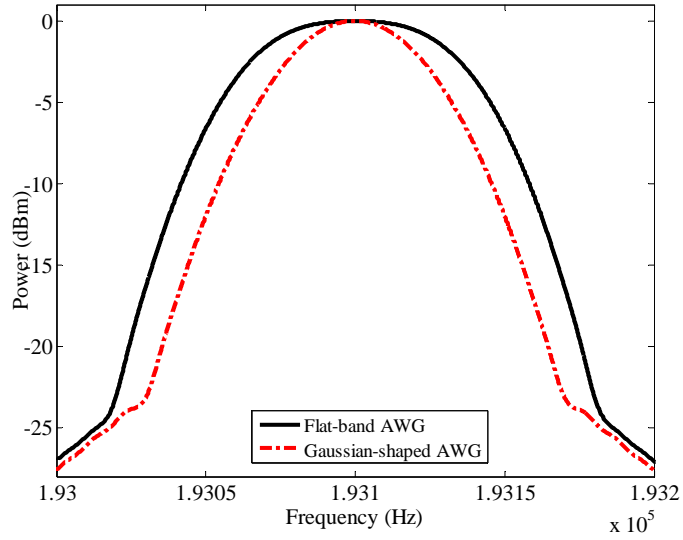
Figure 4.3: AWG band-shapes for 100 GHz channel spacing using VPI Photonics
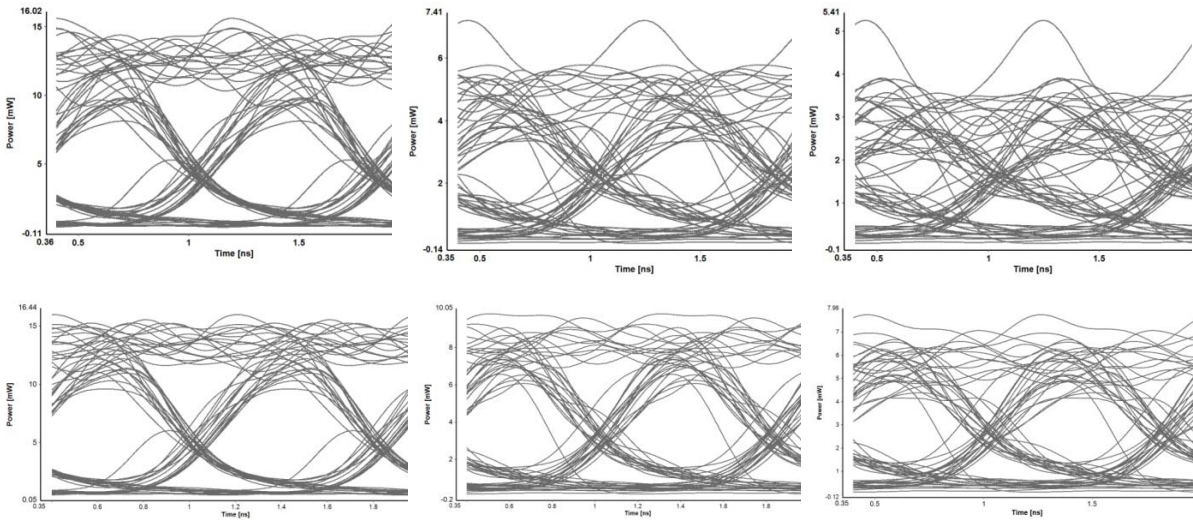
Figure 4.4: Eye diagrams after each AWG using (a) Gaussian-type AWGs, where closing of the eye is observed (b) Flat-band AWGs which maintains eye opening

74

Figure 4.5b shows the signal BER for various output powers for a Flat-band AWG. Using such AWG, the response is approaching that of an ideal filter. Thus, the filtering effects of the signal should be reduced. From this figure, it is evident that a maximum power penalty of 2.5 dB exists for a BER of 10^{-9} at the receiver. Also, the floor on the BER curve has been reduced to below 10^{-10}. As a result, Flat-band AWGs are a must, for WDM-PON multiplexer deployment. Even though there exist power penalties due to the filtering effects of AWGs, but minimum system requirements are met.

(a)   (b)
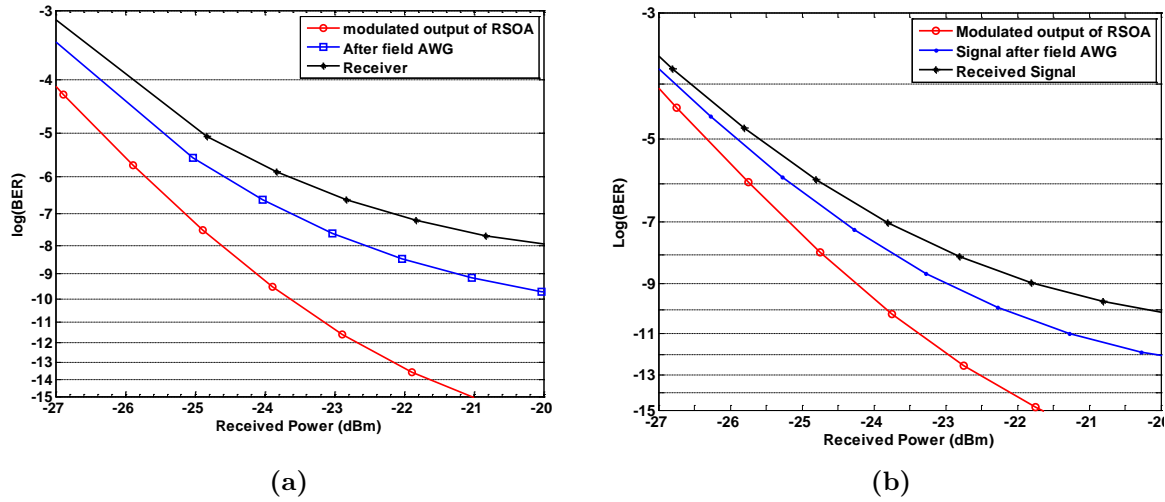
Figure 4.5: Power penalty induced in an incoherently-injected WDM system using (a) Gaussian-type (b) Flat-band AWGs

4.4 Experimental Measurements

The performance of a Gaussian AWG is measured experimentally using a setup shown in Figure 4.6. ASE from an EDFA is spectrally sliced using a 50 GHz bandwidth Gaussian AWG with a 100 GHz channel spacing and injected into a RSOA. The injected power is -15 dBm. RSOA has a fiber coupled optical small signal gain of 20 dB and an output saturation power of 3 dBm. The device is modulated at 1.25 Gbps using a pseudo random pattern of $2^3 1$-1 length. Figure 4.7 shows the measured eye-diagrams for the different stages. Eye diagrams are measured immediately (a) after signal amplification from the RSOA, (b) after the first AWG and (c) after the second AWG at an average output power

of -15 dBm. Significant closing of the eye is observed because of the filtering of the signal as was expected from the previous simulation results.
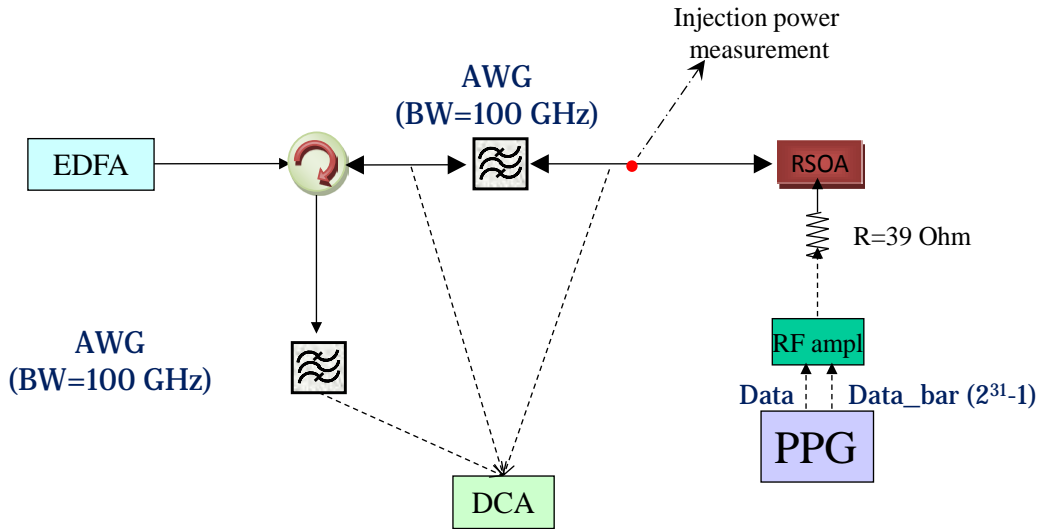
Figure 4.6: Experimental setup for measuring the effect of the AWG

4.5 AWG Detuning

The filtering effect that occurs in a WDM-PON system greatly limits the performance of spectrally-sliced WDM-PONs, and induces power penalties which reduce the BER performance of the device. In addition, if the center frequencies of the two AWG devices are not exactly matched, further loss of data would occur, which results in greater power penalties. In this section, the effect of frequency offset is investigated.

Using VPI Photonics for system modeling, the RSOA is modulated using the spectrally-sliced output from an EDFA, and modulated directly by PRBS type data. The bit rate for this system is 1.25Gbps. The system, including the RSOA, the optical fiber, and the two AWGs are set to possess a center frequency of 193.1 THz. By changing the center frequency of the AWG located at OLT, BER performance of the receiver is measured. Note that this experiment was done using Flat-band AWGs, because the use of Gaussian AWGs would cause the BER floor to be in the order of 10^{-8}.
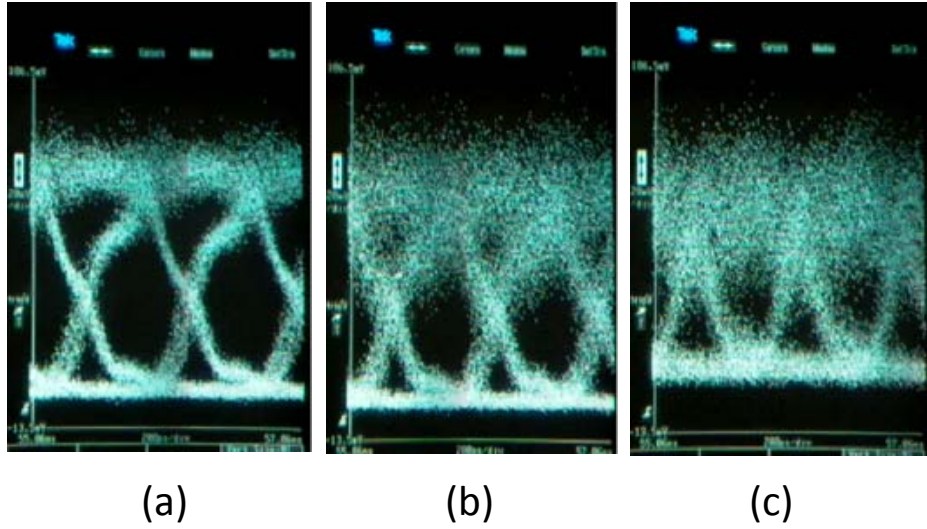
Figure 4.7: Measured eye-diagrams at 1.25 Gbps (a) after signal amplification from the RSOA (b) after the first AWG (c) after the second AWG at an average output power of -15 dBm
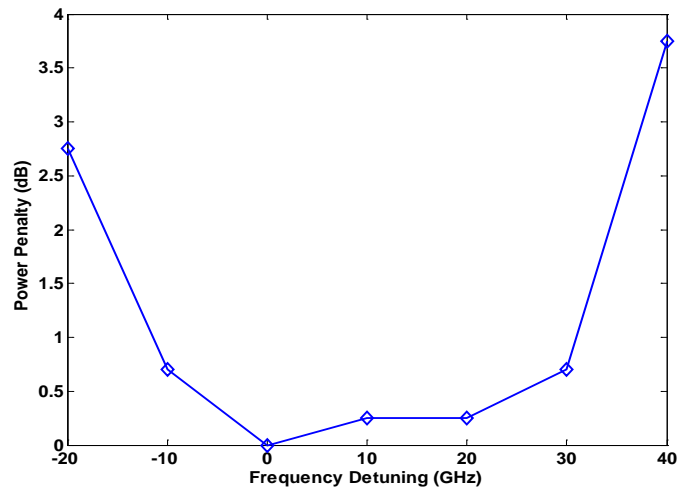
Figure 4.8: Power penalty induced by detuning the field AWG from the OLT AWG for Flat-band AWGs

The RSOA input power is fixed to be -23 dBm, and the receiver power is changed using a variable optical attenuator (VOA). The AWG is then detuned from the center wavelength by steps of 10 GHz, equivalent to 0.08 nm. The power penalty induced to keep the BER fixed at 10^{-9} was calculated, and the results are shown in Figure 4.8.

For a 10 GHz shift in the AWG grid, less than 0.3 dB power penalty is achieved. The detuning is asymmetric from the center point. For 0.5 dB of power penalty, at most +30 GHz detuning between the two AWGs could occur, while only -10 GHz detuning of this AWG from the field AWG could happen. This asymmetry comes from the presence of a Fabry-Perot mode in the RSOA spectrum creating a gain ripple (the gain ripple in the simulation was 1 dB) and how the peak of the mode aligns with the seeded wavelength. If the RSOA is considered to be ideal with no FP mode, the effect of detuning is symmetrical around the center wavelength. Since RSOAs have gain ripple of the order of 1-2 dB, and there is no way to exactly align the FP mode with the seeded signal in a system, system designers should expect a 0.5 dB power penalty for a 10 GHz relative shift in frequencies for the AWG.

4.6   Summary

For incoherently-injected WDM-PON systems, spectrally-sliced seed source has a bandwidth equal to the bandwidth of the field AWG, ranging from 50-100 GHz, and therefore the upstream traffic has the same bandwidth as the two AWG filters. We have illustrated the filtering effect that would cut off the tails of the upstream signal and deteriorate the received signal. As a result, Gaussian type AWGs should not be deployed in these systems due to pattern dependent effects, and the floor BER of 10^{-9} is not achievable. For such systems, it is important to use flat-band a-thermal AWGs.

For a flat-band AWG, significant power penalty of 2.5 dB exists due to the filtering effects of the AWG, and the required BER performance can be achieved. In addition, the detuning that could occur between the center wavelength of the two filter devices would impose an additional power penalty on the system. We have shown through simulations that by deploying athermal flat-band AWGs, the OLT AWG could at most be detuned from the field AWG by 10GHz, and that would create an additional power penalty of 0.5 dB.

As concluding thoughts on RSOA device for WDM-PON applications, RSOA does not seem to be an ideal device due to the increased noise discussed in Chapter 3, issues with AWG filtering discussed in this chapter and its cost. As such, in the next section a novel device is proposed for deployment at ONU.

Chapter 5

Injection-locked Fabry-Perot Laser

Fabry-perot laser diode (FP-LD) sources provide a simple and compact solution at the ONUs in a WDM-PON network, along with low power consumption. In addition, the low cost and ease of production make FP-LDs very attractive for WDM-PON applications. However, multimode operation limits their applications. This can cause low bandwidth, power budget in the optical link, and high intensity noise. Optical injection is an effective method for tackling the issues, and with injection of a master light source at a specific wavelength, the FP-LD can be locked to one cavity mode. This helps improve the modulation bandwidth, and reduce the mode partition noise and chirp. As a result high bit-rates can be achieved with minimal device and management cost. In this chapter the injection-locked FP-LD is evaluated in detail. The issue with mode drift due to temperature and current changes are addressed. A monolithically integrated device is presented which consists of FP-LD with integrated phase modulator. It can be used to counter any drift in wavelength due to temperature changes and allow for cooler-less operation.

5.1   Fabry-Perot Laser Diode

A FP-LD is the simplest type of edge-emitting semiconductor lasers, consisting of an optical cavity as the gain medium, surrounded by p-type and n-type doped regions. The facets of the optical device are cleaved to provide reflections for the generated photons, and build up intensity. The current supplied to the p-i-n junctions results in recombination of carriers (electrons, holes), at first through spontaneous emission to generate the seed photons and later through stimulated emission to provide lasing. The wavelength of radiation, λ is dependent on the cavity length L, because only multiples of half-wavelength can exist in

the optical cavity [91]. These are called the *longitudinal modes* of the laser diode and can be obtained by [67]

$$\frac{m\lambda}{2n} = L \tag{5.1}$$

In the above equation, m is an integer, and n is the effective refractive index of the semiconductor.

From Eq. 5.1, the resonating cavity can support an infinite number of modes, but the semiconductor material provides gain only within a finite range of wavelengths. That is determined by the gain curve which varies according to the structure and material of the laser, and whether it's bulk material or quantum well.

In order to avoid loss of output power, it is common to apply highly reflective coating on the rear facet of the device with $R_2 = 90\%$ and keep the front facet anti-reflective with $R_1 = 10\%$ or lower to keep the cavity in resonance mode [92]. Therefore the output power is mainly emitted from the front facet of laser.

The wavelength spacing between 2 modes in a FP cavity, m and $m + 1$, is called *free spectral range* (FSR) or $\Delta\lambda$, and can be achieved from Eq. 5.1, taking into account dispersion effect ($dn/d\lambda \neq 0$)

$$\Delta\lambda = \frac{\lambda^2}{2n_g L} \tag{5.2}$$

Where $n_g = n - \lambda\frac{dn}{d\lambda}$ is the group refractive index. Following the inverse relationship of frequency f, and $\lambda = c/f$, the relationship between frequency and wavelength spacings is derived as

$$\Delta f = -\frac{c}{\lambda^2} \cdot \Delta\lambda \tag{5.3}$$

In addition, the frequency spacing between 2 adjacent modes Δf can be calculated as

$$\Delta f = \frac{c}{2n_g L} \tag{5.4}$$

As an example, the relationship between longitudinal mode spacing, and the corresponding frequency spacing desired for WDM-PON systems are tabulated in Table 5.1. The multiplexing device, AWG will be operable at one of the tabulated FSRs.

5.2   Injection-Locked Laser

By itself, a FP laser diode is less favorable for PON applications due to the multi-mode nature of the structure. Therefore, it is of interest to promote single mode lasing out of

Frequency Spacing (GHz)	Longitudinal Mode Spacing (nm)
50	0.4
100	0.8
200	1.6

Table 5.1: ITU-standard FP mode spacing and its corresponding frequency spacing in GHz for WDM-PON applications

the simple structure. There are various methods to achieve this; namely use of Distributed Bragg gratings (DBR) laser and DFB lasers. However, these mirror methods increase the laser cost, and can only be designed for a certain wavelength operation. Aside from cost perspective, use of single wavelength source at the customer interface imposes individual wavelength management. Injection-locked lasers provide single wavelength operation, where the operation wavelength can be determined by the seed wavelength source.

Injection-locking of a FP laser can occur by use of a second laser source. The optical power from the seed laser source with a defined wavelength is injected into the FP laser, forcing the cavity to resonate within that specified mode. As such, within a close range, one of the modes of the FP laser with a similar frequency is locked to input wavelength, resulting in that mode becoming amplified in power, and the other modes of the laser diode suppressed in power [93]. The wavelength mismatch between the master and the free-running follower laser is called wavelength detuning. In general, the higher the injection power, the larger the allowed detuning for stable locking.

In detail, through photon injection into the FP cavity, stimulated emission will become strong enough to emit light in the incoming wavelength, and to reduce the carrier density below threshold. Therefore, the injected photons become resonantly amplified, and all other modes will be suppressed due to carrier depletion. However, mode locking can only happen within a specified range, called the locking range. The width of the locking range depends on the ratio of injected power relative to the power of unlocked laser, and also on the coupling efficiency between the two optical sources [4].

Figure 5.1 shows the simulated lasing spectrum when the input wavelength is aligned to a FP cavity mode and when it is misaligned from a FP mode by 8 GHz. For these simulations, the VPI simulation tool is used [87], and the laser is directly modulated at 2.5 Gbps using Non return to Zero (NRZ) modulation of a PRBS sequence. A CW laser source with 1 mW power is controlled by a VOA before being input to the FP laser. By changing the wavelength of the CW source, the effect of seed detuning on mode-locking is investigated. The simulation schematic is depicted in AppendixD by Figure D.1, and the

parameters for modeling of FP laser source are tabulated in Table D.1.

From the simulations, it is clearly seen that the injection efficiency of the laser is degraded due to detuning and the side mode suppression ratio (SMSR) suffers. The maximum SMSR is around 45 dB for fine tuning, whereas it reduces to 22 dB by detuning of around 8 GHz. With our simulations, the frequency locking range of a coherent light source is in the range of about -8 GHZ up to 12 GHz, which corresponds to 0.16nm, which is less than half of the FP mode spacing. Therefore, the injected input wavelength can tolerate a small variation gap, before locking is lost.
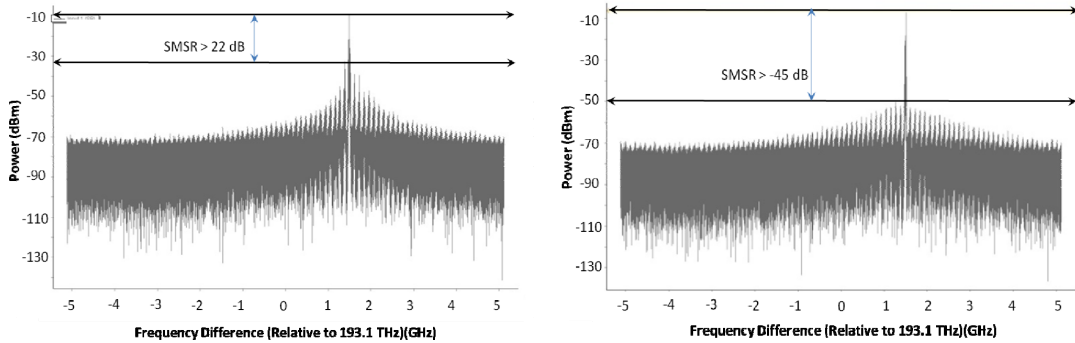
Figure 5.1: The effect of frequency misalignment on injection-locked FP laser SMSR

The asymmetry of the locking range can be seen in Figure 5.2. This asymmetry is due to the asymmetric nature of the gain curve vs. wavelength, and its dependence on carrier density. As the carrier density increases, the peak gain increases as well. The carrier density and the refractive index of a material are coupled, and therefore the detuning range is not equal on both sides [93].

A coherent light source like a DFB laser, used as the injected light source, could provide higher data rates of up of 10Gb/s [94]. However, aside from economic issues, the injection locking range would be very narrow, and around 3.6 GHz of a FP mode. In addition, the FP modes drift with temperature and current density, therefore the device needs to be stabilized and cannot operate cooler-less which is desirable for low cost and low power operation.

As an alternative, an incoherent source like a spectrally sliced broadband ASE source with optical filtering has been proposed [95]. Incoherent injection locking has been shown experimentally by authors in [5]. The setup is shown in Figure 5.3, in which a broad-band light source is generated by pumped erbium-doped fiber, and transmitted through 20 km of fiber before being spectrally sliced by an AWG. The spectrum sliced output of the AWG
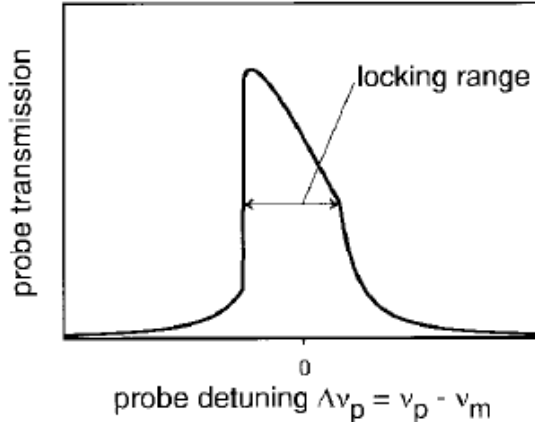
Figure 5.2: The asymmetric locking range of an IL-FP laser diode [4]

is injected into the FP-LD after traveling in the fiber. The light is then modulated, sent back through the fiber, and at the CO, the bit-error-rate and eye diagram on the received light are measured.

Without injection locking, the FP laser diode shows multi-mode behavior as shown in Figure 5.3(b). If modulated, the modes are filtered by the AWG, removing information. The eye diagram and the bit error rate indicate that data transmission has not been successful. The reason for this failure is the random fluctuations in laser mode power which are due to the randomness of the spontaneous emission coupled into each mode. Such randomness creates what is called mode partition noise, which along with the mode filtering causes the eye to close.

On the other hand, when the laser has been injection-locked by the BLS, the locked mode would dominate in power, successful transmission of data can be achieved, resulting in an open eye diagram, as shown in Figure 5.3(c). This experiment highlights the importance of injection-locked laser operation for WDM-PON application.

In theory, injection locked FP lasers could be formulated by using rate equations, and the externally injected narrow-band amplified ASE source can be added to the photon rate equations as an additive term to the spontaneous emission in the injected mode, as derived in [96].

In incoherent injection, the problem of wavelength shift with temperature has been mitigated somewhat by increasing the length of the device so that the FP mode spacing is smaller in wavelength than the injected ASE bandwidth, which is clear from Eq. 5.4 and

83
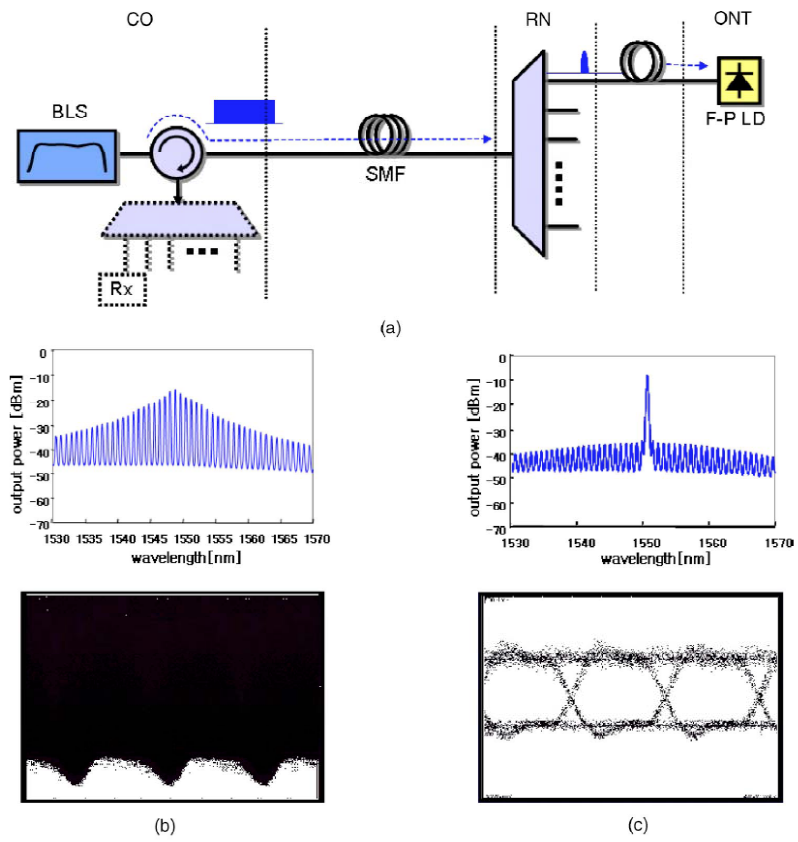
Figure 5.3: (a) An example of IL-FP laser implementation (b)Multi Modes and closed eye without seed injection (c) The modes and eye diagram with BLS as the injection source [5]

5.2. Thus, at least two FP modes occur within the bandwidth of the injected broad-band signal [97]. Even if the modes drift, the device is able to lock onto one of the modes.

However, there is still a decrease in gain of about 2 dB between the case when one of the modes is aligned to the center of the ASE bandwidth and when it is aligned to the edge, and there exists 1 dB of power penalty due to detuning of injection wavelength from the lasing wavelength [32]. Also, the increased length limits the maximum bandwidth of the device due to increased capacitance. Further, the stability of the link over long time with temperature drifting has not yet been reported.

In what follows, a novel device is reported with the purpose of compensating for mode drifts and maintaining mode-locking stability. The device solves temperature drift issues.

5.3   Novel Device Properties

In this section, we propose and demonstrate a new device where we monolithically integrate a phase modulator to the gain section of an ILFP. The earlier version of this work has been presented, and published in [98]. To start with the device design model, let's consider an active region with gain g, interal loss α_g and propagation constant β_g monolithically integrated with a passive phase section with internal loss α_p, and propagation constant β_p. The propagating mode in this resonating structure is reflected by end mirrors with mirror reflectivity coefficients of $r_1 = \sqrt{R_1}$ and $r_2 = \sqrt{R_2}$. The length of the gain section is L_g, and the length of the passive phase section is L_p. The device cross-section and the propagating E-field structure is shown in Figure 5.4.
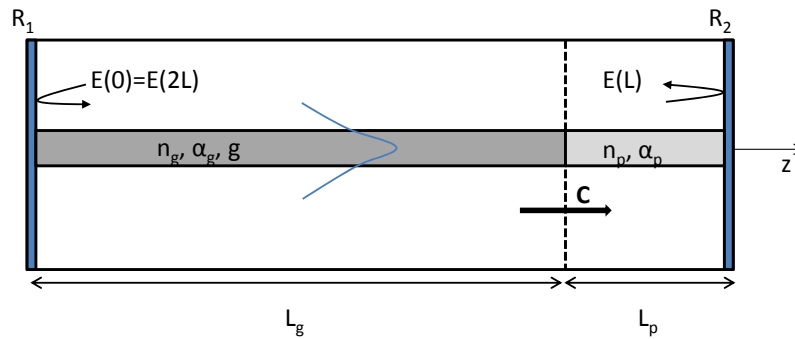
Figure 5.4: Resonant cavity cross section showing the gain and phase regions, as well as the E-field with the condition to achieve lasing

In order for the device mode to reach lasing threshold, the gain in the active region, confined by Γ, must increase to equal the mirror loss and internal losses of active and passive region. As such, the E-field of the mode must replicate itself at the input facet of the device after one round trip traveling into the cavity, i.e. $E(z = 0) = E(z = 2L)$.

The E-field of the mode can be written based on the above boundary conditions, assuming coupling C between the two sections of the device to be

$$Cr_1 r_2 e^{(\Gamma g - \alpha_g)L_g} e^{-2j\beta_g L_g} e^{-\alpha_p L_p} e^{-2j\beta_p L_p} = 1 \tag{5.5}$$

This complex equation should be solved for the magnitude and phase of the E-field separately. The magnitude can be solved for Γg to obtain the threshold lasing gain,

$$g_{th} = \Gamma g = \alpha_g + \alpha_p \frac{L_p}{L_g} + \frac{1}{L_g} ln(\frac{1}{\sqrt{R_1 R_2}}) + \frac{1}{L_g} ln(\frac{1}{C}) \tag{5.6}$$

The above equation indicates that at lasing threshold, the gain of the active region equals the internal and mirror losses in addition to the losses induced by bad coupling between the two sections. Therefore, it is important to increase the coupling efficiency as close to unity as possible; for this mode matching in the design of two sections is critical.

The phase of the wave must remain the same after one round trip travel in the cavity. Obtaining the phase part of Eq. 5.5 requires $exp(-2j\beta_g L_g)exp(-2j\beta_p L_p) = 1$, and therefore $\beta_g L_g + \beta_p L_p = m\pi$. Expanding $\beta = \frac{2\pi n}{\lambda}$, and assuming n_g to be effective index of gain region, and n_p to be effective index of phase region, the phase condition of the resonating cavity can be derived as [54]

$$\lambda = \frac{2}{m}(n_g L_g + n_p L_p) \tag{5.7}$$

m is the longitudinal mode number. From the above equation, it is evident that only light of certain resonant wavelengths are permitted to exist in the cavity. This is in accordance with the discussions in previous section and Eq. 5.1 for FP modes. Importantly, this equation shows that by changing the effective index of phase section n_p, the frequency of lasing can be modified.

In our design, the phase modulator can be used to change the wavelength of the FP modes so that it matches the wavelength of the injected signal. Similar integration of phase modulators with gain sections has been done for multi-section tunable lasers to stop mode hopping [99]. However, in our work, the focus is toward WDM-PON and keeping the integration method simple. The optical gain chip consists of an 800 μm long active section and a 200 μm long phase section for a total device length of 1 mm. Total length was determined by the design rules of the commercial foundry where this device was fabricated.

5.3.1 Phase Section

The core of the phase section consists of a bulk waveguide with λ_g=1.3 μm, and with thickness of 130 nm also in a single step SCH region. The SCH regions of the two sections are adjusted such that the mode profiles in the two sections are nearly identical to give maximum coupling efficiency and reduced reflections, and the SCH thickness is 300 $\mathring{A}$ each. The phase section operates on the principle of free carrier induced refractive index change, Δn, [100]

$$\Delta n = -\frac{e^2\lambda^2}{8\pi^2 n\epsilon c^2} \cdot \left(\frac{N}{m_e^*} + \frac{P}{m_h^*}\right) \tag{5.8}$$

Where e is the electron charge, ϵ is the permittivity of free space, λ is the wavelength of light, n is the refractive index of the unperturbed media, and m_e^* and m_h^* are the effective mass of electrons and holes, and N and P are the injected electron and holes per unit volume. It can be seen that Δn is directly proportional to λ^2, $1/n$ and the induced carriers. With a change in the free carriers, a phase shift $\Delta\phi$ can be calculated as follows where L is the device length

$$\Delta\phi = \frac{2\pi L}{\lambda} \cdot \Delta n \tag{5.9}$$

In order to identify the existing modes in this devices, and to calculate the modal overlaps and similarities between the devices, simulation modeling of the modes was done using FIMMWAVE mode solver [69]. The fundamental TE mode that the structure supports is shown in Figure 5.5. The mode is confined to the bulk waveguide with a confinement factor of Γ=0.21. The effective index for this mode is n_{eff}=3.19. The effective index is important for mode matching condition to the gain section. The vertical farfield angle is 34.4°.

5.3.2 Gain Section

The gain section consists of multiple 1% compressively strained quantum wells (QW) in a dilute SCH. The QW layers have a thickness of 70 $\mathring{A}$ followed by 120 $\mathring{A}$ of barrier thickness. The thin QW layers help with achieving higher gain, along with better temperature performance of the laser. The compressive strain promotes TE mode lasing, by enhancing the HH band. Therefore, any existent TM modes will not be amplified, and the lasing will basically consist of TE modes. The compressive strain is easy to achieve and robust, meaning that several layers could be grown on unstrained InP substrate, without breakage of the material.

87
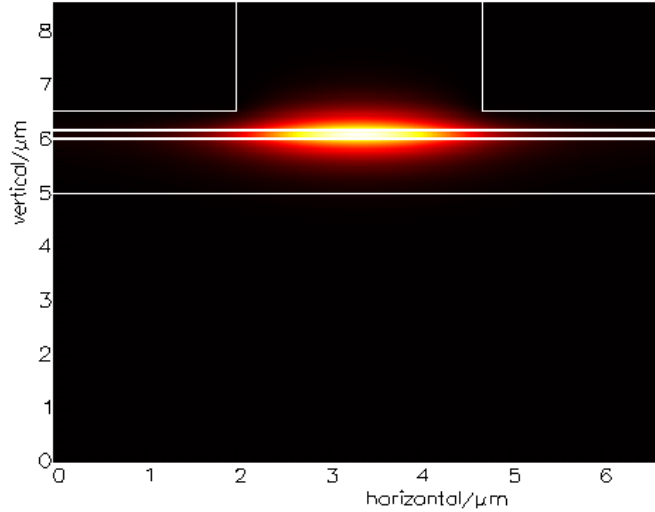
Figure 5.5: Fundamental TE modes of the phase section with 21% confinement in the undoped region

The device is made of two SCH layers surrounding the QWs. These layers have higher bandgap, and will not absorb the photons generated in QWs. The SCH layers help with confinement of the optical mode to the active region. They also help with trapping of electrons and holes in the QW region. For this device, the layers are 200 and 300 $\mathring{A}$ respectively. Changing the width of SCH layers will change the vertical farfield divergence angle of the output beam.

The bandgap structure of the proposed device is shown in Figure 5.6. The active region consists of 4 QW layers, with a rib structure, with a rib width of 2.7 μm. The layer structures are shown in Table 5.2. The cap layer has a bandgap smaller than that required for lasing wavelength, and hence will absorb any photon incident on it. Therefore, the vertical guided electric field should not see the cap layer. If the upper clad is thick enough, this will happen. On the other hand, the upper clad should not be too thick as to increase the electrical resistance and degrade laser performance. Therefore, the upperclad is 2.4 μm thick, and the mode is strictly confined to the QW and SCH layers, and away from the cap layer. The rib etch is 2.05 μm. In this figure, the fundamental optical mode is shown as red dashes, and about 27% of the light is confined to the shown layers.

A simulation was performed using FIMMWAVE to evaluate the modes this gain structure supports. The fundamental TE mode of this structure is shown in Figure 5.7. The mode is confined to the SCH and QW layers with Γ=0.27, the confinement factor in the

88

Layer No.	Layer Name	Material	$\lambda_g(\mu m)$	Strain %	Thickness (μm)	Index	Doping (cm^{-3})	Doping Type
13	Cap	InGaAs	1.64	0	0.1	3.643	2e18	p+
12	UpperClad	InP	0.92	0	2.4	3.167	3e17-1e18	p-variably doped
11	SCH	InGaAsP	1.1	0	0.03	3.282	–	i
10	SCH2	InGaAsP	1.25	0	0.02	3.378	–	i
7	Quantum Well	InGaAsP	1.6	0.9	70 Å	3.6	–	i
6	Barrier	InGaAsP	1.25	0	120 Å	3.378	–	i
5	Quantum Well	InGaAsP	1.6	0.9	70 Å	3.6	–	i
4	SCH2	InGaAsP	1.25	0	0.02	3.378	–	i
3	SCH	InGaAsP	1.1	0	0.03	3.282	–	i
2	Lower clad	InP	0.92	0	1	3.167	7e17	n
1	Substrate	InP	0.92	0	100	3.16	8e18	n

Table 5.2: Material composition of the laser
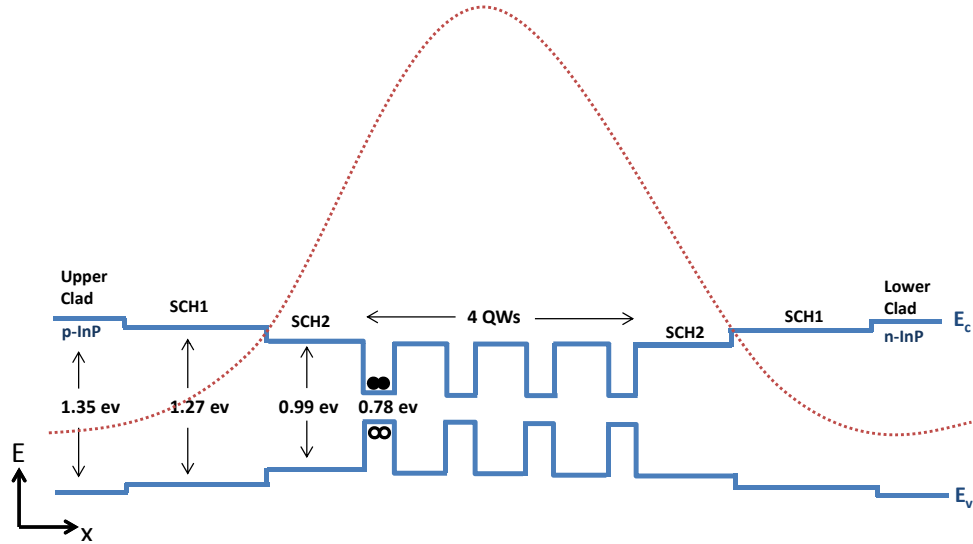
Figure 5.6: Bandgap design of the Gain Section of integrated FP device (Solid lines represent energy levels and the dashes represent optical mode)

QWs alone is Γ=0.05. The effective index of this mode is Neff=3.19, which matches the fundamental mode of the phase section to the third order of decimal of effective index. The farfield divergence angle in the vertical position is 34.8 °. It is evident that the modes of the two devices match well for integration.

5.3.3 Monolithic Integration

The two structures are monolithically integrated using butt-coupled re-growth [101] in three steps using solid state molecular beam epitaxy (MBE) via a commercial foundry. In the first step, the structure is grown up to the phase waveguide. Using a large area mask, the core of the phase waveguide is etched where it is not needed and the active waveguide structure is grown butt-coupled to it. Also before the regrowth, the etch depth is measured and a spacer layer of InP is grown before the active region to ensure that the two cores are aligned.

In the third growth step, a common p-doped cladding is grown over the complete structure. The lateral confinement in the structure is provided by a ridge waveguide. The ridge waveguides were 2.7 μm wide and were fabricated by dry etching in Ch4/H2/Ar based reactive ion etcher. The highly doped cap layer between the active and phase section was etched to reduce the cross-talk between the two sections. A part of the p-cladding was
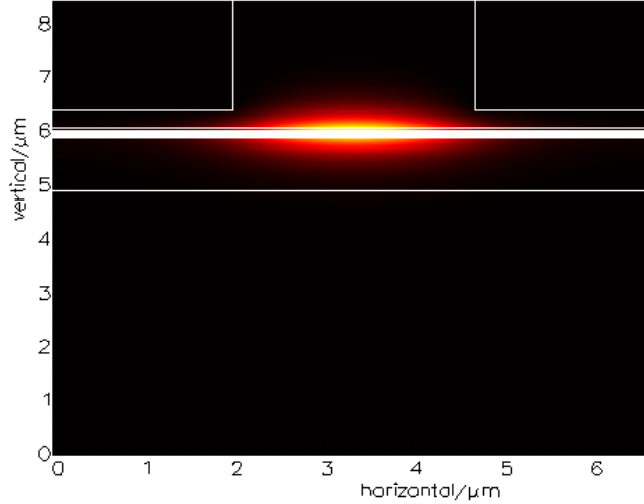
Figure 5.7: Fundamental TE modes of the gain section with 27% confinement in the active region

also etched especially on the sides of the ridge waveguide. Further, the metal electrodes were placed 25 μm apart. The resulting isolation between the two structures was greater than 2 KΩ. Since both the electrodes are forward biased, the isolation was considered to be sufficient.

The P-doped InP is doped with Beryllium (Be). The doping concentration for P+ region is P$^+$=2 $\times$ 10^{19} cm^{-1}. The p-doped concentration is ranging from 1 $\times$ 10^{18} to 8 $\times$ 10^{18} cm^{-1}. The n-doping happens with Sulfur (S) and the doping concentration is N=7 $\times$ 10^{17} cm^{-1}. Since carrier mobility is lower with Be doping, the P-doping is placed on top of the device, so that the carriers have less traveling distance to the intrinsic region. The cross section of this device is shown in Figure 5.8.

The fabricated device was cleaved to a length of 1 mm. The length was mainly chosen using a standard processes to keep the cost low and not based on a device optimization point of view. Three different devices were fabricated, a control device with only the gain section; an integrated device with a 800 μm long gain section and a 200 μm long phase section, and an integrated device with 900 μm long gain section and 100 μm long phase section.

91
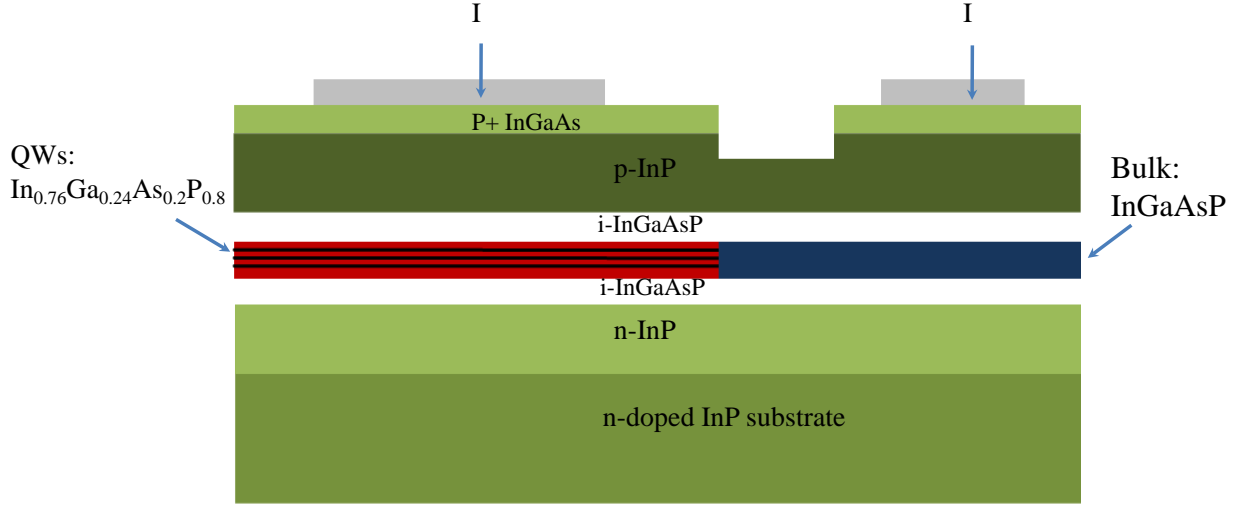
Figure 5.8: Cross-section view of the device

5.3.4 Reducing Reflectivity between 2 Sections

The regrown active region is shown schematically in the shaded part of Figure 5.9. The interface between the waveguides was kept at an angle of 15° to reduce any reflections that may occur due to the butt-joint of the two waveguides. Assuming a Gaussian field distribution, the effective modal reflectivity is given by the following equation, assuming R_0 to be Fresnel Reflectance, n the effective refractive index of the waveguide, W the mode width, θ the angle from normal of the facet, and λ the wavelength of the device [102].

$$R = R_0 \cdot exp - (\frac{\pi n W \theta}{\lambda})^2 \tag{5.10}$$

The Fresnel reflectance between the two material in gain and phase sections, is given by $R_0 = (\frac{n_1-n_2}{n_1+n_2})^2$ when the transmission and reflection are at the right angle to the facet. In this case, the reflection is negligible, since the two material have very similar effective indices, n_1 and n_2. By choosing the angle $\theta = 15^o$ and for $n = 3.19$, $W = 2\mu m$, and wavelength of $\lambda = 1.55~\mu m$, the reflections back into the waveguide smaller than 10^{-6}. The angle will also insure there are no reflections at the boundary of two devices in case of fabrication misalignments.
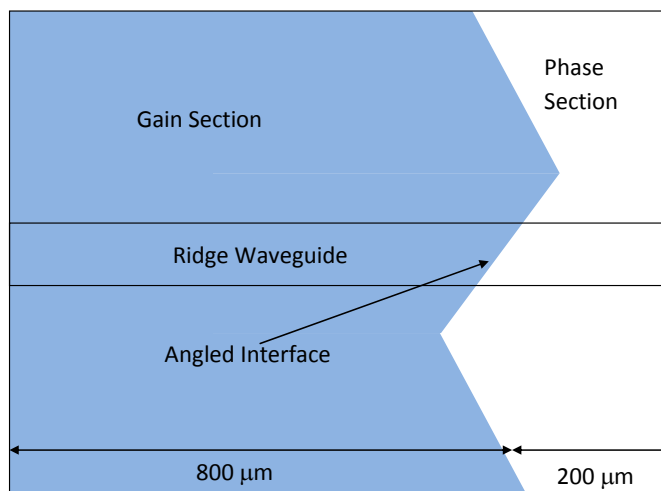
Figure 5.9: Schematic of the top view for the device showing the gain amplifier and the phase section

5.4 Experimental Results

The first experiment relates to the lasing characteristic of the device. Figure 5.10 shows the light versus current (LI) characteristics of the device for different lengths of the phase section including a control device with no phase section. As seen from the figure, the performance of the device does not degrade with the integration of the phase section showing the loss due to the butt-coupling is minimal. The LI curves deviate at higher currents due to thermal effects as the active length gets shorter for longer phase section devices.

5.4.1 Temperature Characteristics

Figure 5.11 shows the temperature performance of a device with a 200 μm long phase section. The chip shows very good temperature performance and 50 mW of optical power is achieved at a current of 300 mA even at high chip temperature of 50° C. We could not go to a higher chip temperature due to limitations of TE cooler in our experimental setup.

The characteristic temperatures T_0 and T_1 in a laser represent threshold current and external quantum efficiency of a laser. The former parameter is more dominant in waveguide-based devices, while the latter would be a significant factor in high power laser applications.
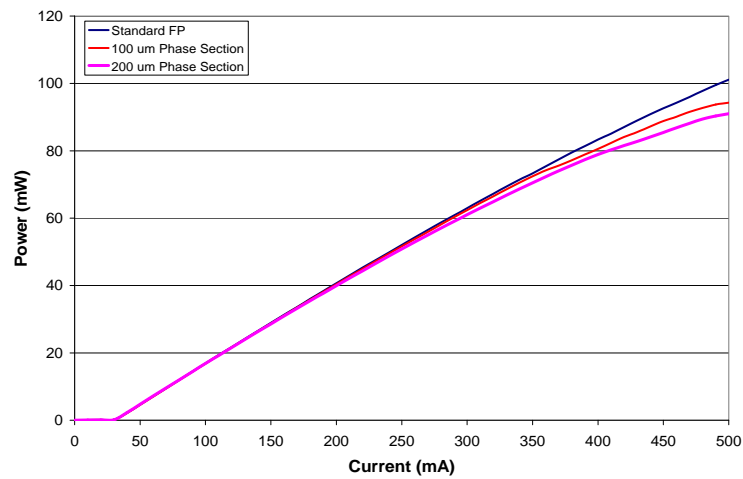
Figure 5.10: LI curves for different phase section lengths
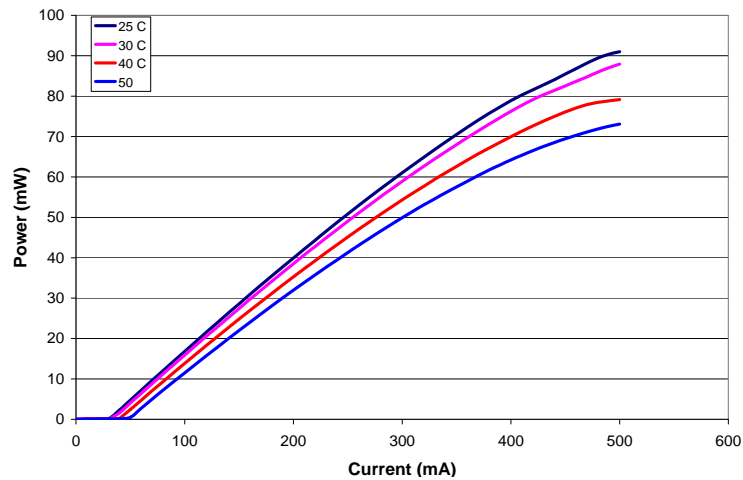
Figure 5.11: LI curves at different temperatures with 200μm long phase sections

T_0 is measured as follows:

$$T_0 = \frac{\Delta T}{ln(I_{th2}/I_{th1})} \tag{5.11}$$

where ΔT is the change of temperature and I_{th1} and I_{th2} are the laser threshold current before and after the temperature change. If we plot the change in threshold current, versus the change in temperature, the slope would give us the value of T_0. It is desirable to have a minimal change of laser threshold current as the temperature changes, and therefore a larger value of T_0 is better. T_1 can be calculated from the LI curve as follows:

$$T_1 = -\frac{\Delta T}{ln(S_2/S_1)} \tag{5.12}$$

S_1 and S_2 are the slopes of the LI curve before and after the change in temperature.

The characteristic temperatures, T_0 and T_1 were measured for the three different devices. The change of threshold and slope with temperature is shown in Figure 5.12, and the numbers are tabulated in Table 5.3. T_0 degrades slightly with the addition of the phase section. The degradation could be due to a slightly higher carrier concentration for shorter active region lengths, resulting in an increase of Auger recombination [67].

Device Type	T_0	T_1
Standard FP	60K	212K
FP with 100 um Phase Section	57K	212K
FP with 200 um Phase Section	54K	227K

Table 5.3: Characteristic Temperature measurements for the laser

5.4.2 Phase Section Current

Figure 5.13 shows how the FP modes change in wavelength for a 200 μm long phase section as the current on the phase section is increased from 0-18 mA. A round trip phase shift of greater than 2π is achieved at a current of 14 mA on the phase section of the device. So by changing the current from 0-14 mA, a FP mode of the device can be made to coincide with the injected wavelength.

Figure 5.14 shows the change in phase and optical power as the phase current is increased for the 200 μm long and 100 μm long phase sections. For the 200μm long phase section, the optical loss associated with a 2π phase shift is 0.8 dB. For this measurement,
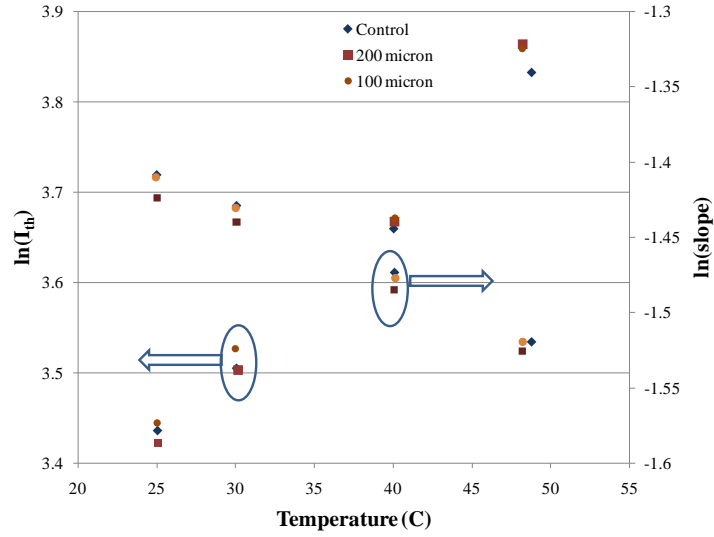
Figure 5.12: wavelength and optical power change as current on phase section is increased
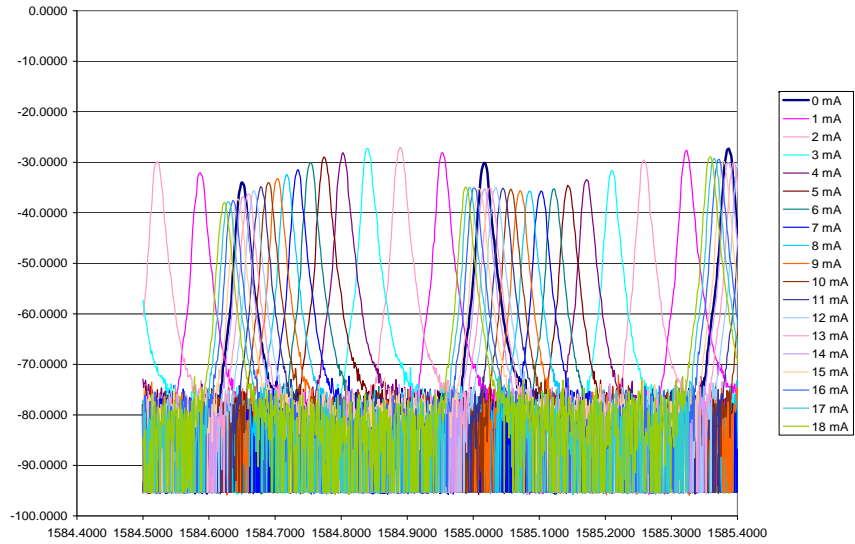
Figure 5.13: Change in wavelength of FP modes as current of phase section is increased

96

the temperature of the chip was 30° C. However, less than 2π of maximum phase shift is achieved for the 100 μm long phase section. This is expected as the phase shift is also directly proportional to the length as predicted by Eq.5.9.
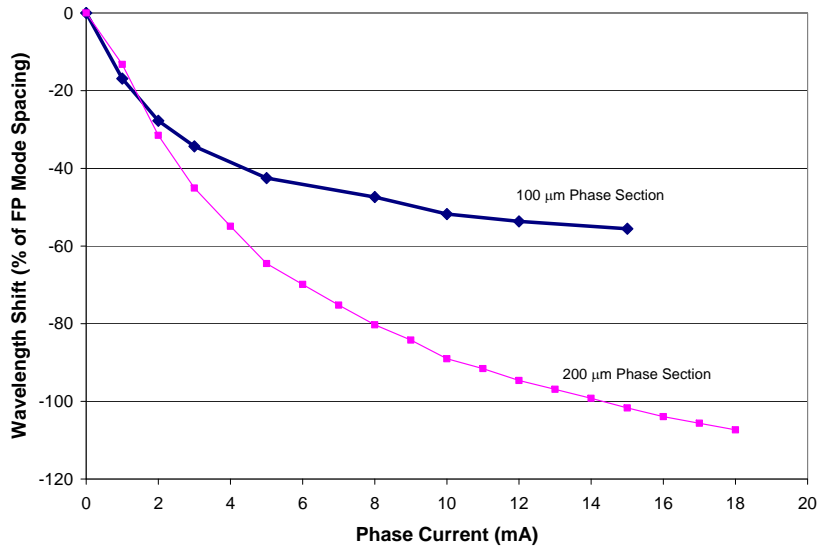
Figure 5.14: FP wavelength and optical power change as current on phase section is increased

5.4.3 Farfield Measurements

Vertical farfield plots were also measured from both sides of the device. On average, the full width half maximum (FWHM) farfield from the gain section was 29.7 degrees with a standard deviation of 0.27 degrees and from the phase section side was 29.9 degrees with a standard deviation of 0.8 degrees. The farfield plots from the gain section side and from the phase section side are shown in Figure 5.15. This confirms our design where we tried to match the modes of two devices. The radiation patterns seen near the substrate of the phase section farfield are indicating radiative modes due to misalignments in the fabricated devices between the two sections.

A total of 10 devices of each type were measured from both the facets. Identical nature of the farfield divergence angles shows the similar nature of the optical modes in the two sections of the device confirming the design. Further, minimal radiation features were seen in the farfield plots again demonstrating the coupling between the two sections.
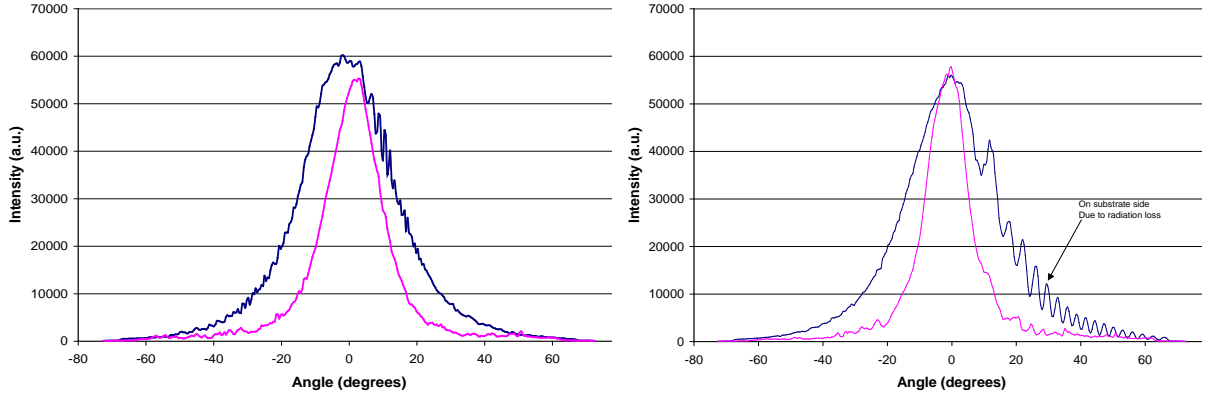
Figure 5.15: (a) Transverse and lateral far-field plots from the gain section facets (b) Transverse and lateral farfield plots from the phase section facet

5.4.4 Frequency Response

Relaxation oscillation frequency is the frequency determining the speed of a lasing device. For any given bias, the device can operate at twice this frequency. The relaxation osciallation frequency (ω_R) is presented by [54]

$$\omega_R = \left[\frac{\Gamma \nu_g a_1}{qV} \eta_i (I - I_{th}) \right]^{1/2} \tag{5.13}$$

Where I is the injected current, Γ is the confinement factor, ν_g is the group velocity, a_1 is the differential gain, η_i is the laser quantum efficiency and V is the volume of active region. It is desirable to increase the differential gain, minimize the mode volume, and increase the current relative to threshold for maximum achievable bandwidth.

For the uncoated devices, ω_R was experimentally measured. Figure 5.16 shows the relaxation oscillation frequency relation with sqrt(I-I$_{th}$). As expected a linear relation is achieved with the relaxation oscillation frequency at 6 GHz at a current of 46 mA, corresponding to a value of 4 for sqrt(I-I$_{th}$). While it has been shown that under injection the relaxation-oscillation is reduced [103], this figure gives an ultimate limit to the maximum speed of the laser.
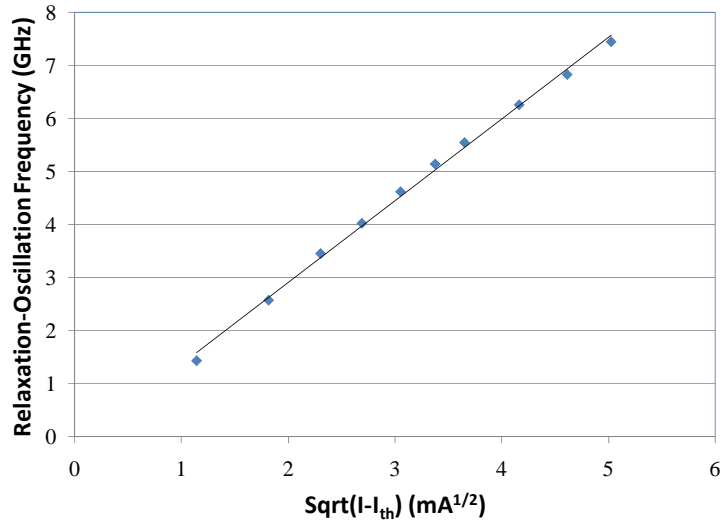
Figure 5.16: Relaxation oscillation frequency for the Fabry Perot Laser with increasing current

5.4.5 Injection-Locked Device Performance

For some devices, the back facet was coated with greater than 90% high reflection coating and the front facet with reflectivity between 2-3%. Experiments with injection locking of the device were considered using the setup shown in Figure 5.17. Broadband light from a high power EDFA was spectrally sliced with a 0.6 nm band pass filter and injected into the laser through a circulator. A variable optical attenuator was used to change the injected optical power. The signal from the injected lasers was measured using an optical spectrum analyzer. Two FP modes lie within the spectrum of the injected signal.
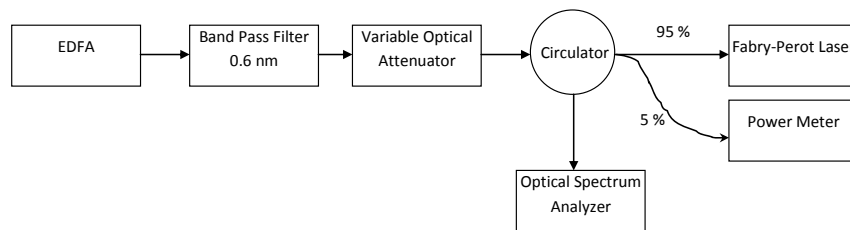
Figure 5.17: Experimental setup for injection locking experiment

The light versus current characteristics for different injected powers are measured and

shown in Figure 5.18. The optical power was measured after coupling the laser to the fiber using an aspheric lens. The coupling efficiency was estimated to be 2 dB. Further the injected power was measured by tapping a part of the optical signal before coupling into the chip. It is observed that as the injected power is increased, and the threshold current of the laser starts to decrease. The reduction in threshold current is due to injection locking of the laser to the injected signal. The slope is nearly constant for different injected powers. This is also expected as the slope only depends on the internal quantum efficiency, internal loss and mirror loss which do not change significantly with injection. This is confirmed in the spectral measurements shown in Figure 5.19.
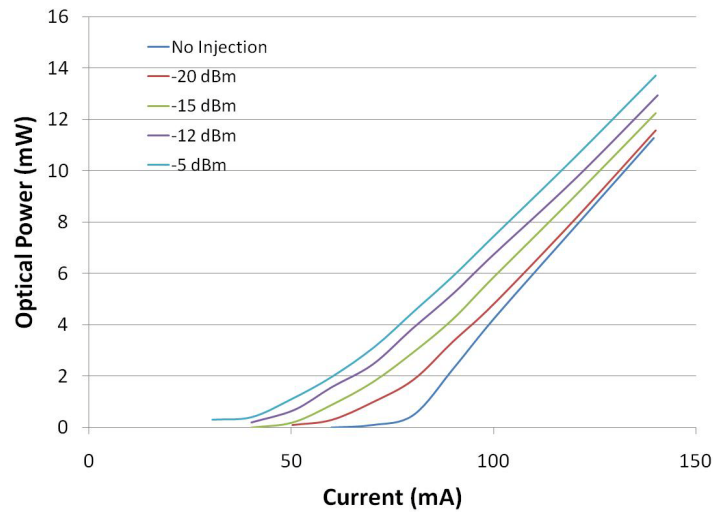
Figure 5.18: Light versus current characteristics for different injection powers

The measurement was done at a current of 75 mA, just above the threshold current of the device without injection. As the injected power is increased, the lasers start to lase on the wavelength of the injected signal, and the side mode suppression ratio (SMSR) improves. For an injected power of -12 dBm, SMSR is greater than 40 dB and for -5 dBm of input power, SMSR is greater than 47 dB. In this figure, we have normalized the spectrum to the peak power in the fundamental lasing mode for a measurement so that SMSR can be compared directly with different injection powers. It is to be mentioned that the peak power does change. Also for this measurement, we had manually changed the phase current to match the FP mode to the injected wavelength by measuring the output

optical power and maximizing it at a gain section current of 75 mA. The phase current was approximately 6 mA.
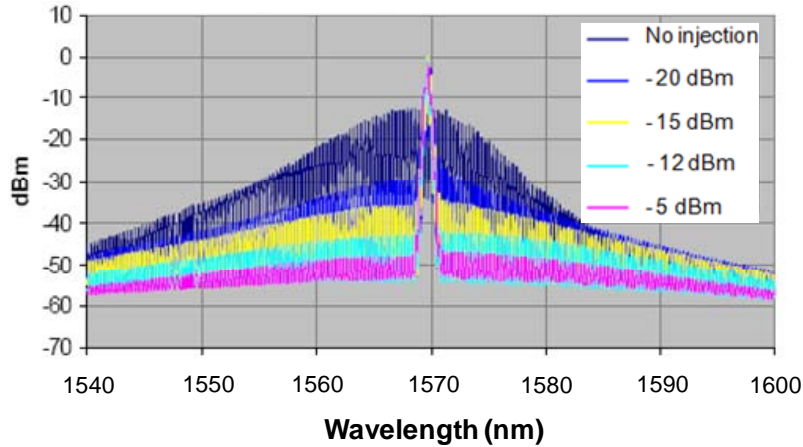
Figure 5.19: Spectrum of the laser as the injection power is increased

Figure 5.20 shows how the injection locking changes as the wavelength of the input signal is changed from the gain peak of the device. The injected power is -15 dBm. As can be seen the SMSR is greater than 30 dB for a full width of 16 nm around the gain peak. However, as the injected signal is 15 nm detuned from the center wavelength, a SMSR of less than 10 dB is achieved, and the device seems to be operating as a Fabry-Perot amplifier. The injection bandwidth may be improved by increasing the power of the optical signal.

5.5 Summary

To conclude, a novel design for solving the problem of shifts in the mode of a FP laser due to temperature variations has been discussed. By integrating a phase modulator to the laser, and changing the input current, the mode shift can be achieved and mode locking to an external laser is guaranteed. Various performance measures have been plotted, which show that the laser can operate at high temperatures. The characteristic temperatures T0 and T1 are around 54 K and 227 K. The relaxation oscillation frequency at a current of 46 mA is 6 GHz. Further under injection locking greater than 45 dB side mode suppression ratio is achieved.
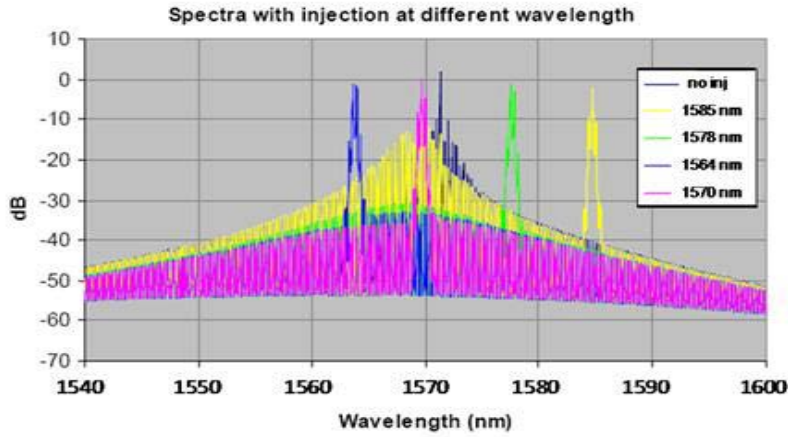
Figure 5.20: SMSR of the locked mode as the injected wavelength is detuned from the gain peak for an injected power of -15 dBm

Alternatively, external wavelength-locking can be achieved by using multiwavelength Slotted FP laser [104]. This type of laser has several resonating wavelength channels within a few nanometers, and the laser can be tuned by changing current/temperature and hence the locked wavelength channel. In this structure, there is no designed pre-selection of which mode will lase and any of the channels within the tuning range of a seed source can be wavelength-locked to form as a single-mode laser. As a result, the control circuit for the slotted FP laser would be very complicated for cost-effective upstream source WDM-PON.

With an automatic current control circuit, the ILFP could be deployable in WDM-PONs as a colorless source. The circuit controlling the amount of current needed to adjust the wavelength of the Fabry-Perot mode can be designed similar to the discussion in [105] where an automatic control is proposed to control the wavelength of a tunable laser in OLT of a WDM-PON network. The integrated device can provide a robust solution for WDM-PON applications in terms of wavelength drift of the laser.

Chapter 6

Conclusion and Future Direction

A thorough look at the progress of broadband services like voice, video and online gaming tells us that the future access networks must move toward optical fiber systems that have a large bandwidth and low capital cost. The development of WDM-PON is the ultimate step in achieving a future-proof solution for broadband services demand. In a WDM-PON, each user is assigned a dedicated wavelength. This features allow for virtual P2P connections, inherent security, scalability, and most importantly, huge user bandwidth. For its design, it is favored to create wavelength-independent ONUs, labeled as colorless-ONUs. Colorless ONUs eliminate wavelength management at the customer premises, and reduce CAPEX costs.

Much research has been performed on semiconductor optical devices, network architectures, and system requirements for achieving best the WDM-PON solutions. Those include use of reflective sources like RSOAs, VCSELs, and injection-locked FP laser diodes at the ONU. The OLT allocates a bank of DFB laser sources for downstream traffic, and BLS laser diodes are used in conjunction with AWGs for generation of seed-light for upstream traffic. For direct modulation of the upstream traffic, the achievable data rates are limited due to limitations imposed by the optical components. We have proposed several novel devices to bring flexibility, and improved performance to the next generation optical access networks.

The first demonstrated device is a polarization-independent RSOA operable over the L-band. The device design effectively combines active region requirements for polarization-independence with operation in the longer wavelength bands. The RSOA has an optical gain of greater than 21 dB and PDG of less than 1 dB over the band. The packaged saturation power is 1.0 dBm and the NF is 10 dB. The 3-dB modulation bandwidth is 1.3

GHz, making it suitable for 1.25 Gb/s operation. Although RSOA devices are inherently slowfor direct modulation, we have shown that they have faster response time, and can be deployed for nonlinear applications such as logic gates.

Later, the saturation characteristics of an RSOA were analyzed in detail and compared to the conventional SOA. Through theoretical investigations and comparison with available devices, we clearly show the NF of an RSOA to be higher than an SOA due to carrier saturations. This undesirable effect is shown to be mitigated by non-uniform carrier injection into the device to achieve a lower RSOA NF. Otherwise, the effect of NF on the system performance can be limiting. Especially in spectrally-sliced WDM systems, great power penalties are induced due to RSOA beating noise. We have shown that the device NF can increase further by changes in bias current, temperature of operation, and wavelength of operation.

Finally for RSOAs, we highlighted the importance of AWG band shape in spectrally-sliced WDM-PON systems by formulating the filtering effect that cuts off the tails of the upstream signal and deteriorate the received signal. System simulations along with experimental analysis show the closing of eye observed after every AWG filter. As a result, Gaussian type AWGs should not be deployed in these systems due to pattern dependent effects, where a BER floor is not achievable. For WDM-PONs systems, it is important to use flat-band athermal AWGs to reduce the filtering effects, and reach acceptable BER for WDM-PON. To conclude, RSOA does not seem to be an ideal device for WDM-PON applications, and FP laser diodes might offer better ONU solutions.

Therefore as an alternative to RSOA, in this thesis we finally demonstrated a novel IL-FP laser with mode-lock stability. It was earlier stated that a maximum bitrate of 1.25 Gb/s was achievable due to the shift in FP modes with temperature variations [106]. Our novel device deploys a phase modulator which is monolithically integrated to a Fabry-Perot diode laser. By changing the input current to the phase modulator, the refractive index of the medium changes, and the laser modes would shift in wavelength. This method guarantees mode-locking to an external seed laser source, even if a shorter length device with larger mode spacing is designed. For the current design, considering a phase section length of 200 μm, integrated with 800 μm of FP device length, $I_{2\pi}$=14 mA for the full wavelength span. Various performance measures have been plotted, which show that the laser can operate at high temperatures, without noticeable performance degradations. The relaxation oscillation frequency at a current of 46 mA is 6 GHz, so the laser can operate at 10Gb/s. Further under injection locking, SMSR greater than 45dB is achieved. With an automatic current control circuit, this system could be deployable in WDM-PONs as colorless sources.

6.1 Future work

This project proposed the reflective device designs for WDM-PON ONU, to improve performance and data rates and highlighted some system limitations. The final leap for this project is to design Photonic Integrated circuit (PIC) chips for deployment at the OLT, and most importantly at the ONU. The PIC at the central office would compose of a bank of lasers, receivers, and a WDM multiplexer all on one chip. At the ONU, the integrated chip would consist of a reflective architecture, a receiver and a filter/combiner. A schematic is depicted in Figure 6.1. By having all the required optical components on a single chip, mass production, ease of installation and eventually cost reduction would be achieved. In the future steps, several goals are proposed,

- Design and fabricate an RSOA with non-uniform current injection into the device, with higher current injection in the front facet, and lower at the back facet to improve the NF characteristics of RSOA.

- Look into temperature performance of RSOAs by investigating other active regions like Quantum Dots.

- Design a control circuit for the IL-FP laser device to automate the flow of current into the phase section of the device and maintain wavelength-locking with drifts in temperature and power. This way higher bitrates would be realized.

- Create a hybrid integration platform on Si for integration platform for integration of laser, receiver, and combiner filter on a single chip, in order to yield high-fabrication and perhaps low cost components.

- Demonstrate a WDM-PON system composed of PICs at the OLT, and the ONU with high performance, and great repeatability.

This would provide a complete framework for the optical components realizable in a future-proof WDM-PON system.
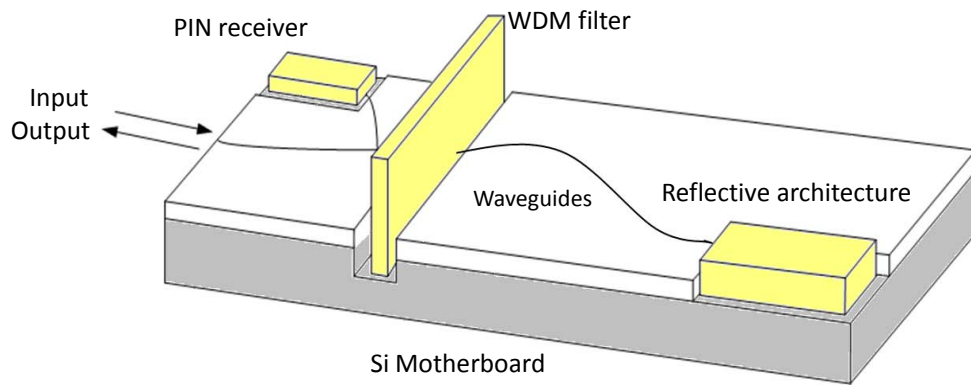
Figure 6.1: A monolithically integrated transceiver at the ONU with WDM-filter, receiver and reflective modulator on a single chip

APPENDICES

Appendix A

VPI model: SOA Dynamic Response

Figure A.1 is a screen shot of the model used for evaluating dynamic response of semiconductor amplifier devices. In this model the input consists of a CW laser source (*LaserCW*) with 10 MHz linewidth operating at frequency of 193.1 THz and a pico-second pulse with a lower frequency of 190 THz. The pico-second pulse is modeled with an impulse function (*FuncImpulseOpt*) of duration a sample window, and the pulse peak power is set to 150 mW. Both signals pass through a coupler with coupling factor=0.5 (*X-Coupler*). Each output arm of the coupler feeds the input ports of a SOA, in addition to a RSOA with same characteristics.

Using a Transmission Line Model (*SOA TLM MS*), the multi-section SOAs are modeled. The device structure and carrier dynamic parameters used for modeling carrier dynamics of both amplifier device are given in Table A.1. The facet reflectivity for each middle section is set to zero for both devices. The end facets have 10^{-4} reflectivity for SOA. As for the RSOA the back facet has 0.99 reflectivity, while the input facet has 10^{-4} reflectivity.

A *DC-Source* module provides constant amplitude electrical signal to each amplifier, and the output of each amplifier is filtered using a bandpass filter (*FilterOpt*) with rectangular band shape of 10 GHz. The dynamic response is displayed and analyzed using *SignalAnalyzer* module with *Scope* option set to On. An electrical low-pass filter (LPF) in this module helps eliminate noise, to view the dynamic response properly.

The results of this analysis are discussed in Section 2.7.

Parameter	Symbol	Value
Linear Recombination Coeff.	A	0
Spontaneous Emission Recombination Coeff.	B	$1e\text{-}16\text{m}^3\text{s}^{-1}$
Auger Recombination Coeff.	C	$1.3e\text{-}41\text{m}^6\text{s}^{-1}$
Differential Gain	g_0	$2.5e\text{-}20\text{m}^2$
Transparency Carrier Density	N_0	$1e\text{+}24\text{m}^{-3}$
Internal Material Loss	α	$3000m^{-1}$
Active Region Waveguide Width	W	$1.5\mu m$
Active Region Thickness	d	$100nm$
Device Length	L	$800\ \mu m$
Operation Current	I	$60mA$

Table A.1: Parameters used for RSOA device in the Gain recovery model (the SOA device has double the length and operation current than above)
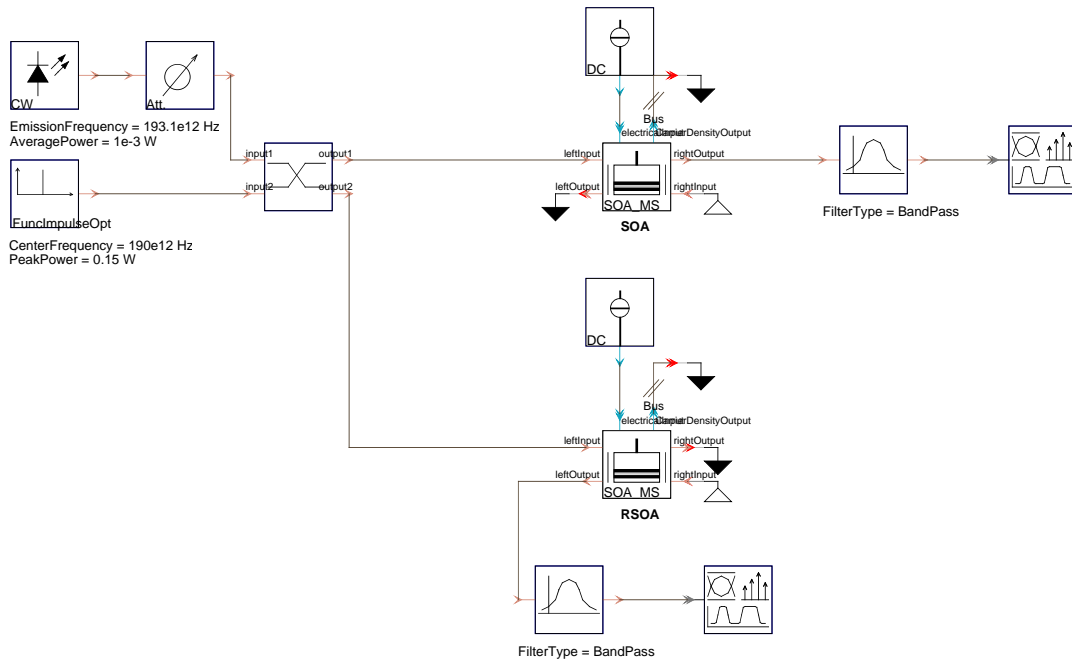
Figure A.1: VPI model used for determining the gain recovery time of SOA and RSOA

Appendix B

VPI model: Effect of RSOA NF on System Performance

The VPI model used for determining the effect of coherently-injected RSOA NF on System performance is shown in Figure B.1. In this model, the bit rate is set to be 1.25×10^9 bits/s, and the seed source input to the RSOA is a CW source with input power of 25 μw operating at 193.1 THz. The output is filtered by an AWG (*AWG M N*) with channel frequency of 193.1 THz, and single input-output port.

The RSOA is modeled using the transmission line model (*SOA TLM MS*) with parameters tabulated in Table B.1. To model the spontaneous emission noise of RSOA, *inversion parameter* model is used and the inversion parameter (n_{sp}) is varied from 2-10 in this model. The effect of increased spontaneous emission noise is then measured at the detector.

The RSOA is modulated directly using a random seed generator (*PRBS*) which is NRZ-coded (*Coder NRZ*). The result runs through a Gaussian filter edge-smoothing module (*RiseTimeAdjust*). This changes the rise time to bitrate/4. The bits then go through a laser driver (*LaserDriver*) with 60 mA of bias current, and 80 mA of drive amplitude. The output goes through a bandpass filter with bandwidth equal to 40 times the bitrate.

The output of RSOA is then sent through a polarizer with 20 km of universal fiber. A VOA (*Attenuator*) controls the received signal power level into the RSOA. The signal is detected by a photodiode, before going through a BER analyzer. The module estimates the error probability assuming Gaussian statistics for optical beat noise. The detected signal has thermal noise and shot noise added to it.

Parameter	Symbol	Value
Active Region type		Bulk
Device Length	L	600 μm
Facet Reflectivity 1	R_1	1e-5
Facet Reflectivity 2	R_2	0.99
Confinement Factor	Γ	0.2
Differential Gain	g_0	30e-23 m^2
Noise Model		Inversion Parameter
Inversion Parameter	n_{sp}	2

Table B.1: Parameters of the RSOA used for NF analysis of this device

To model the ASE-injected WDM-PON shown in Figure B.2, an EDFA seed source is used. In the VPI tool, the EDFA is modeled using a doped fiber (*DopedFiber*) with 100 m of fiber length, optically pumped by a CW source (*LaserCW*) emitting at 1480 nm with power of 40 mW. The input is then spectrally-sliced using the AWG module (*AWG MN*), with 1 input/output port and ideal transfer function. The average power spectrally-sliced output of AWG is controlled by a VOA, and injected into the RSOA model. The RSOA output similar to previous setup is sent through 20 km of optical fiber, and detected at the receiver.

The results of this analysis are presented in section 3.5.
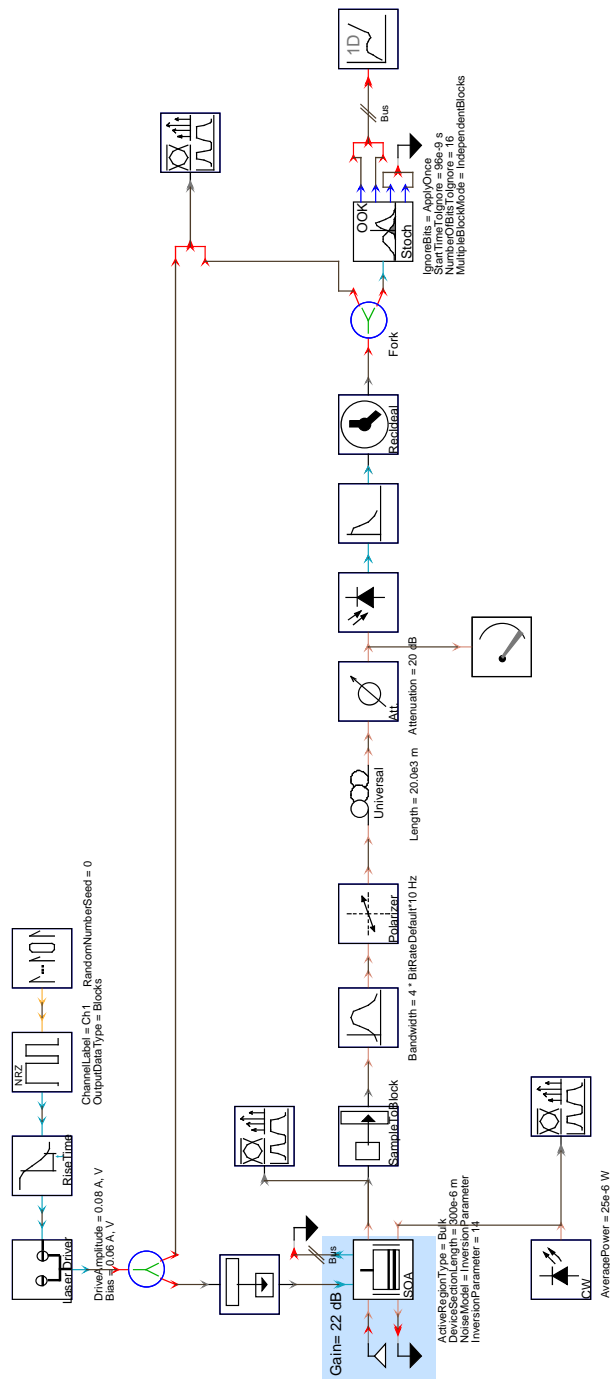
Figure B.1: Setup for NF effects of coherent-injected RSOA in a WDM-PON system
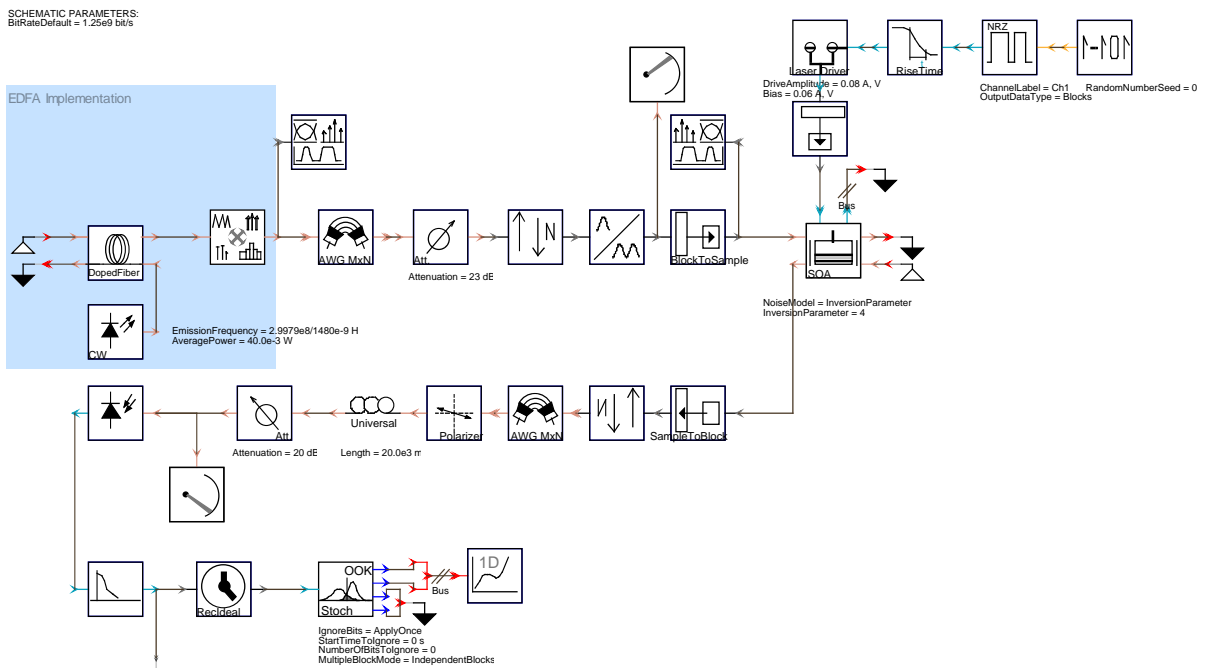
Figure B.2: Setup for incoherent-injected RSOA in a WDM-PON system

Appendix C

VPI model: AWG Filtering Effect

To determine the AWG effects in spectrally-sliced PONs using RSOAs, a screen shot of the VPI model is shown in Figure C.1. The ASE-injected modeling is similar to the one discussed in Appendix B, and the RSOA parameters for this model are used as default values of VPI. This models uses three AWGs to present the seed signal into the field AWG, the upstream signal out of field AWG, and the AWG sitting at the OLT after 20 km of fiber.

The AWGs are modeled using *AWG M N* with passband shape determined by *DataSheet* model and passband type of *FlatMultiGauss* to represent Flat band shape (1-dB and 3-dB bandwidth set to 50 and 75 GHz) or *Gaussian* (1-dB and 3-dB bandwidth set to 25 and 50 GHz) alternatively. The AWG center frequency is set to 193.12 THz, and changed accordingly for the third AWG to simulate frequency detuning effects.

BER estimators are located at various points in the simulation, specifically after each AWG channel for upstream signal. The module Optical receiver with BER estimation (*Rx OOK BER*) is used for this purpose, which estimates Bit Error Rate and Q factor of the directly modulated ASE signal after each AWG filter. The optical receiver is a PIN photo-detector and the VPI default values for this module are used.

The results of this simulation are discussed in Chapter 4.
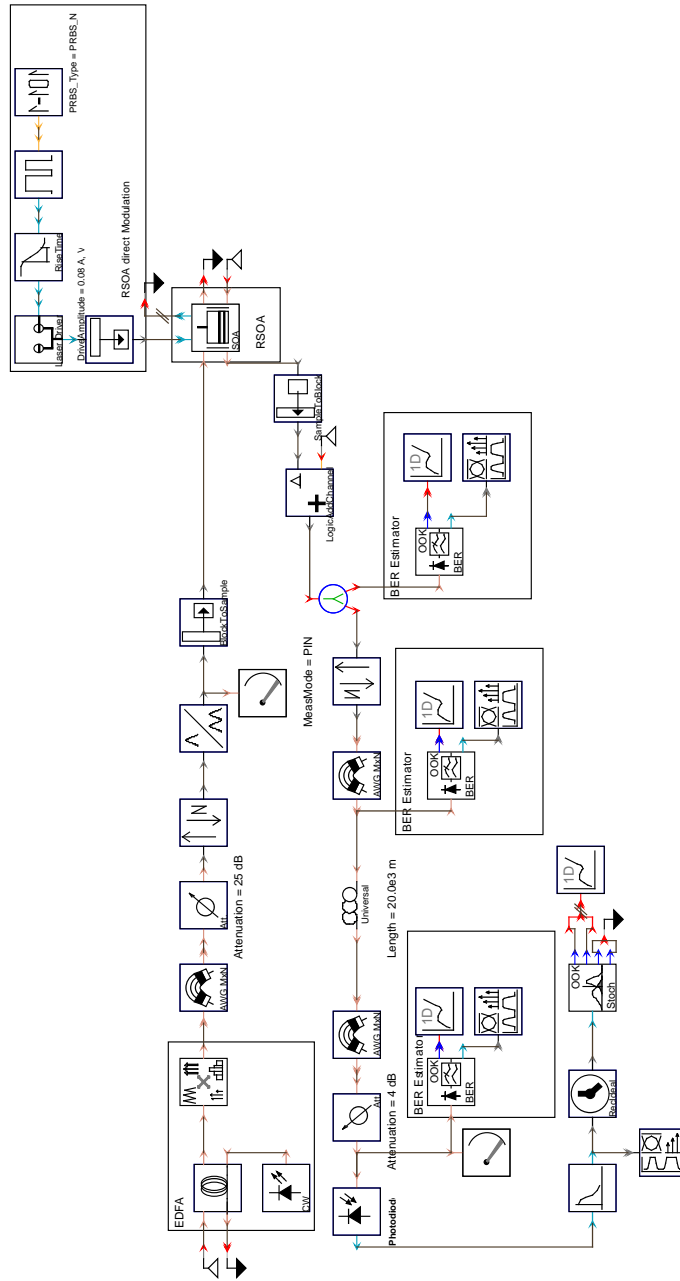
Figure C.1: WDM-PON model for simulation of AWG effects using VPI tool

Appendix D

VPI model: Injection-Locked FP laser

This Appendix describes the simulation model used for determining the injection-locking range of a FP laser diode in a WDM PON. For this simulation the FP laser is modeled using the Transmission Line Model of a semiconductor laser module (*LaserTLM*), with parameters tabulated in Table D.1. The input seed source to the FP laser is a CW laser with 1 mW power and controlled by a VOA (*Attenuator*) before being injected into the FP laser. CW laser emission frequency was modified from 193.1-195.1 THz to visualize injection-locking range.

The injection-locked output of the FP laser is filtered by an optical bandpass filter (*FilterOpt*) with 25 GHz of bandwidth. A direct receiver with a PIN photodiode (*RxOOK*) is used to receive the signal, and the injection-locked optical spectrum of ILFP laser can be viewed by the signal analyzer to determine the locking range.

The results of this discussion are presented in detail in Chapter 5.

Laser Parameter	Value
Active Region	MQW
Active Region Length	350e-6m
Active Region Width	2.5e-6m
QW thickness	40e-9m
SCH thickness	210e-9m
Group index	3.7
Loss	10 cm^{-1}
QW confinement	0.07
Device Length	800 μm
Operation Current	60 mA
Facet Reflectivity	0.32

Table D.1: Parameters used for modeling injection locked laser.
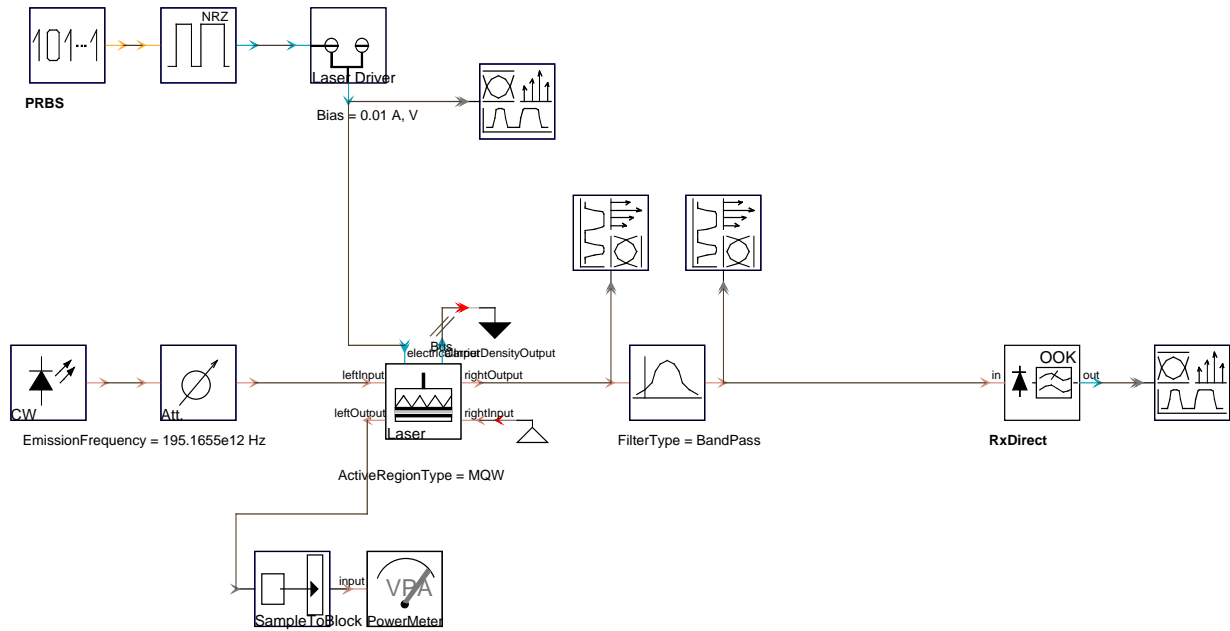
Figure D.1: Simulation model used for extraction of injection locking range of a FP laser diode

References

[1] Novera Optics. WDM-PON for the Access Network White Paper, 2008.

[2] CIP Technologies. WDM-PON Technologies White Paper, Dec 2011.

[3] NTT Electronics. `http://www.ntt-electronics.com/en/products/photonics/`.

[4] J. Horer and E. Patzak. Large-signal analysis of all-optical wavelength conversion using two-mode injection-locking in semiconductor lasers. *IEEE Journal of Quantum Electronics*, 33(4):596–608, Apr 1997.

[5] C.H. Lee, S.M. Lee, K.M. Choi, J.H. Moon, S.G. Mun, K.T. Jeong, J.H. Kim, and B. Kim. WDM-PON experiences in Korea [Invited]. *Journal of Optical Networking*, 6(5):451–464, May 2007.

[6] I.P. Kaminow, T. Li, and A.E. Willner. *Optical fiber telecommunications VB: systems and networks*. Academic Pr, 2008.

[7] E. Ip, A.P.T. Lau, D.J.F. Barros, and J.M. Kahn. Coherent detection in optical fiber systems. *Optics Express*, 16(2):753–791, Jan 2008.

[8] A. Sano, T. Kobayashi, S. Yamanaka, A. Matsuura, H. Kawakami, Y. Miyamoto, K. Ishihara, and H. Masuda. 102.3 Tb/s (224 x 548 Gb/s) C and extended L-band all-Raman transmission over 240 km using PDM-64QAM single carrier FDM with digital pilot tone. In *Optical Fiber Communication Conference and Exposition (OFC/NFOEC)*, pages 1 –3, March 2012.

[9] `http://www.ftthcouncil.org/`.

[10] N. Ghazisaidi, M. Maier, and C. Assi. Fiber-wireless (FiWi) access networks: A survey. *IEEE Communications Magazine*, 47(2):160 –167, Feb 2009.

[11] J.R. Stern, C.E. Hoppitt, D.B. Payne, M.H. Reeve, and K. Oakley. TPON-a passive optical network for telephony. In *Fourteenth European Conference on Optical Communication (ECOC)*, volume 1, pages 203–206, Sep 1988.

[12] F.J. Effenberger, H. Ichibangase, and H. Yamashita. Advances in broadband passive optical networking technologies. *IEEE Communications Magazine*, 39(12):118–124, Dec 2001.

[13] G. Kramer and G. Pesavento. Ethernet passive optical network (EPON): building a next-generation optical access network. *IEEE Communications Magazine*, 40(2):66–73, Feb 2002.

[14] J.D. Angelopoulos, H.C. Leligou, T. Argyriou, S. Zontos, E. Ringoot, and T. Van Caenegem. Efficient transport of packets with QoS in an FSAN-aligned GPON. *IEEE Communications Magazine*, 42(2):92–98, Feb 2004.

[15] J. Kani and N. Yoshimoto. Next generation PONs: an operator's view. *35st European Conference on Optical Communication (ECOC)*, 2009.

[16] N.J. Frigo, P.P. Iannone, P.D. Magill, T.E. Darcie, M.M. Downs, B.N. Desai, U. Koren, T.L. Koch, C. Dragone, H.M. Presby, and G.E. Bodeep. A wavelength-division multiplexed passive optical network with cost-shared components. *IEEE Photonics Technology Letters*, 6(11):1365–1367, Nov 1994.

[17] ITU-T Recommendation: G.694.2. Spectral Grids for WDM Applications: CWDM wavelength grid, March 2002.

[18] H. Toda, T. Yamashita, K. Kitayama, and T. Kuri. DWDM demultiplexing with 25-Ghz channel spacing for 60-Ghz band radio-On-fiber systems. In *28th European Conference on Optical Communication (ECOC)*, volume 3, pages 1 –2, Sep 2002.

[19] L. Gasca. From O to L: The future of optical-wavelength bands. *Broadband Properties*, pages 83–85, June 2008.

[20] H.A. Macleod. *Thin-film optical filters*. Taylor & Francis, 2001.

[21] M.K. Smit and C. Van Dam. PHASAR-based WDM-devices: Principles, design and applications. *IEEE Journal of Selected Topics in Quantum Electronics*, 2(2):236 –250, June 1996.

[22] A. Banerjee, Y. Park, F. Clarke, H. Song, S. Yang, G. Kramer, K. Kim, and B. Mukherjee. Wavelength-division-multiplexed passive optical network (WDM-PON) technologies for broadband access: a review [Invited]. *Journal of optical networking*, 4(11):737–758, Oct 2005.

[23] M. Attygalle, N. Nadarajah, and A. Nirmalathas. Wavelength reused upstream transmission scheme for WDM passive optical networks. *Electronics Letters*, 41(18):1025 – 1027, Sep 2005.

[24] J. Hasegawa and K. Nara. Ultra low loss athermal AWG module with a large number of channels. *Furukawa Rev*, 26, 2004.

[25] Gemfire Inc. `http://www.gemfire.com/index.html`.

[26] NeoPhotonics Inc. `http://www.neophotonics.com/`.

[27] K. Kudo, K. Yashiki, T. Sasaki, Y. Yokoyama, K. Hamamoto, T. Morimoto, and M. Yamaguchi. 1.55 μ m wavelength-selectable microarray DFB-LD's with monolithically integrated MMI combiner, SOA, and EA-modulator. *IEEE Photonics Technology Letters*, 12(3):242–244, March 2000.

[28] D. Anthon, J.D. Berger, J. Drake, S. Dutta, A. Fennema, J.D. Grade, S. Hrinya, F. Ilkov, H. Jerman, D. King, et al. External cavity diode lasers tuned with silicon MEMS. In *Optical Fiber Communication Conference (OFC)*, 2002.

[29] W.B. Chapman, A. Farinas, C. Hand, H. Li, A. Daiber, N. Maluf, et al. Tunable external cavity laser, March 2004.

[30] B. Mason, G.A. Fish, S.P. DenBaars, and L.A. Coldren. Widely tunable sampled grating DBR laser with integrated electroabsorption modulator. *IEEE Photonics Technology Letters*, 11(6):638 –640, June 1999.

[31] S. Kanazawa, T. Fujisawa, A. Ohki, H. Ishii, N. Nunoya, Y. Kawaguchi, N. Fujiwara, K. Takahata, R. Iga, F. Kano, and H. Oohashi. A compact EADFB laser array module for a future 100-Gb/s Ethernet transceiver. *IEEE Journal of Selected Topics in Quantum Electronics*, 17(5):1191 –1197, Sep 2011.

[32] Soo-Jin Park, Chang-Hee Lee, Ki-Tae Jeong, Hyung-Jin Park, Jeong-Gyun Ahn, and Kil-Ho Song. Fiber-to-the-home services based on wavelength-division-multiplexing passive optical network. *Journal of Lightwave Technology*, 22(11):2582–2591, Nov 2004.

[33] NJ Frigo, PP Iannone, and KC Reichmann. Spectral slicing in WDM passive optical networks for local access. In *24th European Conference on Optical Communication*, volume 1, 1998.

[34] S.L. Woodward, P.P. Iannone, K.C. Reichmann, and N.J. Frigo. A spectrally sliced PON employing Fabry-Perot lasers. *IEEE Photonics Technology Letters*, 10(9):1337–1339, Sep 1998.

[35] S.J. Park, G.Y. Kim, and T.S. Park. WDM-PON system based on the laser light injected reflective semiconductor optical amplifier. *Optical Fiber Technology*, 12(2):162–169, Apr 2006.

[36] F. Payoux, P. Chanclou, M. Moignard, and R. Brenot. Gigabit optical access using WDM-PON based on spectrum slicing and reflective SOA. In *31st European Conference on Optical Communication (ECOC)*, volume 3, pages 455 – 456 vol.3, Sep 2005.

[37] http://www.kamelian.com/.

[38] M.D. Feuer, J.M. Wiesenfeld, J.S. Perino, C.A. Burrus, G. Raybon, S.C. Shunk, and N.K. Dutta. Single-port laser-amplifier modulators for local access. *IEEE Photonics Technology Letters*, 8(9):1175 –1177, Sep 1996.

[39] P. Healey, P. Townsend, C. Ford, L. Johnston, P. Townley, I. Lealman, L. Rivers, S. Perrin, and R. Moore. Spectral slicing WDM-PON using wavelength-seeded reflective SOAs. *Electronics Letters*, 37:1181, Sep 2001.

[40] J.J. Koponen and M.J. Soderlund. A duplex WDM passive optical network with 1:16 power split using reflective SOA remodulator at ONU. In *Optical Fiber Communication Conference (OFC)*, volume 1, page 298, Feb 2004.

[41] W. Lee, M.Y. Park, S.H. Cho, J. Lee, C. Kim, G. Jeong, and B.W. Kim. Bidirectional WDM-PON based on Gain-Saturated Reflective Semiconductor Optical Amplifiers. *IEEE Photonics Technology Letters*, 17(11):2460–2462, Nov 2005.

[42] J. Prat, C. Arellano, V. Polo, and C. Bock. Optical network unit based on a bidirectional reflective semiconductor optical amplifier for fiber-to-the-home networks. *IEEE Photonics Technology Letters*, 17(1):250–252, Jan 2005.

[43] MO Van Deventer. Polarization properties of Rayleigh backscattering in single-mode fibers. *Journal of Lightwave Technology*, 11(12):1895–1899, Dec 1993.

[44] E. Wong, K.L. Lee, and T.B. Anderson. Directly modulated self-seeding reflective semiconductor optical amplifiers as colorless transmitters in wavelength division multiplexed passive optical networks. *Journal of Lightwave Technology*, 25(1):67–74, Jan 2007.

[45] N. Nadarajah, K.L. Lee, and A. Nirmalathas. Upstream access and local area networking in passive optical networks using self-seeded reflective semiconductor optical amplifier. *IEEE Photonics Technology Letters*, 19(19):1559–1561, Oct 2007.

[46] KY Cho, Y. Takushima, and YC Chung. 10-Gb/s Operation of RSOA for WDM PON. *IEEE Photonics Technology Letters*, 20(18):1533–1535, Sep 2008.

[47] S.C. Lin, S.L. Lee, and C.K. Liu. Simple approach for bidirectional performance enhancement on WDM-PONs with direct modulation lasers and RSOAs. *Optics Express*, 16(6):3636–3643, March 2008.

[48] KY Cho, Y. Takushima, and YC Chung. Enhanced operating range of WDM PON implemented by using uncooled RSOAs. *IEEE Photonics Technology Letters*, 20(18):1536–1538, Sep 2008.

[49] H.D. Kim, S.G. Kang, and C.H. Le. A low-cost WDM source with an ASE injected Fabry-Perot semiconductor laser. *IEEE Photonics Technology Letters*, 12(8):1067–1069, Aug 2000.

[50] S.M. Lee, K.M. Choi, S.G. Mun, J.H. Moon, and C.H. Lee. Dense WDM-PON based on wavelength locked Fabry-Perot laser diodes. *IEEE Photonics Technology Letters*, 17(7):1579–1581, July 2005.

[51] Z. Xu, Y.J. Wen, W.D. Zhong, C.J. Chae, X.F. Cheng, Y. Wang, C. Lu, and J. Shankar. High-speed WDM-PON using CW injection-locked Fabry-Pérot laser diodes. *Optics Express*, 15(6):2953–2962, March 2007.

[52] A. Turukhin, L. Lunardi, E. Gonzales, and K. Vreeburg. SOA characteristics for L-BAND system applications. In *28th European Conference on Optical Communication (ECOC)*, volume 3, pages 1 –2, Sep 2002.

[53] C. Arellano Pinilla. *Investigation of reflective optical network units for bidirectional passive optical access networks*. PhD thesis, Universitat Politècnica de Catalunya, 2007.

[54] S.W. Corzine L.A. Coldren. *Diode Lasers and Photonic Integrated Circuits*. Wiley, New York, 1995.

[55] G.P. Agrawal. *Fiber-Optic Communication Systems*. Wiley-Interscience, 2002.

[56] Michael J. Connelly. Wideband steady-state numerical model of a tensile-strained bulk semiconductor optical amplifier. *Optical and Quantum Electronics*, 38(12-14):1061–1068, Nov 2006.

[57] M.J. Connelly. *Semiconductor Optical Amplifiers*. Springer, 2002.

[58] L. Gillner. Comparative study of some travelling-wave semiconductor laser amplifier models. *IEE Proceedings J Optoelectronics*, 139(5):339 –347, Oct 1992.

[59] P. Brosson. Analytical model of a semiconductor optical amplifier. *Journal of Light-wave Technology*, 12(1):49 –54, Jan 1994.

[60] S.S. Saini, S.H. Cho, and M. Dagenais. Thermal considerations in high power semiconductor lasers and semiconductor optical amplifiers. In *Proceedings of the SPIE:Photonics Packaging, Integration, and Intercounnects VII*, volume 6478, page 05, 2007.

[61] C. Michie, T. Kelly, and I. Andonovic. Reflective Semiconductor Optical Amplifiers in passive optical networks. In *14th OptoElectronics and Communications Conference (OECC)*, pages 1 –2, July 2009.

[62] S. Park, R. Leavitt, R. Enck, V. Luciani, Y. Hu, PJS Heim, D. Bowler, and M. Dagenais. Semiconductor optical amplifier for CWDM operating over 1540-1620 nm. *IEEE Photonics Technology Letters*, 17(5):980–982, May 2005.

[63] I. Vurgaftman, J. R. Meyer, and L. R. Ram-Mohan. Band parameters for III–V compound semiconductors and their alloys. *Journal of Applied Physics*, 89(11):5815–5875, June 2001.

[64] S.S Saini, J. Bowser, R. Enck, V. Luciani, PJS Heim, and Dagenais. A semiconductor optical amplifier with high saturation power low noise figure and low polarization dependent gain over the C-band. In *The 17th Annual Meeting of the IEEE Lasers and Electro-Optics Society (LEOS)*, volume 1, 2004.

[65] S. Taebi and S.S. Saini. L-Band Polarization-Independent Reflective SOA for WDM-PON Applications. *IEEE Photonics Technology Letters*, 21(5):334–336, March 2009.

[66] AE Kelly, C. Michie, W. Zhong, S. Karagianopoulos, WI Madden, C. Tombling, and I. Andonovic. High performance polarisation independent reflective semiconductor optical amplifiers in the S, C, and L bands. *IEEE Journal on Selected Areas in Communications*, 28(6):943–948, Aug 2010.

[67] Shun Lien Chuang. *Physics of Optoelectronic Devices*. Wiley, New York, 1995.

[68] C. Michie, A. E. Kelly, J. McGeough, I. Armstrong, Ivan Andonovic, and C. Tombling. Polarization-insensitive SOAs using strained bulk active regions. *Journal of Lightwave Technology*, 24(11):3920–3927, Nov 2006.

[69] FIMMWAVE mode solver: . `http://www.photond.com/products/fimmwave.htm`.

[70] D. Marcuse. Reflection loss of laser mode from tilted end mirror. *Journal of Lightwave Technology*, 7(2):336–339, Feb 1989.

[71] F. Ladouceur and E. Labeye. A new general approach to optical waveguide path design. *Journal of Lightwave Technology*, 13(3):481–492, March 1995.

[72] P.J.S. Heim, Z.F. Fan, S.-H. Cho, K. Nam, M. Dagenais, F.G. Johnson, and R. Leavitt. Single-angled-facet laser diode for widely tunable external cavity semiconductor lasers with high spectral purity. *Electronics Letters*, 33(16):1387–1389, July 1997.

[73] D. Derickson, C. Hentschel, and Hewlett-Packard. *Fiber Optic Test and Measurement*. Prentice Hall PTR New Jersey, 1998.

[74] P. Chanclou, F. Payoux, T. Soret, N. Genay, R. Brenot, F. Blache, M. Goix, J. Landreau, O. Legouezigou, and F. Mallecot. Demonstration of RSOA-based remote modulation at 2.5 and 5 Gbit/s for WDM PON. In *Optical Fiber Communication/National Fiber Optic Engineers Conference (OFC)*, pages 1–3, 2007.

[75] IT Monroy, F. Ohman, K. Yvind, LJ Christiansen, J. Mørk, C. Peucheret, P. Jeppesen, and DTU Fotonik. Monolithically integrated reflective SOA-EA carrier remodulator for broadband access nodes. *Optics Express*, 14(18):8060–8064, Sep 2006.

[76] A. Garreau, J. Decobert, C. Kazmierski, M.-C. Cuisin, J.-G. Provost, H. Sillard, F. Blache, D. Carpentier, J. Landreau, and P. Chanclou. 10Gbit/s Amplified reflective electroabsorption modulator for colourless access networks. In *International Conference on Indium Phosphide and Related Materials (IPRM)*, pages 168–170, May 2006.

[77] X. Li, MJ Adams, D. Alexandropoulos, and IF Lealman. Gain recovery in semiconductor optical amplifiers. *Optics Communications*, 281(13):3466–3470, July 2008.

[78] J J Dong, X L Zhang, and D X Huang. Experimental and theoretical study on gain dynamics of SOA. *Acta Physica Sinica*, 54(6):763–767, Feb 2005.

[79] G.P. Agrawal and N.A. Olsson. Self-phase modulation and spectral broadening of optical pulses in semiconductor laser amplifiers. *IEEE Journal of Quantum Electronics*, 25(11):2297–2306, Nov 1989.

[80] D.M. Baney, P. Gallion, and R.S. Tucker. Theory and measurement techniques for the noise figure of optical amplifiers. *Optical fiber technology*, 6(2):122–154, Apr 2000.

[81] Kamelian Application Note 002. Semiconductor optical amplifiers (SOAs) as preamplifiers.

[82] http://www.ciphotonics.com/.

[83] N.A. Olsson. Lightwave systems with optical amplifiers. *Journal of Lightwave Technology*, 7(7):1071 –1082, July 1989.

[84] R. Ramaswami and K.N. Sivarajan. *Optical Networks: A Practical Perspective.* Morgan Kaufmann; 2nd Revised edition, 2001.

[85] L. Chrostowski, C.H. Chang, R. Stone, and C.J. Chang-Hasnain. Demonstration of long-wavelength directly modulated VCSEL transmission using SOAs. *IEEE Photonics Technology Letters*, 14(9):1369–1371, Sep 2002.

[86] H. Nakamura, H. Suzuki, and K. Iwatsuki. SNR degradation owing to spectrum sliced effect in carrier-distributed WDM-PON. *Electronics Letters*, 42(3):179–181, Feb 2006.

[87] VPIphotonics. http://www.vpiphotonics.com/.

[88] Y. Inoue, A. Kaneko, F. Hanaw, H. Takahashi, K. Hattori, and S. Sumida. Athermal silica-based arrayed-waveguide grating (AWG) multiplexer. In *11th International Conference on Integrated Optics and Optical Fibre Communications*, volume 5, 1997.

[89] K. Hirabayashi, N. Koshobu, J. Kobayashi, M. Itoh, and S Kamei. Reduction of second-order temperature dependence of Silica-based athermal AWG by using two resin-filled grooves. *IEEE Photonics Technology Letters*, 23(11):676–678, June 2011.

[90] I. Roudas, N. Antoniades, T. Otani, T. E. Stern, R. E. Wagner, and D. Q. Chowdhury. Accurate modeling of optical multiplexer/demultiplexer concatenation in transparent multi-wavelength optical networks. *Journal of Lightwave Technology*, 20(6):921–936, June 2002.

[91] Safa O. Kasap. *Optoelectronics and Photonics: Principles and Practices.* Prentice Hall, 2001.

[92] Sang-Mook Lee, Ki-Man Choi, Sil-Gu Mun, Jung-Hyung Moon, and Chang-Hee Lee. Dense WDM-PON based on wavelength-locked Fabry-Perot laser diodes. *IEEE Photonics Technology Letters*, 17(7):1579–1581, July 2005.

[93] R. Lang. Injection locking properties of a semiconductor laser. *IEEE Journal of Quantum Electronics*, 18(6):976–983, June 1982.

[94] Zhaowen Xu, Yang Jing Wen, Wen-De Zhong, Chang-Joon Chae, Xiao-Fei Cheng, Yixin Wang, Chao Lu, and Jaya Shankar. High-speed WDM-PON using CW injection-locked Fabry-Pérot laser diodes. *Opt. Express*, 15(6):2953–2962, March 2007.

[95] Hyun Deok Kim, Seung-Goo Kang, and Chang-Hee Le. A low-cost WDM source with an ASE injected Fabry-Perot semiconductor laser. *IEEE Photonics Technology Letters*, 12(8):1067–1069, Aug 2000.

[96] Kun-Youl Park, Sil-Gu Mun, Ki-Man Choi, and Chang-Hee Lee. A theoretical model of a wavelength-locked Fabry-Perot laser diode to the externally injected narrow-band ASE. *IEEE Photonics Technology Letters*, 17(9):1797–1799, Sep 2005.

[97] E.H. Lee, Y.C. Bang, J.K. Kang, Y.C. Keh, D.J. Shin, J.S. Lee, S.S. Park, I. Kim, J.K. Lee, Y.K. Oh, and D.H. Jang. Uncooled C-band wide-band gain lasers with 32-channel coverage and -20-dBm ASE injection for WDM-PON. *IEEE Photonics Technology Letters*, 18(5):667–669, March 2006.

[98] Sareh Taebi and Simarjeet Singh Saini. Injection locked Fabry-Perot lasers with integrated phase modulators. In *Indium Phosphide and Related Materials, 2009. IPRM '09. IEEE International Conference on*, pages 282–284, May 2009.

[99] L.A. Coldren, GA Fish, Y. Akulova, JS Barton, L. Johansson, and CW Coldren. Tunable semiconductor lasers: A tutorial. *Journal of Lightwave Technology*, 22(1):193, Jan 2004.

[100] R. G. Hunsperger. *Integrated Optics: Theory and Technology.* Springer, 2002.

[101] EJ Thrush, JP Stagg, MA Gibbon, RE Mallard, B. Hamilton, JM Jowett, and EM Allen. Selective and non-planar epitaxy of InP/GaInAs (P) by MOCVD. *Materials science & engineering. B*, 21(2-3):130–146, Nov 1993.

[102] C.E. Zah, R. Bhat, S.G. Menocal, N. Andreadakis, F. Favire, C. Caneau, M.A. Koza, and T.P. Lee. 1.5 μ m GaInAsP angled-facet flared-waveguide traveling-wave laser amplifiers. *IEEE Photonics Technology Letters*, 2(1):46–47, Jan 1990.

[103] T.R. Zaman and R.J. Ram. Modulation of injection locked lasers for WDM-PON applications. In *Optical Fiber communication/National Fiber Optic Engineers Conference (OFC/NFOEC)*, pages 1–3, Feb 2008.

[104] S.K. Mondal, B. Roycroft, P. Lambkin, F. Peters, B. Corbett, P. Townsend, and A. Ellis. A multiwavelength low-power wavelength-Locked slotted Fabry Perot laser source for WDM applications. *IEEE Photonics Technology Letters*, 19(10):744 –746, May 2007.

[105] J.H. Moon, K.M. Choi, S.G. Mun, and C.H. Lee. An automatic wavelength control method of a tunable laser for a WDM-PON. *IEEE Photonics Technology Letters*, 21(5):325–327, March 2009.

[106] Franck Pauyoux. *Etude Des Reseaux D'access Optiques Exploitant Le Multiplexage En Longueurs D'onde.* PhD thesis, L'ecole Nationale Superieure des Telecommunications de Bretagne, 2006.